Thesis submitted to

Jawaharlal Nehru University

for the degree of

Doctorate of Philosophy

Shear-induced yielding, memory formation and jamming in dense particulate suspensions

---

Author
Sebanti Chattopadhyay

Supervisor
Dr. Sayantan Majumdar

Soft and Adaptive Materials Lab
Department of Soft Matter Physics
Raman Research Institute
Bengaluru, India

2023

Dedication

To my parents...

Declaration

I hereby declare that the work reported in this doctoral thesis titled **"Shear-induced yielding, memory formation and jamming in dense particulate suspensions"** is entirely original and is the result of the research work carried out by me in the **Soft Matter Physics Group, Raman Research Institute, Bengaluru, India** under the supervision of **Dr. Sayantan Majumdar**. No part of this work was previously presented for the award of any degree, diploma, fellowship, or similar title to any University or Institution. I have also run the thesis through Turnitin plagiarism software.

Dr. Sayantan Majumdar
Thesis supervisor

Sebanti Chattopadhyay

Certificate

This is to certify that the dissertation/thesis titled "**Shear-induced yielding, memory formation and jamming in dense particulate suspensions**" submitted by Ms. **Sebanti Chattopadhyay**, in partial fulfillment of the requirements for the award of the degree of **Doctorate of Philosophy** at the Jawaharlal Nehru University, New Delhi, has not been previously submitted in part or in full for any other degree of this university or any other university/institution.

Prof. Tarun Souradeep	**Dr. Sayantan Majumdar**
Director	Thesis supervisor

Acknowledgements

While pursuing a doctorate is undeniably fulfilling, it frequently becomes overwhelming and stress-inducing. I would like to seize this opportunity to convey my deep appreciation to the individuals who were instrumental throughout this journey. Your unwavering support and encouragement have had a profound impact on me, and I will carry your kindness with me always.

My doctorate stands as a profound testament to the exceptional mentorship provided by my supervisor Dr. Sayantan Majumdar. I am deeply appreciative that he consistently maintained his calm and patient demeanor. His unwavering support and encouragement has motivated me to strive for excellence. Under his guidance, I have honed my critical thinking skills and developed the ability to pose pertinent questions, addressing a personal shortcoming that I had long recognized. I am perpetually humbled by his profound insights into the subject matter and his ingenious approach to execution. I extend my heartfelt gratitude for affording me this extraordinary doctoral experience. Being your first student has been a privilege and I will be proudly wearing this badge for many years.

This thesis and the six years of dedication it represents would not have been achievable without the unwavering support of my parents. Their enduring patience and understanding throughout my doctoral journey is something I am eternally thankful for. I feel blessed to have maternal grandparents who eagerly anticipate the completion of my doctorate. Words fail me when I try to convey my appreciation to my extended family (Masimoni, Meso and Antara), who have been a loving and motivating presence in my life. I hold deep affection for each and every one of you.

I extend my heartfelt gratitude to Prof. Supurna Sinha, who served as my first research mentor during a brief internship in 2014. Reconnecting with her upon joining RRI for my Ph.D. in 2017 brought me great joy. My passion and deep appreciation for the realm of soft matter physics blossomed while working with Prof. Shankar Ghosh at TIFR, Mumbai

as a summer intern back in 2015. His guidance and introduction to this captivating field of science are invaluable, and I will forever be indebted to him. Additionally, I wish to express my sincere thanks to Prof. Kanhaiya Lal Yadav, who served as my M.Sc. thesis advisor. My experience working in his lab played a pivotal role in laying the groundwork for aspects of my doctoral research.

I am deeply indebted to Prof. Gautam Soni, with whom I had the privilege of being a student briefly during my first year. His invaluable lesson, "Nothing should be a black box when it comes to your experimental setup," has left a lasting impact on my approach to research. I am committed to upholding this principle throughout my academic journey.

I extend my sincere gratitude to Prof. Ranjini Bandyopadhyay and Prof. Pramod Pullarkat for their active involvement as members of my research advisory committee. Their engagement has been truly enriching, as I have consistently received invaluable suggestions and guidance regarding my research during our interactions. Additionally, both of them generously extended support from their labs and lab members when our own lab was still in the process of being set up, and we faced challenges with access to instruments, raw materials, and expertise. Additionally, I want to express my thanks to Prof. Sanjib, Prof. Arun, and Prof. Raghunathan for their contribution to my thesis as part of the coursework at RRI.

I would like to extend my gratitude to Radhakrishna sir, who served as the department secretary for half of my doctorate. His adept handling and guidance in navigating lab purchases and related paperwork were invaluable. I would also like to express my appreciation to Raja, Murali, and Mahadeva for their continuous efforts in ensuring the well-managed and maintained state of our labs and workspaces. A big shoutout to Yatheendran for his assistance with SEM and confocal imaging for my research systems. Additionally, I appreciate Serene for her guidance in SEM sample preparation.

Chaithanya, I am deeply thankful for your exceptional secretarial skills, which rank as my second favorite aspect of your contribution. First and foremost, your unwavering friendship and support since your arrival at RRI have meant the world to me. Navigating the final stages, particularly the tedious paperwork, would not have been as smooth without your constant assistance. Your contributions have been immensely valuable, and I extend my heartfelt gratitude for everything you've done.

I would also like to extend my appreciation to the RRI library for their most valuable and timely assistance. My gratitude also goes to the RRI IT department, canteen staff, and security personnel for their continuous efforts. I am deeply indebted to the RRI workshop team for their exceptional craftsmanship in creating essential setups and parts

for my research. To all those involved in the RRI Administration, I offer my sincerest regards for your unwavering support and assistance throughout these years, especially during the challenging periods of the COVID lockdowns. Your support was instrumental in helping us navigate those uncertain times. I would like to express my thanks to the RRI Sports committee for allowing me to be a part of it. Being a member of the committee for three years brought me genuine joy and pride.

I have been fortunate to work alongside some exceptional colleagues in the lab. Beginning with Sachidananda, my first lab junior. I cannot thank you enough for constantly challenging my work with your insightful questions. Your unwavering dedication to improving my research has my deepest appreciation. Abhishek, beyond being colleagues, it's been a pleasure being your friend. I owe you a heartfelt thanks for seamlessly handling many responsibilities with such diligence. Your presence has been a wonderful asset to our lab and to my personal life. Here's to you, raising a glass in appreciation. Akhil, you were instrumental in giving me the confidence to initiate the vibration experiments, and for that, I am truly thankful. My sincere thanks to Soumen and Maitri for your valuable input and support. My work has benefitted greatly from the contribution of my collaborators Sharadhi and Subhranshu, who also co-authored some of my papers. A heartfelt cheer goes out to all current and former lab members who, in various ways, contributed to my work and provided me with opportunities for growth.

Finally, I want to express my gratitude to the numerous people I've had the privilege of meeting during my time at RRI. Thank you all for sharing in the ups and downs of life with me. My personal journey has been marked by its share of challenges over these years, but I have decided to leave those behind and embrace what lies ahead. As I embark on new paths ahead, let Robert Frost's words echo in my mind:

The woods are lovely, dark and deep,
But I have promises to keep,
And miles to go before I sleep,
And miles to go before I sleep.

Preface

Soft matter physics is an emerging area of science that involves the study of materials which are intermediate between a Newtonian liquid and a crystalline solid. These materials can be easily deformed by an external force and show viscoelasticity. Examples of such materials include: emulsions, gels, surfactants, liquid crystals, polymers, suspensions, etc. In day to day life, such materials are all around us. Soft materials are characterized by the mesoscopic sizes of the constituents and weak interactions between the constituents, hence entropic effects are often important. This results in many interesting features like large response functions, slow relaxation dynamics and self-organization. Many of these properties have made soft materials a testing ground for non-equilibrium statistical physics. These materials also show striking non-linear flow behaviours that include shear-thinning, shear-thickening and strain-localization/shear-banding. Aside from their ubiquity, soft materials find wide range of industrial applications in food and polymer processing, oil recovery, cosmetics and pharmaceuticals, etc.

Dense suspensions, formed by dispersing solid particles in Newtonian fluids in high proportion, are one such important class of soft materials that has drawn significant research attention in recent years. Apart from the general applications mentioned above, these systems also have application-potential in designing smart and adaptive materials. Importantly, dense suspensions are model systems for complex jammed materials, which can be used to study material failures in connection to catastrophic natural phenomena like landslides and earthquakes.

In this thesis, I study the flow and deformation properties of athermal dense suspensions of granular particles by using rheology combined with in-situ optical imaging. I explore an array of important non-linear flow properties including yielding, energy dissipation, shear banding, memory formation, shear-thickening and shear-induced jamming. By tuning the interparticle interactions, I try to understand the underlying mechanisms

behind such striking response and ways to control them over a large range of spatio-temporal scales.

The thesis is divided into the following chapters:

Chapter-1: This chapter gives a general introduction to the field of soft matter physics. I explain, in detail, the various features of soft matter systems that make them interesting to study and important as model systems for many scientific areas. I also give some overview of the important topics related to the chapters of this thesis.

Chapter-2: In this chapter, I discuss the experimental techniques and the various sample preparation techniques used in the thesis.

Chapter-3: In this chapter, I discuss the yielding and energy dissipation in adhesive dense granular suspensions formed by dispersing Cornstarch (CS) particles in Paraffin oil (PO). CS particles are hydrophilic, so they experience a solvent-mediated adhesion when dispersed in the non-polar oil. As a result, the particles form fractal aggregates that give rise to a yield stress in the system beyond a critical volume fraction called the adhesive loose packing fraction. I use Large Amplitude Oscillatory Shear (LAOS) protocol, with an amplitude spanning a range of over 3 orders of magnitude, to study the yielding behaviour of this system over a wide range of volume fraction. I find that the adhesive interaction imparts a significantly higher energy dissipation to the system as compared to well-dispersed suspensions (where the inter-particle interactions are primarily steric repulsive and frictional) of CS in glycerol/glycerol-water mixtures, over the whole range of applied strain amplitudes. I introduce a parameter called the normalized energy dissipation (E_N) to characterize the yielding behaviour of the system. I find that E_N shows a non-monotonic variation with both applied strain amplitude and volume fraction of the suspensions. This system also shows strain stiffening behaviour for intermediate applied strain values, which causes the non-monotonicity in E_N as a function of applied strain amplitude. Further, using in-situ optical boundary imaging and particle tracking, I map out the difference in the flow of the system below and above yielding. I also characterize the plasticity in the system using stroboscopic analysis. Interestingly, I find that the system flows in a shear banded manner both below as well as above yielding. However, the velocity profiles are spatio-temporally erratic below yielding while above yielding, the profiles are more well-behaved and self-similar. Additionally, the plastic particle rearrangements happen throughout the bulk below yielding but above yielding, they are mostly restricted to the shearing boundaries (within the shear bands). Next, to understand the non-monotonic variation of E_N with volume fraction, I use particle settling experiments. This study is the first instance of using such experiments for adhesive

granular systems to determine the critical jamming volume fractions. Finally, I use a non-ionic surfactant (Span-60) to vary the inter-particle adhesion and I find that the non-monotonicity of E_N goes away when the adhesion is significantly nullified. Moreover, the flow behaviour of the system changes from shear banded to a quasi-linear flow and the system no longer strain stiffens. I summarize the results into a detailed phase diagram describing the behaviour of the system over a wide parameter space.

Chapter-4: In this chapter, I explore memory formation in adhesive granular gels formed by Cornstarch particles dispersed in Paraffin oil, as also mentioned in the previous chapter. It is known in literature that repeated/cyclic shearing can drive amorphous solids to a steady state, encoding a memory of the applied strain amplitude. However, recent experiments found that the effect of such memory formation on the mechanical properties of the bulk material is rather weak. I find that under cyclic shear, our system evolves toward a steady state showing training-induced strain stiffening and plasticity. A readout reveals that the system encodes a strong memory of the training amplitude γ_T as indicated by a large change in the differential shear modulus. I observe that memory can be encoded for a wide range of γ_T values both above and below the yielding, albeit the strength of the memory decreases with increasing γ_T. In situ boundary imaging shows strain localization close to the shearing boundaries, while the bulk of the sample moves like a solid plug. In the steady state, the average particle velocity $< v >$ inside the solid-like region slows down with respect to the moving plate as γ approaches γ_T; however, as the readout strain crosses γ_T, $< v >$ suddenly increases. I demonstrate that inter-particle adhesive interaction is crucial for such a strong memory effect. Interestingly, our system can also remember more than one input only if the training strain with smaller amplitude is applied last.

Chapter-5: This chapter is a continuation of the previous one and primarily deals with the multiple memory formation in adhesive granular systems. The main focus of this chapter is how the encoded memory of a larger strain amplitude gets affected due to repeated application of a lower strain amplitude. Here, after training the system up to a certain strain amplitude, I apply N cycles of smaller strain amplitude before taking a readout. For disordered solids (particularly glasses), simulation studies have predicted that applying a smaller amplitude to a trained system can weaken the encoded memory of the larger amplitude but both memories survive indefinitely. However, systematic experimental studies probing such effects remains missing. I show experimentally that for disordered solids formed by adhesive granular suspensions, applying a smaller amplitude (γ) to a system trained at a larger amplitude (γ_T) can progressively decay the encoded

memory of γ_T to the point of destruction. Interestingly, in our system, this happens as a result of a systematic shift of the encoded amplitude γ_T towards γ with increasing N. Such shifting of encoded memory has not been reported previously. Moreover, I find that this shift is more pronounced if the system is trained at higher shearing rates. By analysing the energy dissipation in the system at various shear rates, I propose a possible mechanism for this interesting phenomenon.

Chapter-6: This chapter deals with dense suspensions of well dispersed frictional particles that show shear-thickening and shear induced jamming. It is well-known that under an increasing applied shear stress, the viscosity of dense well-dispersed suspensions of frictional particles increases drastically beyond a stress onset, a phenomenon known as discontinuous shear-thickening. Recent studies point out that some suspensions can transform into a stress-induced solid-like shear jammed (SJ) state at high particle volume fraction. SJ state develops a finite yield stress and hence is distinct from a shear-thickened state. Here, I study the steady-state shear-thickening behaviour of dense suspensions formed by dispersing colloidal Polystyrene particles (PS) in polyethylene glycol (PEG). I find that for small stress values, the viscosity of the suspensions as a function of volume fraction can be well described by Krieger–Dougherty (KD) relation. However, beyond the onset stress, KD relation systematically overestimates the measured viscosity, particularly for higher volume fractions. This systematic deviation can be rationalized by the weakening of the sample due to flow-induced failures of the solid-like SJ state. Using Wyart–Cates model, I propose a method to predict the SJ onset from the steady state rheology measurements.

Chapter-7: In this chapter, I explore the effects of applied orthogonal vibration on the rheology of dense particulate suspensions with different inter-particle interactions. Such superimposed vibrations have been used to reduce frictional yield stress as reported in the earlier studies. However, in the case of adhesion-induced yield stress, the effects of such vibration have not been explored. I find that the adhesive yield stress can also be significantly tuned using such orthogonal perturbations. Additionally, I also inspect the effects of such vibrations on shear-thickening dense suspensions.

Chapter-8: This chapter summarizes the main results of the thesis and highlights the open questions that remain to be explored in future.

Dr. Sayantan Majumdar
Thesis supervisor

Sebanti Chattopadhyay

List of Publications

1. **S. Chattopadhyay** and S. Majumdar, "Orthogonal vibration induced tuning of yield stress in adhesive jammed systems", manuscript in preparation (2023).

2. **S. Chattopadhyay** and S. Majumdar, "Tuning of encoded memory in adhesive granular gels by an external drive", to be submitted for publication (2023).

3. **S. Chattopadhyay** and S. Majumdar, "Inter-particle adhesion induced strong mechanical memory in a dense granular suspension", Journal of Chemical Physics 156(24), 241102 (2022).

4. **S. Chattopadhyay**, S. Nagaraja, and S. Majumdar, "Effect of adhesive interaction on strain stiffening and dissipation in granular gels undergoing yielding" Communications Physics 5, 126 (2022).

5. S. Dhar, **S. Chattopadhyay**, and S. Majumdar, "Signature of jamming under steady shear in dense particulate suspensions", J. Phys.: Condens. Matter, 32 (12), 124002 (2019).

Dr. Sayantan Majumdar
Thesis supervisor

Sebanti Chattopadhyay

Contents

CHAPTER

ONE

Introduction

1.1 Soft matter physics: A general introduction

Soft matter is the term broadly used to characterise materials that are intermediate in behaviour to that of crystalline solids and viscous liquids [1, 2, 3, 4, 5, 6, 7, 8, 9, 10]. In typical soft matter systems, the presence of important mesoscopic hierarchical length-scales, weak interactions and long relaxation timescales, gives rise to many interesting and complex phenomena such as linear and non-linear viscoelasticity, self-organization, memory formation, etc. This field encompasses a wide variety of materials including, but not limited to, gels, emulsions, foams, suspensions, bio-polymers, surfactants and liquid crystals. Consequently, soft materials are ubiquitous in nature with many important applications in food and polymer processing, industries, oil recovery, drug delivery, cosmetics and regenerative medicine, to name a few.

Soft matter systems are also important testing ground for non-equilibrium statistical physics [11, 12] due to slow relaxation processes. In fact, the presence of important mesoscopic lengthscales ensures that many macroscopic properties can be predicted without complete knowledge of the atomic/molecular level details. Soft matter systems are generally disordered with significantly low energy scales for deformation. A fascinating aspect of these systems is their ability to adapt to applied external perturbations. The bulk behavior of many soft matter systems can show interesting stimuli responsive behavior, an example of which is the reversible shear-jamming of dense particulate suspensions [13, 14]. Such stimuli adaptability makes soft matter systems a good candidate for designing smart and adaptive materials with applications such as developing flexible body armors, shock absorbing materials, soft robotics and shape memory polymers [15, 16]. Soft materials are also important systems for understanding catastrophic natural phenomena like landslides and earthquakes.

In this thesis, I have primarily studied a model soft matter system: dense particulate suspensions [17] formed by dispersing solid particles in a Newtonian fluid at high volume fractions. Depending on factors like the size and shape of the particles, particle-poly-dispersity, inter- particle interactions and viscosity of the suspending fluid, such suspensions can have widely varying flow behavior under applied shear. These suspensions are one of the most versatile soft matter systems because not only do they exhibit interesting adaptability to applied perturbations, their bulk behavior can also be tuned very easily. Additionally as athermal dense suspensions are inherently out of equilibrium, they show many surprising collective response which are beyond equilibrium thermodynamics.

1.2 Characteristics of soft matter systems

1.2.1 Mesoscopic sizes

The constituents of common soft matter systems have sizes that are in the range of a few nanometers (nm) (for example polymer chains, surfactant molecules, etc) to a few micrometers (μm)(for example, colloidal particles). More recently, granular systems with particles in the size range of a few microns to hundreds of micron are also categorized as soft materials. In general, systems for which many of the properties can be described using mesoscopic lengthscales are generally studied under the formulation of soft matter physics. At these length scales, quantum effects are unimportant but thermal energy is relevant. These length scales, being much larger than atomic/molecular lengthscales, can be probed easily using different types of techniques like optical [18] and electron microscopy, X-ray diffraction, etc [19]. These properties of soft materials enable us to visually probe them under static as well as dynamic conditions.

1.2.2 Weak inter- constituent interactions

While inter-atomic interactions are extremely strong, with strengths of the order of electron volts, the interactions at the mesoscopic lengthscales (inter-constituent interactions) of soft matter systems are generally much weaker. Consequently, thermal energy plays a significant role. Some of the most common interactions in soft matter systems [20] are given below:

- **Van der Waals interaction:** This is a long range attractive interaction between molecules that can have broadly three types of origins: the Keesom interaction happens between permanent dipolar molecules, Debye interaction happens between a permanent and a temporary dipole and London dispersion interaction happens between two temporary or induced dipoles. Temporary or induced dipoles happen when a non-polar molecule (which can be polarized) develops a transient dipole due to fluctuations. All three interaction potentials have a $1/r^6$ variation with the separation (r) between the two point particles.

- **Hard-core (excluded volume) repulsive interaction:** This is a short ranged repulsive interaction between two solid bodies. Following from Pauli's exclusion principle, solid bodies cannot inter-penetrate. This interaction, thus, only comes into picture when the particle surfaces approach very close to each other. The

typical form of the interaction potential from a hard core repulsion between two spherical particles of radius R is as follows:

$$V(r) = \infty \text{ for } r \leq R$$
$$V(r) = 0 \text{ for } r > R$$

- **Electrostatic repulsive interaction:** This is a repulsive interaction experienced by particles having similar charges on their surfaces. This type of repulsion is often used to stabilize colloidal dispersions and prevents the particles from agglomerating. Adding salt to the dispersing medium can modify the Debye layer around the particles, and in turn modify the repulsion between the particles in the suspension. [21]

Origin of the softness of soft materials: The mechanical modulus of a system, that defines its degree of rigidity, is given by the ratio of the interaction potential and the typical lengthscale of the system. The combination of mesoscopic lengthscales and weak interactions results in a much smaller modulus for soft matter systems as compared to conventional solids like metals (where the typical lengthscales are in angstrom and the interactions are much stronger). The smaller modulus makes soft materials to deform significantly, even under weak perturbations.

1.2.3 Long relaxation timescales

When a system is perturbed by an external stimulus, it triggers a relaxation in the system. The purpose of this relaxation mechanism is to equilibrate the system by relaxing the excess stress in the system. Typical relaxation mechanisms involve rearrangement and local restructuring of the system. The timescale of such relaxation processes depends on the microscopic details of the system. Due to the large particle sizes, soft matter systems have longer relaxation timescales (of the order of milliseconds to seconds) which allows us to easily probe various non-equilibrium phenomena and evolution in these systems.

1.3 Viscoelasticity

As mentioned earlier, soft matter systems are intermediate to that of conventional solids and fluids. This intermediate mechanical behavior is termed as viscoelasticity. When a solid is deformed, it stores the energy while a liquid under deformation dissipates the

energy. Thus, on removing the applied load, a solid can regain its shape, while a liquid remains in the deformed state. Viscoelastic behavior involves an interplay between the two types of behavior that is crucially determined by the nature of applied deformation such as the rate of deformation, degree of deformation, etc. Rheology (the study of flow and deformation of systems) is used to characterize such viscoelastic flow behavior.

It is well known that elastic solids deform according to the Hooke's law of elasticity for small deformation (linear regime):

$$\sigma = G\gamma$$

where σ is the stress response of the system, γ is the applied strain and G is the modulus of elasticity. The system is reversible under a deformation cycle and regains it's original state after the force is removed. Beyond the linear regime, plasticity sets in and the system gets permanently deformed. On the other hand, Newton's law of viscosity defines the flow behavior of a purely viscous liquid:

$$\sigma = \eta\dot{\gamma}$$

where η is the viscosity of the liquid and $\dot{\gamma}$ is the applied shear rate. For Newtonian liquids, η is only a function of temperature and pressure.

To model the behavior of viscoelastic systems, a spring and a dashpot are used to represent the elastic and viscous components respectively[22]. The simplest model with both elements in series is the Maxwell model (see Fig. 1.1(a)) where both elements are under the same stress during deformation. The net deformation rate in the system can be written as:

$$\dot{\gamma} = \frac{\sigma}{\eta} + \frac{\dot{\sigma}}{G}$$

The other basic model with the elements in parallel is the Kelvin-Voight (KV) model (see Fig. 1.1(b)) where both elements deform together and the net stress in the system is given by the following differential equation:

$$\sigma = \eta\dot{\gamma} + G\gamma$$

In the Maxwell model, after removal of the load, the stress goes to zero after a long time. Thus, the longtime behavior of the system is liquid-like. On the other hand, in the KV model, there is a residual stress in the system even after a long time. Thus, the long time response of the system is solid-like. More realistic linear viscoelastic material models

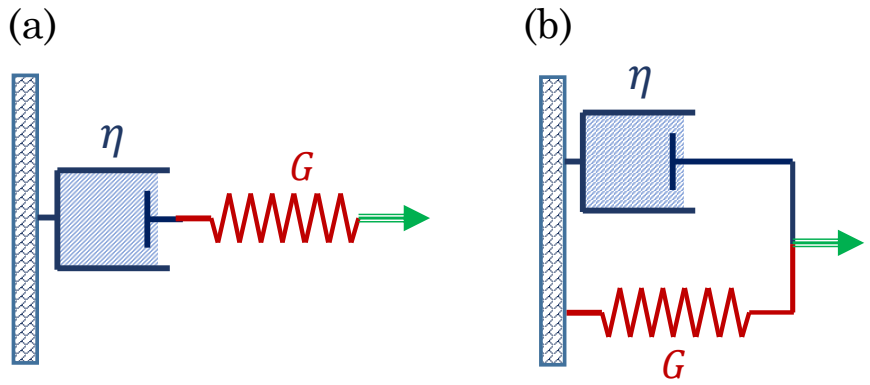

Figure 1.1: Linear viscoelastic models: (a) Maxwell model for viscoelastic liquids. (b) Kelvin-Voight model for viscoelastic solids.

are obtained by adding more spring/dashpot elements or combining a number of Maxwell and Kelvin-Voight elements. These models are useful when the applied stress/strain is small and the system's behavior is linear (reversible). In the non-linear regime, these models are no longer applicable.

To study the flow behavior of soft materials, commonly used protocols are steady shear and oscillatory rheology. In steady shear ramp protocol, the system is subjected to increasing perturbation in the form of shear stress or shear rate while the conjugate quantity (shear rate/stress) is measured. For a Newtonian liquid, the viscosity remains constant with changing stress/rate. Non-Newtonian systems, however, have a rate dependent viscosity and often show shear induced thinning and thickening behavior, as shown in the Fig. 1.2.

For studying the viscoelastic nature, oscillatory protocols are much better suited where the deformation as well as rate dependence can be studied simultaneously. For this, the system is subjected to sinusoidal perturbation:

$$\gamma = \gamma_0 \sin(\omega t)$$

Here, γ_0 is the amplitude of the applied sinusoidal strain γ with a frequency ω. The corresponding shear rate is,

$$\dot{\gamma} = \omega\gamma_0 \cos(\omega t)$$

The elastic component of the stress response will be in phase with γ while the viscous component will be in phase with $\dot{\gamma}$, giving a resultant stress response that is phase shifted with γ as given below (also see Fig. 1.3) [23, 24, 25]:

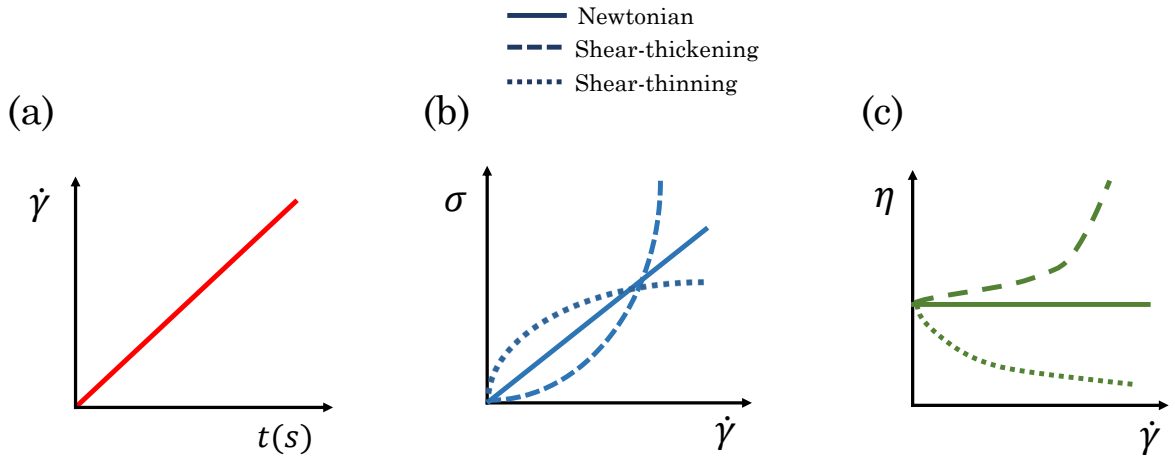

Figure 1.2: (a) A typical steady shear ramp protocol where the shear rate $\dot{\gamma}$ is increasing with time. The corresponding stress response and viscosity for Newtonian, Shear-thinning and thickening systems are shown in (b) and (c), respectively.

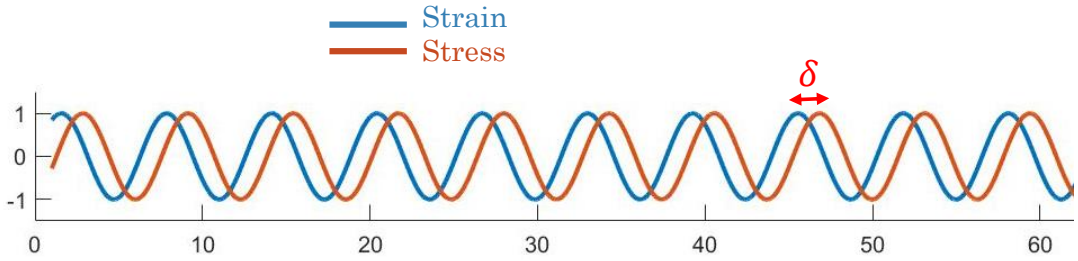

Figure 1.3: Typical stress response for an input sinusoidal oscillatory perturbation. δ indicates the phase shift in the response.

$$\sigma = \sigma_0 \sin(\omega t + \delta)$$

The applied strain amplitude (γ_0) is increased progressively from small to large values and the stress response is noted. Typically, the response of a viscoelastic material under applied oscillatory protocol with increasing strain amplitude is as shown in the Fig. 1.4. The elastic (G') and viscous moduli (G'') are characterizing the in-phase and out of phase components of the response. For a viscoelastic solid, $G' > G''$. Following a linear viscoelastic region, where the moduli are independent of γ_0, the G' starts to drop at an amplitude that is defined as the yield strain of the system. Soon after the yield point, a crossover of the moduli indicates that the system is now predominantly viscous (fluid-like) with $G'' > G'$. The Large Amplitude Oscillatory Shear (LAOS) protocol is a useful technique to study the yielding behavior of soft matter systems. Additionally, the intra cycle stress-strain plots (Lissajous plots) can give information about the intra-cycle energy dissipation and non-linear effects such as strain stiffening or weakening of the system. [26, 27]

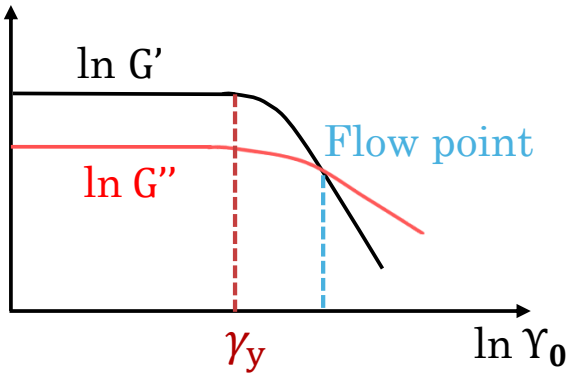

Figure 1.4: Typical LAOS (Large Amplitude Oscillatory Shear) response of a viscoelastic system.

1.4 Related special topics

In this section, we give a brief account of some important topics related to soft materials that we explore in this thesis.

1.4.1 The Jamming transition

Jamming is the phenomena where a fluid undergoes a transition to an arrested solid- like state with a finite yield stress [28, 29, 30, 31, 32, 33, 34, 35, 36, 37, 38]. Many soft matter

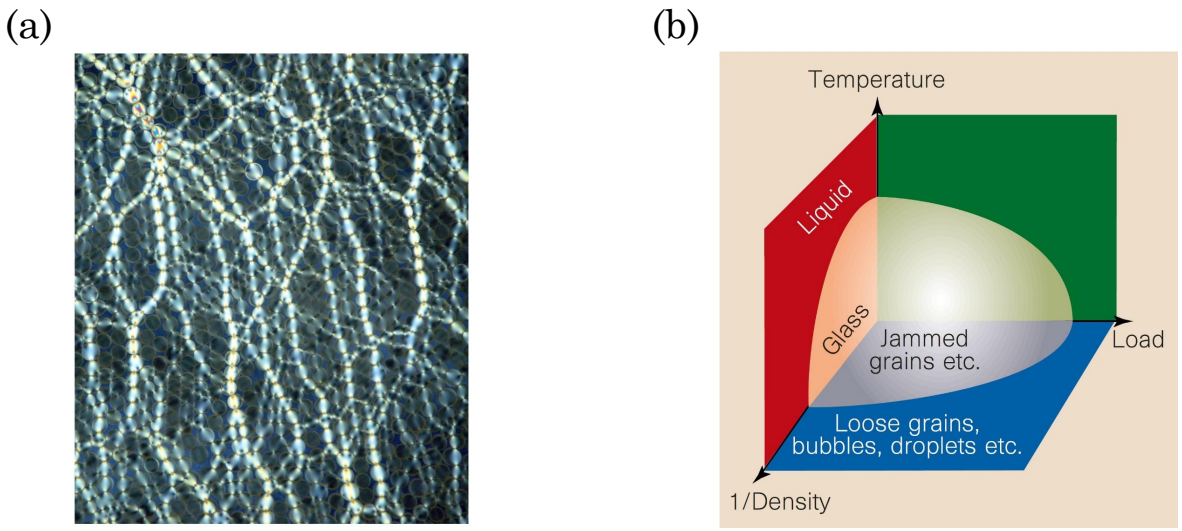

Figure 1.5: (a) Force chains observed in photo-elastic disks (figure is adapted from [28]) (b)The Jamming phase diagram given by Liu and Nagel [29].

systems such as foams, emulsions, suspensions, granular media and glasses exhibit the formation of disordered jammed solids but with distinct underlying mechanisms. Aside from the obvious similarities with conventional solids (for example, load bearing ability), jammed solids have some very unique characteristics. It has been found that in jammed systems, stress propagates through the network of particles called force chains (depicted in Fig. 1.5(a)). Consequently, under an applied load, there is significant stress heterogeneity in the system, with some particles undergoing a lot more stress and some barely experiencing any stress. Another feature of jammed solids is their anisotropic load bearing capacity. While the system is jammed under shear along one direction, a reversal of the shear direction can unjam the solid-like state. Hence jammed solids are referred to as fragile matter[30]. Onset of plasticity and failure under applied load is difficult to predict in these solids, owing to the absence of identifiable defects as the structure is disordered.

A jamming phase diagram was proposed by Liu and Nagel (see Fig. 1.5(b)) to generalize the jamming behavior across different systems based on only a few key parameters. The phase diagram indicated that the jamming transition is accessible through an interplay of three parameters: density of the system, the applied load/stress and the temperature. Trappe et al further generalize the phase diagram [31] by incorporating inter-particle interactions (see Fig. 1.6). In essence, the presence of additional interactions increases the constraints on the flowing state of the system, consequently the system can get jammed more easily. Thus, inter-particle interactions are a crucial parameter to predict the jam-

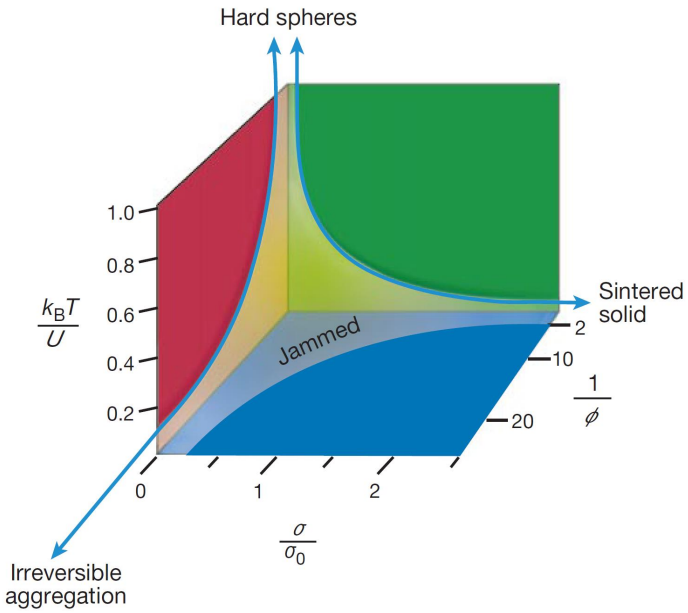

Figure 1.6: Jamming phase diagram proposed by [31] incorporating inter-particle interactions as a general parameter for jamming across attractive systems.

ming behavior of a wide class of soft matter systems. For instance, gels have attractive inter-particle interactions and can form jammed solids at very low volume fractions [31]. On the other hand, hard-sphere suspensions require very high volume fraction of particles (close to random close packing) to form a jammed solid [39, 40].

A lot of recent interest has been on the shear-induced jamming in frictional dense particulate suspensions. The phase diagram for these systems in the parameter plane of stress and particle volume fraction is shown in Fig. 1.7. This phase diagram significantly differs from those shown in Fig. 1.5 and 1.6. In Fig. 1.8, we show the work by Singh et al, establishing the dependence of ϕ_J (the jamming volume fraction) on the nature of inter-particle interactions, thus highlighting the importance of inter-particle interactions in controlling the jamming transition.

1.4.2 Yielding in disordered materials

Yielding is the phenomena where a solid-like material, under applied stress, starts flowing like a viscous liquid. Diverse disordered materials close to jamming show a finite elasticity under small perturbations. When the applied perturbations become large enough, plasticity and irreversible deformations take place as the material yields [41, 42, 43, 44]. An example of shear induced yielding of a colloidal gel is shown in the Fig. 1.9([43]).

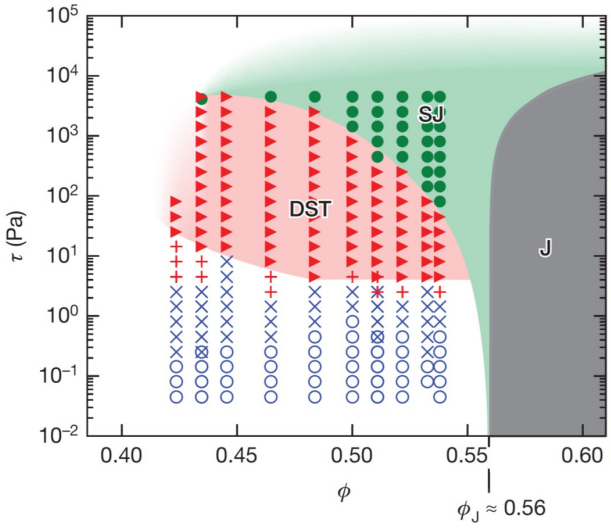

Figure 1.7: The jamming phase diagram for dense suspensions of Cornstarch particles in water with the critical jamming volume fraction ϕ_J indicated in the figure. The figure is adapted from [39].

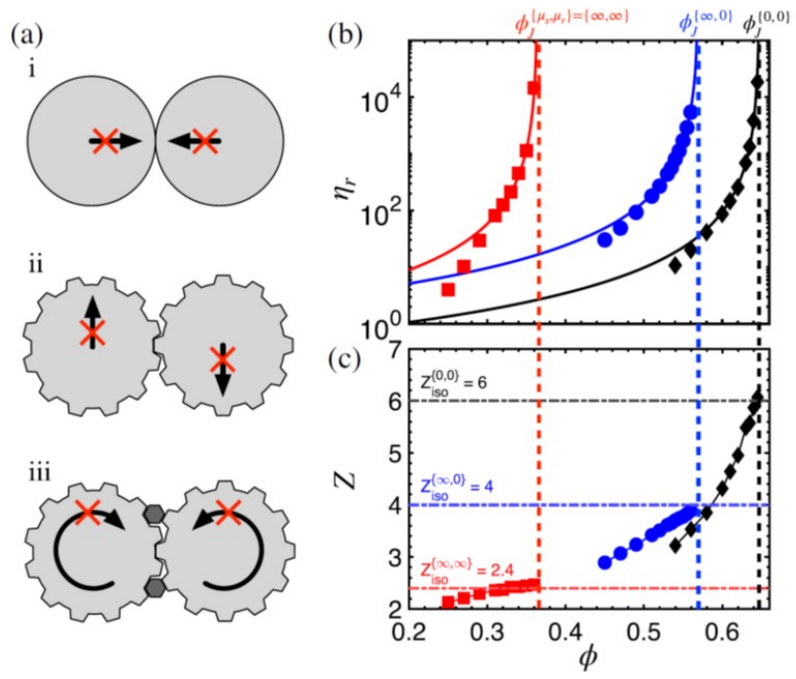

Figure 1.8: Figure shows the lowering of the jamming volume fraction ϕ_J due to constraints imposed by the presence of additional inter-particle interactions such as friction and adhesion. The figure is adapted from [40]. The colors on the right panel correspond to the three types of constraints depicted on the left panel as follows: black diamonds for (i), blue circles for (ii), and red squares for (iii).

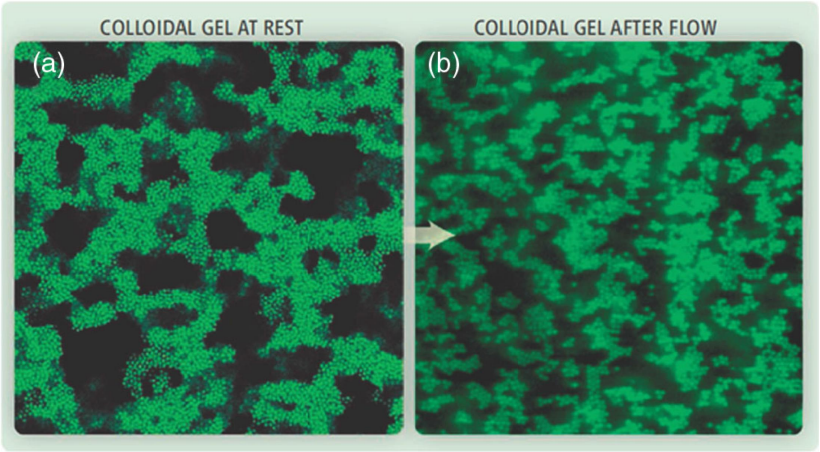

Figure 1.9: Shear-induced yielding of a colloidal gel network indicated by the disintegration of the particle networks that give rise to yield stress in the system. Figure is adapted from [43].

As opposed to crystalline systems, due to lack of translational symmetry there is no obvious structural precursor (similar to crystalline defects) of yielding in disordered materials [45, 46] as also mentioned earlier. This makes the understanding of the yielding phenomena in amorphous solids particularly challenging.

Yielding is also accompanied by an enhanced energy dissipation [43, 47] that eventually leads to fluidization/fracture of the material. Studies have reported that systems often accumulate minor failures and cracks before a system wide catastrophic failure occurs [48, 49]. Identifying these micro-failures in materials are crucial for many practical applications. Yielding in amorphous solids plays an important role in material processing industries, as well as, in catastrophic natural phenomena like landslides and earthquakes [50, 51, 52].

1.4.3 Out of equilibrium behavior: Memory formation

Athermal systems are inherently out of equilibrium. If left undisturbed, these systems have no means of exploring their phase space and are stuck in their prepared configuration. Thus, they can retain a memory of their preparation and past perturbations. Interestingly, these systems can also be trained to remember an external stimulus/perturbation, which can be read out later using suitable protocols. The system encodes a memory of the applied perturbation as an imprint in its material structure.

Repeated cyclic perturbation protocols have been widely used to encode memories in many of these systems. Such perturbations in the form of shear, temperature change, elec-

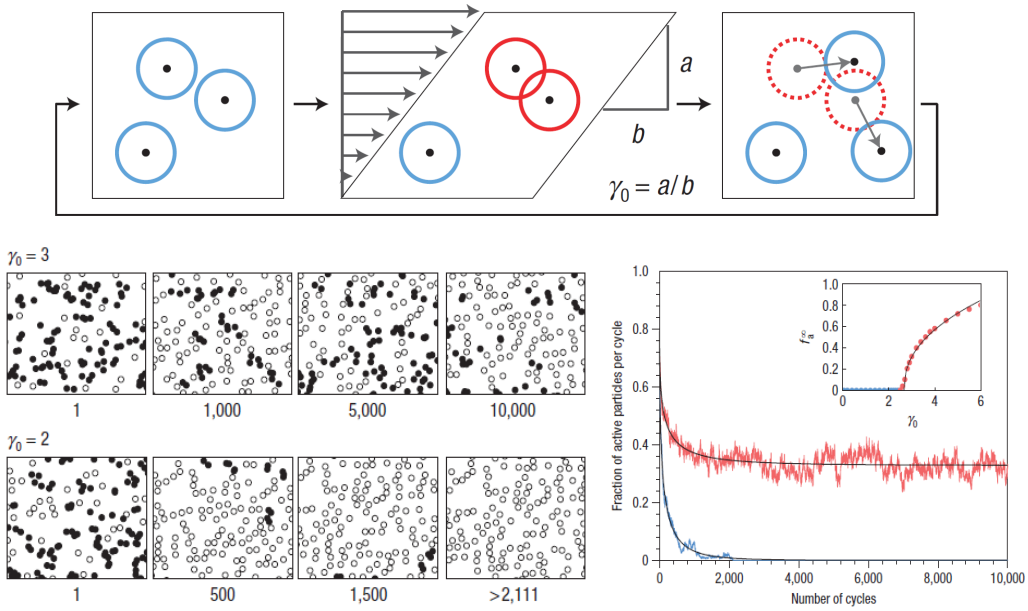

Figure 1.10: Schematic shows the random organization under applied shear for particles in a suspension. Bottom row indicates the two types of steady states that are formed by the system as explained in [53]. Figures are adapted from [53].

trical/magnetic fields [54] have been encoded into dilute granular suspensions [53, 55, 56], glasses [57, 58] and charge density wave conductors [59, 60], respectively. As a result of the repeated driving, the system undergoes random organization and reaches a reversible state that remains undisturbed/unperturbed under further cycling at the same drive. Stroboscopic imaging of the system and subsequent mean squared displacement (MSD) calculations have been used to establish these reversible states (commonly known as the absorbing states) in simulations, as well as, experimental studies on dilute granular suspensions (see Fig. 1.10 and 1.11). In these systems, once an absorbing state is developed for a training strain (γ_T), the system is reversible for all strain values $\gamma \leq \gamma_T$ (This is known as ordering of states). Further driving up to this strain will not cause any new collisions/dissipation in the system. Hence, the system's state is reversible. The underlying dynamics is overdamped and there is no storage of elastic energy in the system. Note that the system is reversible in the sense of reversibility of particle trajectories and not in terms of storing energy. When driven beyond γ_T, there is a sudden onset of particle collisions in the system, thus exhibiting a reversible to irreversible transition (RIT) across γ_T. So, under a sequence of increasing strain values, the trained system's stroboscopic MSD will show a kink at γ_T indicating a memory in the system as shown in Fig. 1.11.

Similar reversible states are also formed by jammed disordered systems (like glasses,

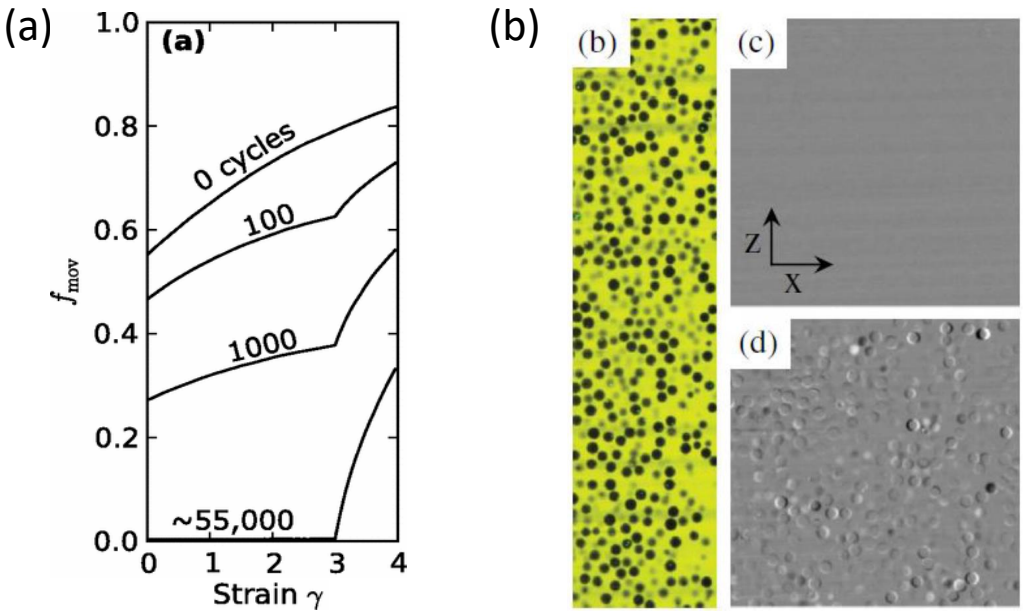

Figure 1.11: (a) Figure shows the development of a memory signature corresponding to the training strain of 3. The fraction of moving particles (f_{mov}) goes to zero with increasing cycles of training, indicating that an absorbing state is formed upto a strain of 3. When the system is subjected to cycles of increasing strain to read out the encoded memory, it remains reversible upto 3 due to the training induced absorbing state, beyond which a sharp rise in f_{mov} indicates that the system has undergone irreversible collisions. This reversible to irreversible transition beyond the training strain is a signature of encoded memory in the system. Figure is adapted from [55]. (b) Experimental observation of memory formation in dilute suspensions. Figure is adapted from [56].

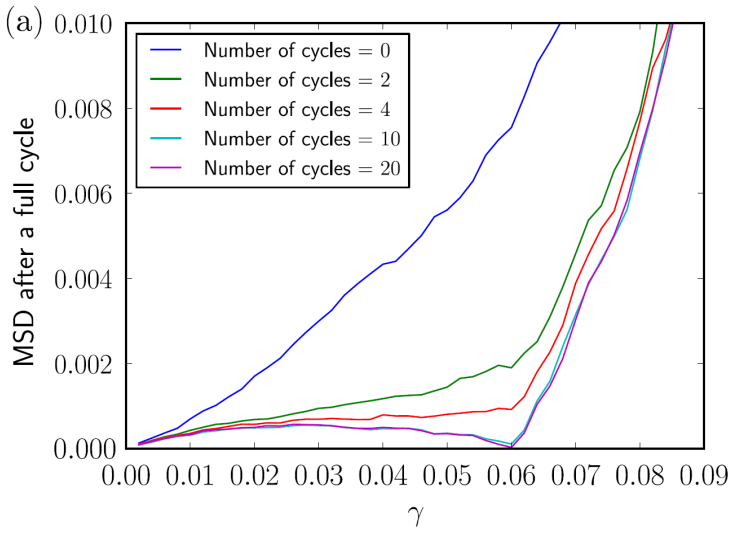

Figure 1.12: Figure adapted from [62] shows MSD of a disordered being trained at a strain of 0.06 with increasing number of cycles as indicated by the color scheme.

gels, etc.). However, in these cases, particles are in enduring contact throughout the perturbation cycles so the reversible states are not collision free. Also, it has been reported that these systems do not obey the ordering of states, rather their trained state exhibits a loop reversibility. This difference in the nature of the reversible state has the following important consequence: In case of dilute suspensions, once an absorbing state is formed at an amplitude, the system is reversible for all smaller amplitudes as well (see Fig. 1.11). But in disordered solids, the system is loop reversible at the training strain, so, for smaller applied strain values, the system need not be reversible (see Fig. 1.12). This difference is evident in the MSD plots for both cases as shown in Fig. 1.11(a) and 1.12. Simulations have proposed an energy landscape based picture for the reversibility in disordered solids, as explained in [61, 62, 63]. Recent reports have also explored memory formation across the yield point of disordered solids [64, 65].

1.4.4 Discontinuous shear thickening in dense suspensions

Dense suspensions show an array of interesting non-linear stress response [66, 67, 68]. Under shear, the viscosity of the suspension can either decrease (a phenomena called shear-thinning) or increase (a phenomena called shear thickening [69]). At sufficiently large volume fraction ϕ, many dense suspensions show discontinuous shear-thickening (DST) [70, 71, 72, 73, 74, 75] when the suspension viscosity rapidly increases by more than an order of magnitude under an applied stress (σ) larger than a stress onset (σ_0)

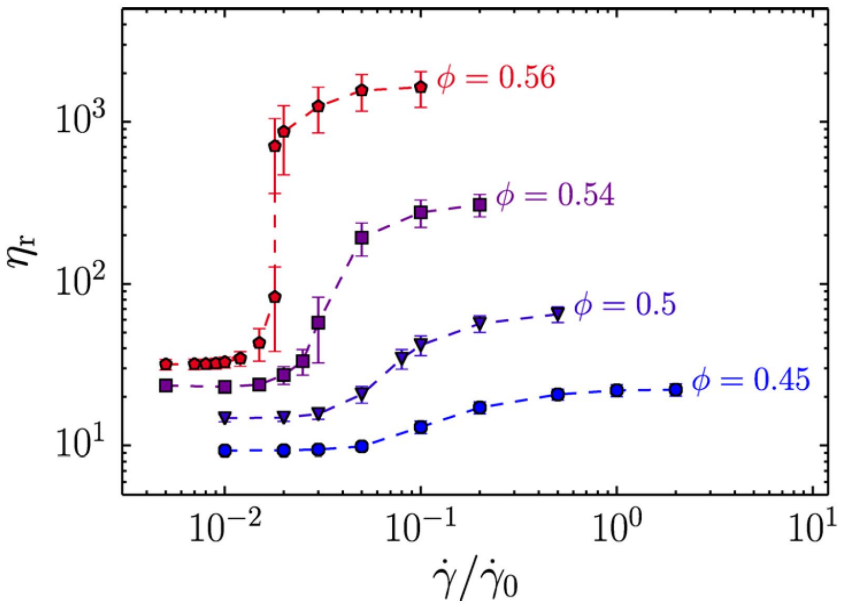

Figure 1.13: Figure depicts continuous and discontinuous shear-thickening with increasing volume fraction. Figure is adapted from [83].

[76] (see Fig. 1.13). Upon removal of the applied stress, the viscosity quickly drops and approaches the initial value. This striking effect has triggered a lot of recent interest in the study dense suspensions [13, 77, 78, 79, 80]. Such control of suspension viscosity by an external stress has made these systems potential candidates for designing smart and stimuli responsive materials that can find wide range of applications [81, 82].

1.4.5 Orthogonal vibration and jammed systems

Athermal jammed systems are structurally arrested with limited phase space accessibility. Apart from applying external shear to these systems, it has been found that applying orthogonal vibration is an useful technique to tune the effective inter-particle interactions in these far from equilibrium systems. Vibrated dry granular media has been widely studied but the flow of athermal dense suspensions under superimposed orthogonal vibrations is the subject of current interest [84, 85, 86, 87]. Such a setup has been used, so far, to tune the Discontinuous Shear Thickening properties in dense granular suspensions (see Fig. 1.14), as well as, frictional yield stress (see Fig. 1.15). Thus, orthogonal vibration provides an external handle to control the flow behavior of jammed systems.

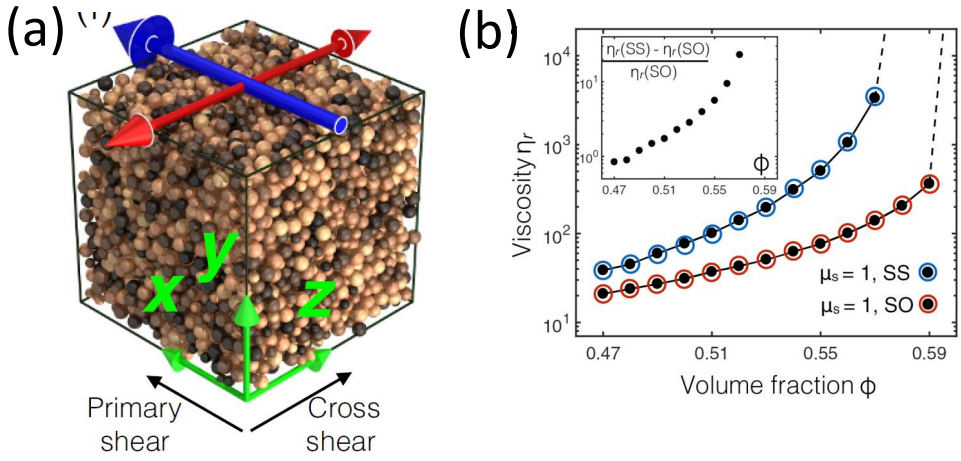

Figure 1.14: Figure adapted from [86] shows a representation of orthogonal vibration applied to a system in (a) and in (b) depicts the reduction in the viscosity of the suspension as a result of applied vibration.

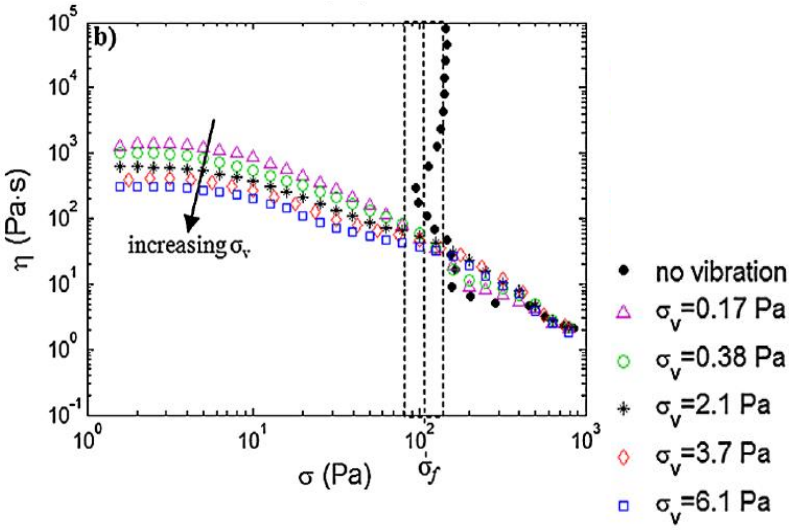

Figure 1.15: Figure adapted from [84] shows the reduction of frictional yield stress under applied vibration.

1.5 Thesis Overview

The construction of this thesis is in the following manner:

Chapter 2: This chapter discusses the main experimental techniques used in this thesis, including Rheology with in-situ optical imaging, Scanning Electron and Confocal Microscopy. It also covers details of the sample preparation techniques used in the subsequent chapters.

Chapters 3-7: These chapters elaborate the different problems studied in this thesis. A brief summary of these chapters is included in the Preface.

Chapter 8: This chapter concludes the thesis with a brief summary of the work done, followed by an outlook to the possible future research directions.

Bibliography

[1] Wilhelm Flügge. *Viscoelasticity*. Springer, Berlin, Germany.

[2] A. Wineman. Nonlinear Viscoelastic Solids—A Review. *Math. Mech. Solids*, 14(3):300–366, May 2009.

[3] Daan Frenkel. Soft condensed matter. *Physica A*, 313(1):1–31, October 2002.

[4] T. C. Lubensky. Soft condensed matter physics. *Solid State Commun.*, 102(2):187–197, April 1997.

[5] Sidney R. Nagel. Experimental soft-matter science. *Rev. Mod. Phys.*, 89(2):025002, Apr 2017.

[6] Brochard-Wyart Francoise, Nassoy Pierre, and Puech Pierre-Henri. *Essentials of Soft Matter Science*. CRC Press, Boca Raton, FL, USA, September 2019.

[7] Richard A. L. Jones. *Soft Condensed Matter*. OUP, Oxford, England, UK.

[8] Thomas A. Witten. Insights from soft condensed matter. *Rev. Mod. Phys.*, 71(2):S367–S373, March 1999.

[9] Masao Doi. *Soft matter physics*. Oxford University Press, USA, 2013.

[10] Jasper van der Gucht. Grand Challenges in Soft Matter Physics. *Front. Phys.*, 6:410242, August 2018.

[11] Dapeng Bi, Silke Henkes, Karen E. Daniels, and Bulbul Chakraborty. The Statistical Physics of Athermal Materials. *Annu. Rev. Condens. Matter Phys.*, 6(1):63–83, March 2015.

[12] S. Ciliberto. Experiments in Stochastic Thermodynamics: Short History and Perspectives. *Phys. Rev. X*, 7(2):021051, June 2017.

[13] B. M. Guy, M. Hermes, and W. C. K. Poon. Towards a Unified Description of the Rheology of Hard-Particle Suspensions. *Phys. Rev. Lett.*, 115(8):088304, August 2015.

[14] Deng Pan, Yinqiao Wang, Hajime Yoshino, Jie Zhang, and Yuliang Jin. A review on shear jamming. *arXiv*, June 2023.

[15] Eric Brown and Heinrich M. Jaeger. Shear thickening in concentrated suspensions: phenomenology, mechanisms and relations to jamming. *Rep. Prog. Phys.*, 77(4):046602., April 2014.

[16] Mohammad Zarei and Jamal Aalaie. Application of shear thickening fluids in material development. *J. Mater. Res. Technol.*, 9(5):10411–10433, September 2020.

[17] Christopher Ness, Ryohei Seto, and Romain Mari. The Physics of Dense Suspensions. *Annu. Rev. Condens. Matter Phys.*, 13(1):97–117, March 2022.

[18] Taewoo Lee, Bohdan Senyuk, Rahul P. Trivedi, and Ivan I. Smalyukh. Optical Microscopy of Soft Matter Systems. In *Fluids, Colloids and Soft Materials*, pages 165–185. John Wiley & Sons, Inc, Hoboken, NJ, USA, May 2016.

[19] Redouane Borsali and Robert Pecora. *Soft-Matter Characterization*. January 2008.

[20] Jacob N. Israelachvili. *Intermolecular and Surface Forces*. Elsevier, Academic Press, 2011.

[21] Duncan J. Shaw. *Introduction to Colloid and Surface Chemistry*. Butterworth-Heinemann, Oxford, England, UK, 1992.

[22] Thomas Mezger. *The Rheology Handbook*. Vincentz Network, August 2020.

[23] Christopher W. Macosko. *Rheology: Principles, Measurements, and Applications*. Wiley, Hoboken, NJ, USA, December 1996.

[24] Ronald G. Larson and Ronald G. Larson. *The Structure and Rheology of Complex Fluids*. Oxford University Press, Oxford, England, UK, January 1999.

[25] Howard A. Barnes. *A Handbook of Elementary Rheology*. University of Wales, Institute of Non-Newtonian Fluid Mechanics.

[26] Randy H. Ewoldt, A. E. Hosoi, and Gareth H. McKinley. New measures for characterizing nonlinear viscoelasticity in large amplitude oscillatory shear. *J. Rheol.*, 52(6):1427–1458, November 2008.

[27] Kyu Hyun, Manfred Wilhelm, Christopher O. Klein, Kwang Soo Cho, Jung Gun Nam, Kyung Hyun Ahn, Seung Jong Lee, Randy H. Ewoldt, and Gareth H. McKinley. A review of nonlinear oscillatory shear tests: Analysis and application of large amplitude oscillatory shear (LAOS). *Prog. Polym. Sci.*, 36(12):1697–1753, December 2011.

[28] Dapeng Bi, Jie Zhang, Bulbul Chakraborty, and R. P. Behringer. Jamming by shear. *Nature*, 480:355–358, December 2011.

[29] Andrea J. Liu and Sidney R. Nagel. Jamming is not just cool any more. *Nature*, 396(6706):21–22, November 1998.

[30] M. E. Cates, J. P. Wittmer, J.-P. Bouchaud, and P. Claudin. Jamming, Force Chains, and Fragile Matter. *Phys. Rev. Lett.*, 81(9):1841–1844, August 1998.

[31] V. Trappe, V. Prasad, Luca Cipelletti, P. N. Segre, and D. A. Weitz. Jamming phase diagram for attractive particles. *Nature*, 411:772–775, June 2001.

[32] Liu Andrea J. and Nagel Sidney R. *Jamming and Rheology*. CRC Press, Boca Raton, FL, USA, December 1969.

[33] Michael Dennin. Discontinuous jamming transitions in soft materials: coexistence of flowing and jammed. *J. Phys.: Condens. Matter*, 20(28):283103, June 2008.

[34] M. van Hecke. Jamming of soft particles: geometry, mechanics, scaling and isostaticity. *J. Phys.: Condens. Matter*, 22(3):033101, December 2009.

[35] Andrea J. Liu and Sidney R. Nagel. Granular and jammed materials. *Soft Matter*, 6(13):2869–2870, 2010.

[36] Andrea J. Liu and Sidney R. Nagel. The Jamming Transition and the Marginally Jammed Solid. *Annu. Rev. Condens. Matter Phys.*, 1(1):347–369, July 2010.

[37] Nagel Liu. *Jamming and Rheology:Constrained Dynamics on Microscopic and Macroscopic Scales*. Taylor & Francis, Andover, England, UK, April 2014.

[38] Robert P. Behringer and Bulbul Chakraborty. The physics of jamming for granular materials: a review. *Rep. Prog. Phys.*, 82(1):012601, November 2018.

[39] Ivo R. Peters, Sayantan Majumdar, and Heinrich M. Jaeger. Direct observation of dynamic shear jamming in dense suspensions. *Nature*, 532:214–217, April 2016.

[40] Abhinendra Singh, Christopher Ness, Ryohei Seto, Juan J. de Pablo, and Heinrich M. Jaeger. Shear Thickening and Jamming of Dense Suspensions: The ``Roll" of Friction. *Phys. Rev. Lett.*, 124(24):248005, June 2020.

[41] Michael L. Falk and J. S. Langer. Deformation and Failure of Amorphous, Solidlike Materials. *Annu. Rev. Condens. Matter Phys.*, 2(1):353–373, Feb 2011.

[42] Ludovic Berthier, Giulio Biroli, Jean-Philippe Bouchaud, Luca Cipelletti, and Wim van Saarloos. *Dynamical Heterogeneities in Glasses, Colloids, and Granular Media: 150 (International Series of Monographs on Physics)*. OUP, Oxford, England, UK, Jul 2011.

[43] Daniel Bonn, Morton M. Denn, Ludovic Berthier, Thibaut Divoux, and Sébastien Manneville. Yield stress materials in soft condensed matter. *Rev. Mod. Phys.*, 89(3):035005, Aug 2017.

[44] P. Coussot. Yield stress fluid flows: A review of experimental data. *J. Non-Newtonian Fluid Mech.*, 211:31–49, Sep 2014.

[45] Sylvain Patinet, Damien Vandembroucq, and Michael L Falk. Connecting local yield stresses with plastic activity in amorphous solids. *Physical review letters*, 117(4):045501, 2016.

[46] D. Richard, M. Ozawa, S. Patinet, E. Stanifer, B. Shang, S. A. Ridout, B. Xu, G. Zhang, P. K. Morse, J.-L. Barrat, L. Berthier, M. L. Falk, P. Guan, A. J. Liu, K. Martens, S. Sastry, D. Vandembroucq, E. Lerner, and M. L. Manning. Predicting plasticity in disordered solids from structural indicators. *Phys. Rev. Mater.*, 4(11):113609, Nov 2020.

[47] K. van der Vaart, Yasser Rahmani, Rojman Zargar, Zhibing Hu, Daniel Bonn, and Peter Schall. Rheology of concentrated soft and hard-sphere suspensions. *J. Rheol.*, 57(4):1195, Jun 2013.

[48] Stefano Aime, Laurence Ramos, and Luca Cipelletti. Microscopic dynamics and failure precursors of a gel under mechanical load. *Proc. Natl. Acad. Sci. U.S.A.*, 115(14):3587–3592, April 2018.

[49] Luca Cipelletti, Kirsten Martens, and Laurence Ramos. Microscopic precursors of failure in soft matter. *Soft Matter*, 16(1):82–93, 2020.

[50] Pradip K Bera, Sayantan Majumdar, Guy Ouillon, Didier Sornette, and Ajay K Sood. Quantitative earthquake-like statistical properties of the flow of soft materials below yield stress. *Nature communications*, 11(1):1–9, 2020.

[51] Douglas J Jerolmack and Karen E Daniels. Viewing earth's surface as a soft-matter landscape. *Nature Reviews Physics*, 1(12):716–730, 2019.

[52] P. A. Johnson, B. Ferdowsi, B. M. Kaproth, M. Scuderi, M. Griffa, J. Carmeliet, R. A. Guyer, P.-Y. Le Bas, D. T. Trugman, and C. Marone. Acoustic emission and microslip precursors to stick-slip failure in sheared granular material. *Geophys. Res. Lett.*, 40(21):5627–5631, November 2013.

[53] Laurent Corté, P. M. Chaikin, J. P. Gollub, and D. J. Pine. Random organization in periodically driven systems - Nature Physics. *Nat. Phys.*, 4:420–424, May 2008.

[54] Nathan C Keim, Joseph D Paulsen, Zorana Zeravcic, Srikanth Sastry, and Sidney R Nagel. Memory formation in matter. *Reviews of Modern Physics*, 91(3):035002, 2019.

[55] Nathan C. Keim and Sidney R. Nagel. Generic Transient Memory Formation in Disordered Systems with Noise. *Phys. Rev. Lett.*, 107(1):010603, Jun 2011.

[56] Joseph D. Paulsen, Nathan C. Keim, and Sidney R. Nagel. Multiple Transient Memories in Experiments on Sheared Non-Brownian Suspensions. *Phys. Rev. Lett.*, 113(6):068301, Aug 2014.

[57] K Jonason, E Vincent, J Hammann, JP Bouchaud, and P Nordblad. Memory and chaos effects in spin glasses. *Physical Review Letters*, 81(15):3243, 1998.

[58] Ling-Nan Zou and Sidney R. Nagel. Glassy Dynamics in Thermally Activated List Sorting. *Phys. Rev. Lett.*, 104(25):257201, Jun 2010.

[59] RM Fleming and LF Schneemeyer. Observation of a pulse-duration memory effect in k 0.30 moo 3. *Physical Review B*, 33(4):2930, 1986.

[60] SN Coppersmith, TC Jones, LP Kadanoff, A Levine, JP McCarten, SR Nagel, SC Venkataramani, and Xinlei Wu. Self-organized short-term memories. *Physical Review Letters*, 78(21):3983, 1997.

[61] Davide Fiocco, Giuseppe Foffi, and Srikanth Sastry. Oscillatory athermal quasistatic deformation of a model glass. *Phys. Rev. E*, 88(2):020301, Aug 2013.

[62] Davide Fiocco, Giuseppe Foffi, and Srikanth Sastry. Encoding of Memory in Sheared Amorphous Solids. *Phys. Rev. Lett.*, 112(2):025702, Jan 2014.

[63] Monoj Adhikari and Srikanth Sastry. Memory formation in cyclically deformed amorphous solids and sphere assemblies. *Eur. Phys. J. E*, 41(9):1–17, Sep 2018.

[64] Srimayee Mukherji, Neelima Kandula, A. K. Sood, and Rajesh Ganapathy. Strength of Mechanical Memories is Maximal at the Yield Point of a Soft Glass. *Phys. Rev. Lett.*, 122(15):158001, Apr 2019.

[65] Sebanti Chattopadhyay and Sayantan Majumdar. Inter-particle adhesion induced strong mechanical memory in a dense granular suspension. *J. Chem. Phys.*, 156(24), June 2022.

[66] Eric Brown and Heinrich M. Jaeger. Dynamic Jamming Point for Shear Thickening Suspensions. *Phys. Rev. Lett.*, 103(8):086001, August 2009.

[67] A. Fall, F. Bertrand, D. Hautemayou, C. Mezière, P. Moucheront, A. Lemaître, and G. Ovarlez. Macroscopic Discontinuous Shear Thickening versus Local Shear Jamming in Cornstarch. *Phys. Rev. Lett.*, 114(9):098301, March 2015.

[68] Michiel Hermes, Ben M. Guy, Wilson C. K. Poon, Guilhem Poy, Michael E. Cates, and Matthieu Wyart. Unsteady flow and particle migration in dense, non-Brownian suspensions. *J. Rheol.*, 60(5):905–916, September 2016.

[69] Jeffrey F. Morris. Shear Thickening of Concentrated Suspensions: Recent Developments and Relation to Other Phenomena. *Annu. Rev. Fluid Mech.*, 52(1):121–144, January 2020.

[70] H. A. Barnes. Shear-Thickening ("Dilatancy") in Suspensions of Nonaggregating Solid Particles Dispersed in Newtonian Liquids. *J. Rheol.*, 33(2):329–366, February 1989.

[71] R. L. Hoffman. Discontinuous and Dilatant Viscosity Behavior in Concentrated Suspensions. I. Observation of a Flow Instability. *Transactions of The Society of Rheology*, 16(1):155–173, March 1972.

[72] Jonathan Bender and Norman J. Wagner. Reversible shear thickening in monodisperse and bidisperse colloidal dispersions. *J. Rheol.*, 40(5):899–916, September 1996.

[73] Brent J. Maranzano and Norman J. Wagner. The effects of interparticle interactions and particle size on reversible shear thickening: Hard-sphere colloidal dispersions. *J. Rheol.*, 45(5):1205–1222, September 2001.

[74] Abdoulaye Fall, N. Huang, F. Bertrand, G. Ovarlez, and Daniel Bonn. Shear Thickening of Cornstarch Suspensions as a Reentrant Jamming Transition. *Phys. Rev. Lett.*, 100(1):018301, January 2008.

[75] Qin Xu, Sayantan Majumdar, Eric Brown, and Heinrich M. Jaeger. Shear thickening in highly viscous granular suspensions. *Europhys. Lett.*, 107(6):68004, September 2014.

[76] Subhransu Dhar, Sebanti Chattopadhyay, and Sayantan Majumdar. Signature of jamming under steady shear in dense particulate suspensions. *J. Phys.: Condens. Matter*, 32(12):124002, December 2019.

[77] John R. Royer, Daniel L. Blair, and Steven D. Hudson. Rheological Signature of Frictional Interactions in Shear Thickening Suspensions. *Phys. Rev. Lett.*, 116(18):188301, May 2016.

[78] Jean Comtet, Guillaume Chatté, Antoine Niguès, Lydéric Bocquet, Alessandro Siria, and Annie Colin. Pairwise frictional profile between particles determines discontinuous shear thickening transition in non-colloidal suspensions. *Nat. Commun.*, 8(15633):1–7, May 2017.

[79] Norman J. Wagner and John F. Brady. Shear thickening in colloidal dispersions. *Phys. Today*, 62(10):27–32, October 2009.

[80] Abhinendra Singh, Romain Mari, Morton M. Denn, and Jeffrey F. Morris. A constitutive model for simple shear of dense frictional suspensions. *J. Rheol.*, 62(2):457–468, March 2018.

[81] Young S. Lee, E. D. Wetzel, and N. J. Wagner. The ballistic impact characteristics of Kevlar® woven fabrics impregnated with a colloidal shear thickening fluid. *J. Mater. Sci.*, 38(13):2825–2833, July 2003.

[82] Abhijit Majumdar, Bhupendra Singh Butola, and Ankita Srivastava. Optimal designing of soft body armour materials using shear thickening fluid. *Materials & Design (1980-2015)*, 46:191–198, April 2013.

[83] Romain Mari, Ryohei Seto, Jeffrey F. Morris, and Morton M. Denn. Shear thickening, frictionless and frictional rheologies in non-Brownian suspensions. *J. Rheol.*, 58(6):1693–1724, November 2014.

[84] C. Hanotin, S. Kiesgen de Richter, P. Marchal, L. J. Michot, and C. Baravian. Vibration-induced liquefaction of granular suspensions. *Phys. Rev. Lett.*, 108(19):198301., May 2012.

[85] Neil Y. C. Lin, Christopher Ness, Michael E. Cates, Jin Sun, and Itai Cohen. Tunable shear thickening in suspensions. *Proc. Natl. Acad. Sci. U.S.A.*, 113(39):10774–10778, September 2016.

[86] Christopher Ness, Romain Mari, and Michael E. Cates. Shaken and stirred: Random organization reduces viscosity and dissipation in granular suspensions. *Sci. Adv.*, 4(3), March 2018.

[87] C. Garat, S. Kiesgen de Richter, P. Lidon, A. Colin, and G. Ovarlez. Using good vibrations: Melting and controlled shear jamming of dense granular suspensions. *J. Rheol.*, 66(2):237–256, March 2022.

CHAPTER

TWO

Experimental Techniques

2.1 Introduction

In this thesis I experimentally examine some of the interesting phenomena exhibited by jammed systems (see section 1.4) formed by dense particulate suspensions. I primarily use rheology to obtain the bulk flow behavior of different dense suspensions. Further, I use in-situ optical imaging with rheology to understand the particle/ aggregate level dynamics that generates the observed bulk flow behavior. Additionally, I use Scanning Electron Microscopy (SEM) and Confocal Microscopy techniques to characterize the particles used to form the dense suspensions studied in this thesis.

This chapter gives the relevant details of the above mentioned experimental techniques. I also discuss the sample preparation techniques used in the upcoming chapters.

2.2 Experimental Techniques

2.2.1 Rheology with in-situ optical boundary imaging

For all our rheological measurements, I use a stress controlled rheometer MCR-702 (Anton Paar, Austria). Below are some details regarding the mode of operation of the rheometer and geometries used during measurements. In the subsequent chapters, I refer back to these details wherever necessary.

- **Modes of operation of the rheometer:** The MCR-702 has two motors driving the geometries with the functionality to operate in two modes: counter rotation and separate motor transducer. In the counter rotation (CR) mode, the motors rotate the geometries in opposite directions and the set rotation/perturbation is divided between the two geometries. For example, a 50-50 CR mode will counter rotate both the geometries with the same speed, generating the overall net shear that is set by the user.

  In the separate motor-transducer (SMT) mode, the geometry connected to the top motor is held stationary throughout the measurement and acts as the transducer, whereas the geometry connected to the bottom motor applies the entire set perturbation. For most of our measurements, I use the SMT mode of operation unless specified otherwise.

- **Different geometries used for measurements:** I have extensively used the cone-plate geometry in our measurements (Chapter- 3 to 6). In cone and plate

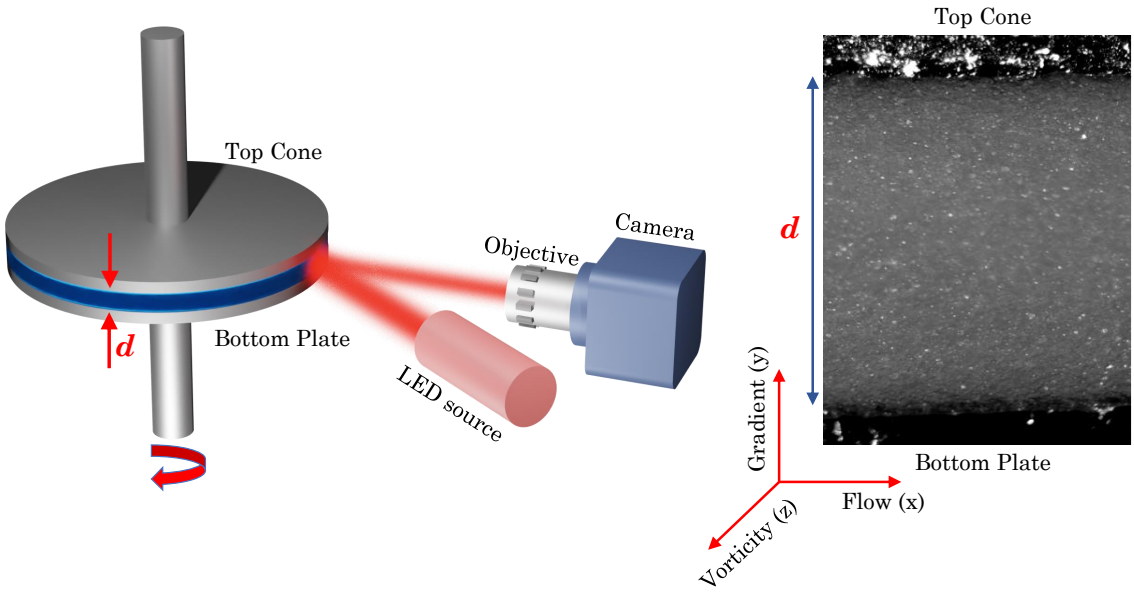

Figure 2.1: Schematic of the rheometer along with the boundary imaging setup. Alongside the setup is an actual boundary image of a dense suspension of Cornstarch particles dispersed in Paraffin oil and loaded in the Cone and Plate geometry. The speckles seen in the image are from the particles.

(C-P), the shear rate remains constant throughout the gap, which ensures that the entire sample is being deformed with a homogeneous stress field. I ensure that the truncation distance of the cone is significantly larger than the average particle size in all the systems studied.

I have also used the Couette (Anton Paar, Austria) geometry for some of our measurements (Chapter-7). I use a profiled surface for the bob to minimize wall slippage. In the subsequent chapters, the Materials and methods sections mention the particular geometry used for the measurements.

- **Sandblasted geometry:** All geometries that I use in the experiments are sandblasted to minimize the slippage at the sample boundaries. Our sandblasted geometries have a roughness scale of about 50 microns.

The schematic of our boundary imaging setup combined with the rheometer is shown in Fig. 2.1. The imaging setup consists of a CCD camera (Lumenera, Lt545R) with a suitable long working distance objective (Mitutoyo). An LED light source is used to illuminate the sample surface. I do a non-standard boundary imaging of our systems. Since our samples are optically opaque, it is difficult to image the system in 3D. Boundary

imaging tracks the features on the sample-air interface which can then be analysed using particle tracking codes to measure the flow field. Generally, I use cone and plate setup for our measurements which has a homogeneous stress field everywhere in the shear gap. Thus, the particle/aggregate level flow fields obtained from the outer surface of the sample are expected to give a good estimate of the behavior in the bulk.

I use Particle imaging velocimetry (PIV) and Kymograph analysis techniques to map out the flow behavior of the system, along with the plasticity and local particle rearrangements under different forcing conditions. More details are provided in the relevant chapters.

2.2.2 Scanning Electron Microscopy (SEM)

Scanning Electron Microscopy is an imaging technique that is broadly used to resolve sub micron features in the sample that cannot be resolved by the conventional optical microscopy techniques. The de-Broglie wavelength for energetic electrons is much smaller than the visible region of the electromagnetic radiation. SEM uses this principle to achieve a much superior resolution.

In the SEM technique, an electron gun, which can be of either thermoionic or field emission type, is used to generate electrons. Using condenser lenses and other supporting optics, a well collimated electron beam is incident on the sample. This electron beam interacts with the sample and generates different types of scattered radiation which is collected using suitable detectors and studied in order to capture various attributes of the sample under study (see Fig. 2.2). SEM can be used to study the particle shapes, size, surface properties, aggregation, porosity, etc.

Alongwith SEM, a technique called cryo-SEM is also used to study samples, generally in presence of a solvent where the sample structure needs to be studied as is. Cryo-SEM uses cryogenic freezing of the samples to be studied, thus allowing a preservation of the structure. This technique is commonly used for biological samples. In our case, I found it difficult to image the micro-structure of the suspensions (Cornstarch particles dispersed in Paraffin oil, see 2.3) using cryo-SEM due to the structures arising from the freezing of the suspending fluid. Hence all our particle characterization is done using SEM.

For characterizing particles in this thesis, I use a Carl-Zeiss Field emission Scanning Electron Microscopy (FESEM). I determine the average particle size, polydispersity and surface properties using FESEM. For this, I prepare a dilute suspension with the particles dispersed in water or ethanol. A drop of this suspension is put on an ITO coated glass plate

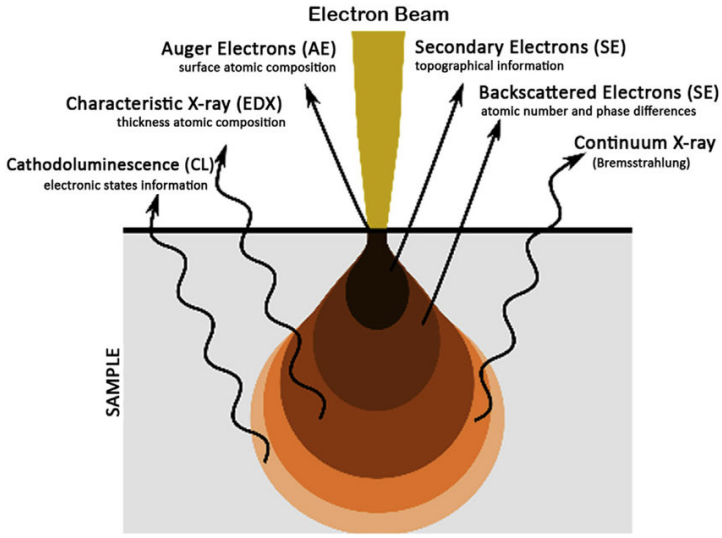

Figure 2.2: Electron beam interaction with a sample [1].

and left to dry overnight. Before loading into the sample stage for FESEM, the sample is first sputter coated with a very thin ($\approx$ 5nm) layer of gold or platinum to ensure a conducting surface. Then the sample is loaded into the instrument for characterization. I use the secondary electron detector to study the surface properties of the sample. (see Fig. 2.2). I show a typical SEM image of Cornstarch particles (Sigma Aldrich) in Fig.2.3.

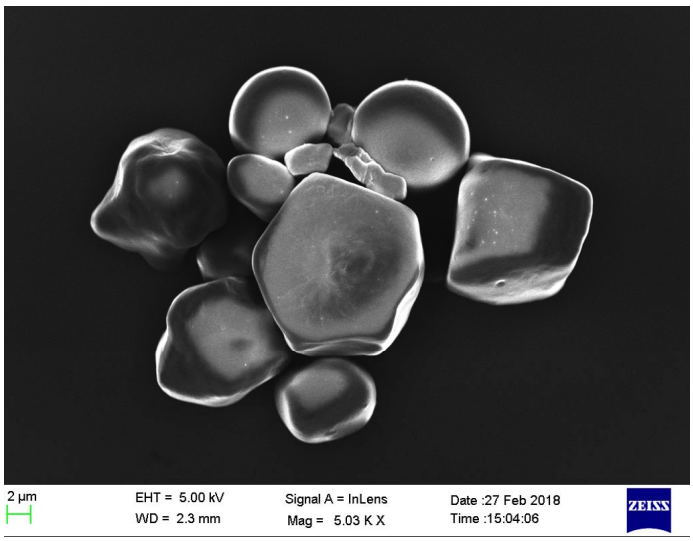

Figure 2.3: Scanning Electron Microscopy (SEM) image of Cornstarch particles (Sigma Aldrich).

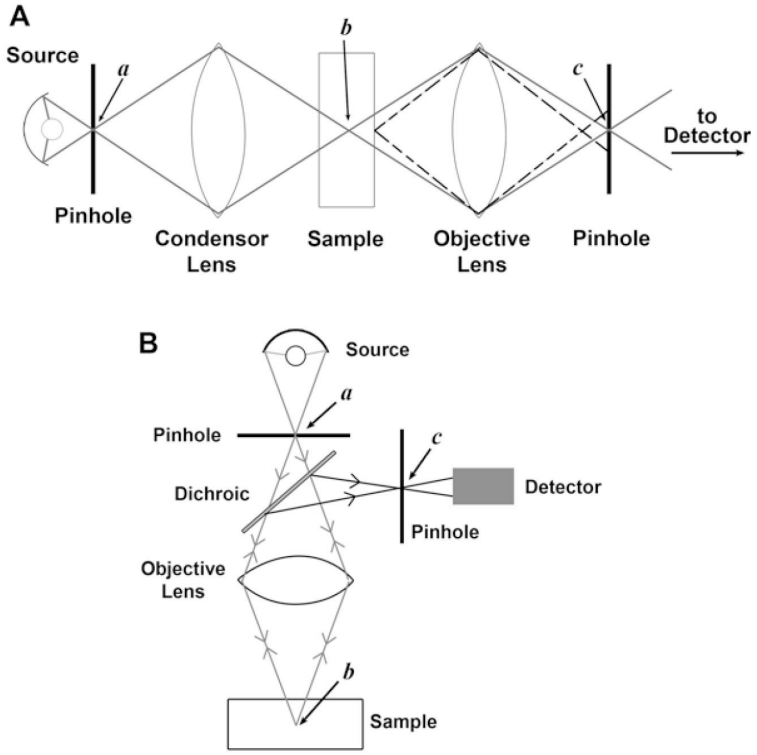

Figure 2.4: Schematic of a Confocal Microscope adapted from [2].

2.2.3 Confocal Microscopy

Another popular technique used in soft matter is Confocal Microscopy. Axial resolution (imaging inside the samples) in conventional optical microscopy techniques is limited by scattering of light from the out of focus planes. In an imaging setup, the sample and the image plane are in conjugate focus. By using a pinhole at the image plane, Confocal Microscopy allows light from only a very small, point-like region of the sample to be focused by the objective, thus eliminating stray light scattered from other areas of the sample (see Fig. 2.4). By scanning the sample in a point by point manner, a 3D reconstruction of the sample can be obtained.

One of the systems that I have widely studied in this thesis is adhesive granular suspensions formed by Cornstarch particles (CS) dispersed in Paraffin oil (PO) (refer to the section 2.3.1 for details of this system). The particles form fractal aggregates due to a solvent mediated adhesion. To verify the fractal nature of the system, I perform confocal imaging of the suspension.

For this, I use the fluorescent ink extracted from Faber Castell Textliner Supefluorescent markers as the dye. The excitation and emission wavelengths are 435 nm and 570

nm, respectively, as obtained from the absorption (using UV-Visible Spectroscopy, Perkin Elmer Lambda 35) and the emission spectrum (using Photoluminescence spectroscopy, Horiba Jobin Yvon – Edison, NJ USA). I use a Leica DMI6000 microscope and a Confocal scanner (Sp8 Germany) for the microscopy. The z-stack images are obtained with a z-spacing of 0.68 μm.

Sample preparation for Confocal Microscopy involves adding the CS particles to a petri dish containing the dye dissolved in ethanol. The solvent is then evaporated at room temperature to get the dyed CS particles. The particles are dried further in a vacuum oven. For making dense suspensions using these dyed CS particles dispersed in oil (with/without surfactant) I follow the mixing protocol described in section 2.3.1.

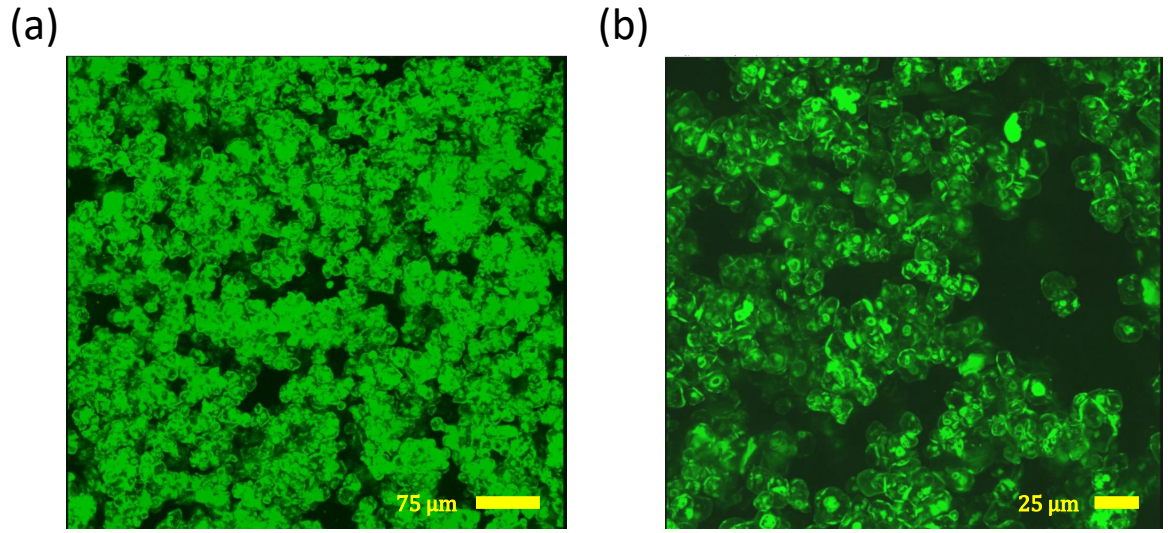

Figure 2.5: Maximum intensity projection of typical confocal z-stack images inside the gravitationally settled bed of Cornstarch particles in Paraffin oil. The magnification is 20X in (a) and 40X in (b).

The XY projection of the 3D stack is showed in the Fig. 2.5 under 20X and 40X magnification. The presence of voids in the structure confirms the fractal nature of the aggregates. The individual confocal images are used to determine the fractal dimension of the CS - Paraffin oil system in Chapter-3.

2.2.4 Particle synthesis

For the study of shear-induced thickening and jamming, I synthesized Polystyrene particles in our lab. The monodisperse Polystyrene (PS) microspheres are synthesized by dispersion polymerization method [3, 4, 5]. Polyvinylpyrrolidone (PVP K-30, Spectrochem,

India) is mixed with a solvent (ethanol/ethanol-water/ethanol with 2-methoxyethanol) inside a 250 ml round bottom flask under continuous stirring at 300 rpm. In another beaker, styrene monomers (TCI, Japan), are mixed with the initiator AIBN (Spectrochem, India). The mixture containing the monomers is poured into the flask maintained at 70 ^{o}C under a constant nitrogen environment. The reaction is carried out for 24 h. The amount of different reactants controls the particle size [4, 5], as summarized in Table 2.1. The PS microspheres formed are cleaned repeatedly using ethanol and water mixture to get rid of chemical impurities/unreacted components from the surface of the particles and are dried and stored for further use. [6]

Size distributions of PS microspheres are characterized by Scanning Electron Microscopy (SEM) technique, using a Ultra Plus FESEM (Zeiss, Germany)(see section 2.2.2). First, a small amount of dried PS microspheres is dispersed in water to form a very dilute suspension. The suspension is then ultrasonicated to break particle clusters, if present. A small drop of this suspension is put on top of an ITO coated glass plate using a micropipette and is left to dry overnight in a covered petri dish to prevent dust accumulation. The slow drying of the dilute suspension ensures formation of mono-layers of particles over a few localized regions on the ITO plate. Since, PS particles are non-conducting, the ITO plate containing the dried suspension droplet is coated with a thin layer of platinum (2 - 3 nm) to increase the conductivity of the sample, as required for SEM imaging. This platinum coated sample is then mounted in the sample chamber of the SEM and is imaged under vacuum.

PS (g)	PVP (g)	AIBN (g)	Ethanol (g)	Water (g)	2-methoxyethanol (g)	d (μm)
14.7	1.44	0.4	78.56	–	–	2.76
15.13	1.75	0.24	27.48	–	62.73	1.21
8	2	0.114	62.82	19.94	–	0.59

Table 2.1: Effect of the amount of reactants and solvent type on particle size. Details of polydispersity are given in Fig. 6.1.

2.3 Sample preparation

In this section, I give the detailed sample preparation methods used in this thesis.

2.3.1 Dense suspensions with adhesive inter-particle interactions

I disperse Cornstarch (CS) particles (Sigma Aldrich) in a non-polar solvent Paraffin oil (PO) (SDFCL). The CS particles are amorphous, having a mean-diameter $\approx$ 15 μm and a polydispersity of 30% . I use SEM images to characterize the CS particle size polydispersity (see Fig. 2.6).

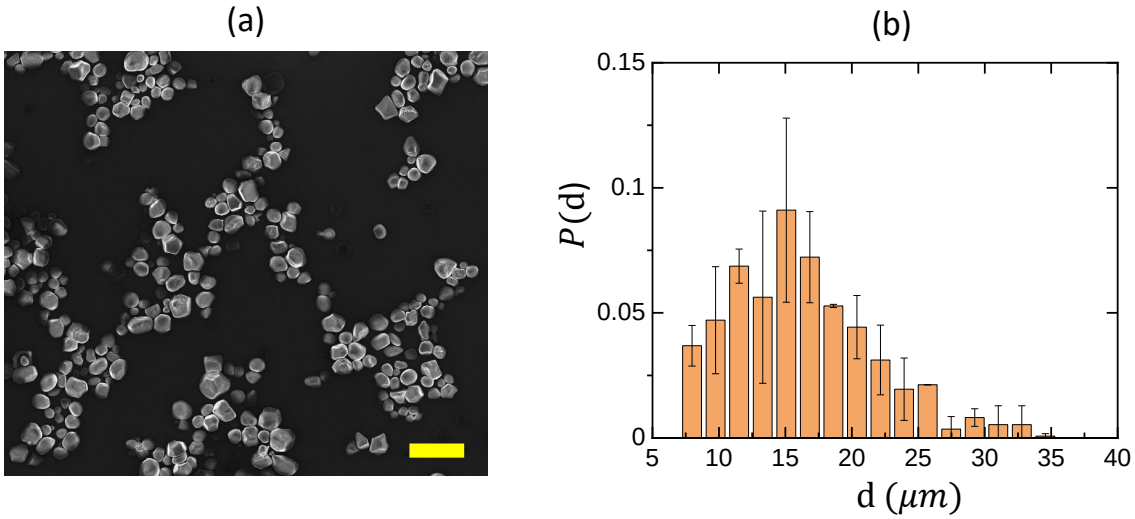

Figure 2.6: (a) A typical SEM image of dry CS particles. The scalebar is 40 μm. (b) Histogram shows the particle size distribution estimated from the SEM images using ImageJ software. I first suitably threshold the grayscale image and convert it into a binary image without introducing any distortion in the image of individual particles. From the binary image, I calculate the area (A) of the individual particles. Due to the non-spherical nature of the particles, for our system I define an effective radius of the particle, $r = \sqrt{A}$ and the diameter $d = 2\sqrt{A}$.I get mean diameter d = 15 μm and polydispersity (standard deviation / mean) = 30 %. Error bars indicate the standard deviation of the four different histograms obtained from different SEM images.

The particles are hydrophilic in nature due to the presence of -OH groups on the surface [7, 8] and hence they are well dispersed in polar solvents like water. In the absence of external stress, hard-core repulsion is the only interaction present in the systems like CS in water (neglecting van der Waals interaction which is always present at very short range). Under this condition, the system is referred to as a repulsive system. However, when dispersed in a non-polar solvent like Paraffin oil, the particles form clusters to minimize the interactions between the surface -OH groups and the hydrophobic solvent, giving rise to a solvent mediated attractive/adhesive interaction between the particles. This adhesion

gives rise to a yield stress in the system [9]. The density of CS particles is ≈ 1.6 g/cc and that for the Paraffin oil (PO) is ≈ 0.89 g/cc at room temperature. Despite this density mismatch, for $\phi > 0.22$ (which is the adhesive loose packing limit for this system [10]), the system develops a yield stress and no particle settling is observed over few days in this volume fraction range.

To prepare the samples, the particles are weighed out and added to the oil in small quantities. For volume fraction $\phi \leq 0.3$, CS powder is gradually added to the oil and mixed thoroughly using a magnetic stirrer. For samples with higher ϕ values, a combination of hand mixing and magnetic stirring is employed to ensure homogeneity of the sample.

I have also studied the following variations in the Cornstarch - Paraffin oil system:

- **Cornstarch in Paraffin oil with added surfactant** : In order to vary the inter-particle adhesive interactions in this system, I use a non-ionic surfactant Span® 60 (Sigma Aldrich). By adding controlled quantities of the surfactant, I are able to systematically tune the adhesion in the system and subsequently study how it affects the flow properties of the suspensions.

  To make the CS suspensions in Paraffin oil with added surfactant, I first weigh out the required amount of surfactant (in powder form) and then crush it in a mortar pestle to get rid of big clusters, if any. Next, CS particles are added and dry mixed thoroughly with the surfactant. After that, the oil is added to the dry mixture and then the sample is mixed well in the mortar pestle followed by mixing with a magnetic stirrer till homogenized. All the samples are degassed overnight under vacuum at room temperature in a desiccator (Borosil)/vacuum oven (Allied Scientific) before rheology.

  Rheological studies verify the effects of adding surfactant on the inter-particle adhesion as shown in Chapter 3 of this thesis. Additionally, I also performed Confocal Microscopy of the system at high surfactant concentrations as shown in Fig. 2.7. Details of sample preparation techniques for Confocal Microscopy are provided in section 2.2.3. When compared with Fig. 2.5, I can clearly see the absence of voids and a significantly well dispersed particle distribution in this case.

- **Cornstarch in Organic oil** : Another adhesive suspension studied in this thesis is formed by dispersing CS particles in a density matched hydrophobic organic liquid (Cargille labs heavy liquid organic series, Cat. No.: 12410, density = 1.6 ± 0.005 g/cc at room temperature). In this case, both the particles and the liquid have the

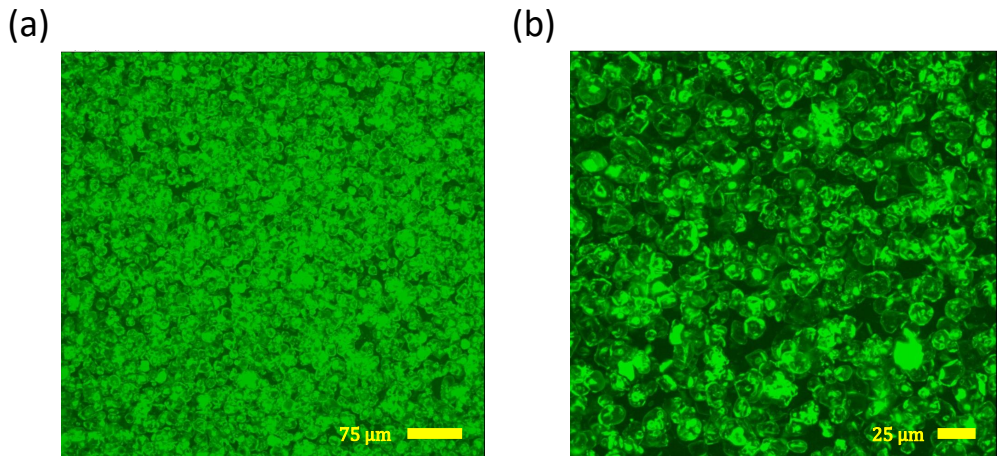

Figure 2.7: Maximum intensity projection of typical confocal z-stack images inside the gravitationally settled bed of Cornstarch particles in Paraffin oil with 0.3% (by mass) added surfactant (Span®60). The magnification is 20X in (a) and 40X in (b).

same density as opposed to the case of CS in Paraffin oil. As explained already, despite the density mismatch in the CS-PO system, the development of yield stress prevents any considerable settling for days after sample is left undisturbed. However, density mismatch could play a role in the flow behavior of the suspension. The sample preparation method is same as that used for CS in Paraffin oil described earlier.

2.3.2 Dense suspensions with repulsive inter-particle interactions

For this thesis, I have studied two types of dense suspensions which have primarily repulsive inter-particle interactions.

- **Cornstarch particles in water and water-glycerol**: CS particles are hydrophilic (as mentioned in section 2.3.1), so when dispersed in either water or water-glycerol mixtures, I get a well dispersed suspension with inter-particle interactions that are predominantly repulsive. Water-glycerol mixtures have the added advantage that the mixture can be prepared to have any desired viscosity in the range $\eta_{water} < \eta_{solvent} < \eta_{Glycerol}$. Since viscosity of the solvent in a suspension is a major contributor to the energy dissipated by the system, by varying the solvent viscosity, I can vary the energy dissipation in the system. I disperse the CS particles in the desired solvent (water or a water-glycerol mixture) at room temperature (25 ^{o}C).

The suspensions prepared using water-glycerol mixture are sonicated for 20 to 30 minutes after hand mixing to ensure homogeneity. Cornstarch particles undergo swelling when dispersed in water and water-glycerol mixtures ([11] and the references within). I ensured that the time between sample preparation to loading of the samples for measurements into the rheometer is kept same for all independent runs to minimize artifacts.

- **Polystyrene particles in Polyethylene glycol**: Suspensions are formed by dispersing PS particles (synthesized in our lab) in polyethylene glycol (PEG-400) [12] at different volume fractions ϕ ranging from 0.4 - 0.6. Details of the particle synthesis are given in section 2.2.4. Just before loading the sample for rheology measurements, the suspensions are ultrasonicated for 5 minutes to ensure uniform dispersion. [6]

Bibliography

[1] M. Ezzahmouly, A. Elmoutaouakkil, M. Ed-Dhahraouy, H. Khallok, and Z. Hatim. Micro-computed tomographic and SEM study of porous bioceramics using an adaptive method based on the mathematical morphological operations. *Heliyon*, 5(12):e02557, December 2019.

[2] *Basic Confocal Microscopy*. Springer International Publishing, Cham, Switzerland.

[3] Dong Wang, Bing Yu, Hai-Lin Cong, Yue-Zhong Wang, Qian Wu, and Ji-Lei Wang. Synthesis of Monodisperse Polystyrene Microspheres by Seeding Polymerization. *Integr. Ferroelectr.*, 147(1):41–46, January 2013.

[4] Anthony James Paine, Wayne Luymes, and James McNulty. Dispersion polymerization of styrene in polar solvents. 6. Influence of reaction parameters on particle size and molecular weight in poly(N-vinylpyrrolidone)-stabilized reactions. *Macromolecules*, 23(12):3104–3109, June 1990.

[5] Young-Sang Cho, Cheol Hwan Shin, and Sujin Han. Dispersion Polymerization of Polystyrene Particles Using Alcohol as Reaction Medium. *Nanoscale Res. Lett.*, 11(1):1–9, December 2016.

[6] Subhransu Dhar, Sebanti Chattopadhyay, and Sayantan Majumdar. Signature of jamming under steady shear in dense particulate suspensions. *J. Phys.: Condens. Matter*, 32(12):124002, December 2019.

[7] Nicole M. James, Endao Han, Ricardo Arturo Lopez de la Cruz, Justin Jureller, and Heinrich M. Jaeger. Interparticle hydrogen bonding can elicit shear jamming in dense suspensions. *Nat. Mater.*, 17(11):965–970, November 2018.

[8] Scott R. Waitukaitis. *Impact-Activated Solidification of Cornstarch and Water Suspensions*. January 2015.

[9] J. A. Richards, B. M. Guy, E. Blanco, M. Hermes, G. Poy, and W. C. K. Poon. The role of friction in the yielding of adhesive non-Brownian suspensions. *J. Rheol.*, 64(2):405, Mar 2020.

[10] Sebanti Chattopadhyay, Sharadhi Nagaraja, and Sayantan Majumdar. Effect of adhesive interaction on strain stiffening and dissipation in granular gels undergoing yielding. *Commun. Phys.*, 5(126):1–10, May 2022.

[11] Ivo R. Peters, Sayantan Majumdar, and Heinrich M. Jaeger. Direct observation of dynamic shear jamming in dense suspensions. *Nature*, 532:214–217, April 2016.

[12] Jianbin Qin, Guangcheng Zhang, and Xuetao Shi. Study of a shear thickening fluid: the suspensions of monodisperse polystyrene microspheres in polyethylene glycol. *J. Dispersion Sci. Technol.*, 38(7):935–942, July 2017.

CHAPTER

THREE

Yielding and dissipation in adhesive dense granular suspensions

The results covered in this chapter are published in the article Chattopadhyay et al., Communications Physics 5, 126 (2022) [1].

3.1 Introduction

In recent years there have been extensive studies, both experimental and theoretical, to understand failures in amorphous materials [2, 3, 4, 5, 6, 7, 8, 9, 10, 11, 12, 13, 14, 15, 16, 17, 18, 19, 20, 21, 22, 23]. Many of these studies are motivated by the generalized jamming phase diagram describing yielding in a variety of disordered materials based on only a few control parameters [24]. Dense particulate suspensions have been widely used as model systems for studying the yielding behavior. Depending on the inter-particle interactions, these systems show striking non-linear flow properties like, yielding, shear-thinning, shear-thickening, shear induced jamming [25, 26, 27, 28, 29, 30].

Although, yielding and failure in glassy and gel-like materials formed by Brownian particles have been widely studied, experiments probing the same in non-Brownian granular suspensions of rigid particles are very few [31, 32, 33]. Besides being inherently out of equilibrium, the main complexity arises from the fact that due to the large size of the constituent particles, flow of granular materials are dominated by contact interactions, since the stress scale for contact formation (critical onset stress) between two repulsive particles, $\sigma* \propto 1/d^2$ (d: particle diameter) [34] (see Chapter-6 for more details on this). Moreover, close to jamming, the average surface to surface separation between two particles becomes negligible compared to the particle size. As a result, van der Waals and other short-ranged attractive/adhesive interactions become very important for granular systems [35]. All these contributions make the flow behavior of these systems extremely complicated.

To cut through the complexity arising due to the frictional and adhesive/attractive interactions between non-Brownian particles, recently proposed constraint rheology models have been quite successful [36, 37, 38, 39]. In these models, all the interactions are encoded in the jamming packing fraction for the system, which gradually decreases from the value obtained in the limit of hard-core steric repulsion as the sliding and rolling degrees of freedom for the particles become more and more constrained due to enhanced inter-particle interactions. Measuring the jamming packing fractions from numerical simulations and using a generalized version of Wyart-Cates model [40], the framework of constraint rheology successfully captures many experimental aspects of yielding in granular systems. The complex interplay between inter-particle adhesion and friction demonstrated in recent

experimental studies [37, 38] emphasizes the difference in yielding mechanism in adhesive granular and Brownian systems, despite some superficial similarities in rheological response. Such difference mainly originates from the inter-particle friction that plays a far more important role in case of granular systems as compared to their Brownian counterparts. It is also evident from these studies that the existing framework of Brownian systems is not sufficient to describe yielding in adhesive non-Brownian systems and a fresh perspective is required.

In adhesive systems, stress induced viscoelastic deformation of fractal clusters can also play a key role in determining the mechanical properties. Such deformations can reflect as quasi-reversible strain stiffening response in bulk rheological measurements as has also been observed in colloidal gels [41, 42, 43]. Importantly, in granular systems, deformations of fractal particle clusters involve both adhesive and frictional contacts between the particles. Since, the number of these contacts depends on both applied perturbation and particle volume fraction, the strain stiffening response should also depend on these parameters. However, a detailed study of strain stiffening and its correlation with inter-particle interactions in the context of yielding in adhesive granular systems is currently lacking. The origin of such non-linearities also remains beyond the existing theoretical models for these systems. Such understanding is particularly crucial in the light of the difference in microscopic mechanism of yielding in colloidal and granular systems as mentioned above. All these points further signify that the nature of strain stiffening in granular systems can be quite distinct and the existing studies on colloidal systems are not sufficient to capture the detailed strain stiffening phenomena in adhesive granular systems. Furthermore, both thermal and athermal systems of attractive/adhesive particles show significant strain-localization which gets enhanced with increasing strength of interaction, as shown by recent experimental and simulation studies [44, 45, 46, 47, 48, 49, 50, 51]. However, any possible connection between strain-stiffening and spatio-temporal variation of velocity gradients in the system has not been highlighted in these studies. Thus, a complete picture of the yielding behavior requires the bulk non-linearity and energy dissipation to be connected to the local strain distribution, particle-scale interactions and irreversibility in these systems.

In this chapter, I study non-linear mechanics, energy dissipation, and plasticity in soft solids formed by dense suspensions of Cornstarch particles in Paraffin oil over a wide range of particle volume fractions and applied strain amplitudes. I show that the normalized energy dissipation and intra-cycle strain stiffening show a remarkable non-monotonic variation that depends on both strain amplitude and particle volume fractions. To our

knowledge, such complex behavior has never been reported in the context of yielding in granular or, colloidal gels. To gain a microscopic insight I experimentally determine, for the first time, critical jamming packing fractions for the adhesive granular system. These critical parameters encode complex, many-body inter-particle interactions in the system and also automatically take into account the amorphous shape of the particles. I further show that these critical parameters can explain the complete flow behavior of the system, as described in the detailed phase diagram.

3.2 Materials and methods

For our measurements, dense suspensions are prepared by dispersing Cornstarch (CS) particles in Paraffin oil (PO) at different volume fractions ϕ ranging from 0.15 to 0.44. Details of the CS particles and sample preparation techniques are given in section 2.3.1. The Young's modulus of CS particles is $\approx$ 5 GPa ([52] and references within), so for the maximum stress scales probed in our experiments ($\approx$ 150 Pa, refer to Appendix of this chapter), the strain deformation produced in the particle: $\sim \frac{150Pa}{5GPa} \sim 10^{-8}$ which is negligibly small. Thus, the particles can be considered to be rigid.

For density matched adhesive suspensions, I disperse CS particles in a hydrophobic organic liquid (Cargille labs). I vary the inter-particle adhesion in the CS-PO suspensions by adding a non-ionic surfactant Span® 60 (Sigma Aldrich) in varying quantities. For well dispersed suspensions with repulsive inter-particle interactions, I disperse CS particles in either water or in a water-glycerol mixture having viscosity matched with Paraffin oil at room temperature (25 ^{o}C). In section 2.3, I give the detailed sample preparation techniques for all these cases and also explain the different inter-particle interactions present in these systems. Details of the Confocal imaging of CS particles dispersed in Paraffin oil can be found in section 2.2.3.

Rheological measurements are performed using a stress controlled rheometer (MCR-702 Anton Paar, Austria). I use sandblasted cone-plate geometry with diameter of 50 mm and cone angle of 2°. The in-situ imaging is done using a Lumenera Lt545R camera fitted with a 5X Mitutoyo objective. For image analysis, the images are taken at discrete values of strain amplitude γ_0 with frame rate varying between 1 Hz - 40 Hz. Refer to section 2.2.1 and [1] for additional details of the experimental setup and geometry used.

I use Large amplitude oscillatory shear (LAOS) protocol for all our rheological measurements in the separate motor transducer (SMT) mode (see section 2.2.1). LAOS measurements are done at an angular frequency (ω) of 0.1 rad/s. The rheometer mea-

sures the intra-cycle stress and strain to measure the G' and G'' values (first harmonics) for each data point of the measurement over a strain amplitude range of 0.001 to 2 (I have also checked over a range 0.0001 to 2 which I show in Fig. 3.2 in the next section). I acquire 15 data points per decade of strain variation for the strain range of 0.001 to 2 and 12 points per decade for the strain range of 0.0001 to 2. LAOS measurements also provide higher harmonic values of the moduli. For the rheological measurements on repulsive systems (using water-glycerol mixture as solvent, see section 2.3.2), an in-house built humidity chamber is used to prevent solvent evaporation. For LAOS measurements, after loading the sample in the cone-plate geometry, I wait for the normal force response from the loaded sample to reach zero before starting the measurements. I observe that for $\phi \leq 0.3$, the normal force almost immediately goes to zero, but for higher ϕ values, I have to wait for a few minutes before the normal force vanishes. I find that this protocol provides a fairly good reproducibility, as seen from the multiple independent experimental runs (Fig. 3.18(a) and 3.18(b)). Although I did not apply any pre-shear to our samples, I verified that applying a pre-shear before the measurements does not significantly alter the results (Fig. 3.18(c)).

Finally, for particle settling experiments, I degas the sample (CS dispersed in Paraffin oil) and transfer them to 15 mL graduated Falcon tubes very gently. Next, the tubes are either kept in a vertical position and left undisturbed for 3 weeks (for settling under gravity) or, centrifuged (Remi, R-8C BL) in a swinging-bucket type holder with rotation speed varying between 1000 - 2500 rpm for 2 hours. For this range of rotation speeds and considering slight sample to sample variation in bed heights, I find that the average acceleration approximately varies between $114g$ - $711g$ (g: acceleration due to gravity). I confirm that in all cases the waiting time is sufficient to get a stable bed formation.

3.3 Results and discussion

For rheological measurements, I perform oscillatory amplitude sweep at a constant frequency (see Materials and methods). I show the variation of Elastic (G') and Viscous (G'') moduli as a function of strain amplitude (γ_0) for $\phi = 0.4$ in Fig. 3.1(a). The system remains predominantly elastic ($G' > G''$) till intermediate γ_0. However, for larger strain amplitudes, a crossover to fluidization is observed with $G'' > G'$. Interestingly, I do not find any linear visco-elastic region (where G' and G'' become independent of γ_0) even for γ_0 values as low as 0.0001 (see Fig. 3.2(a)). This implies that some rearrangements are always present in the system. In fact, I also find an absence of linear response regime

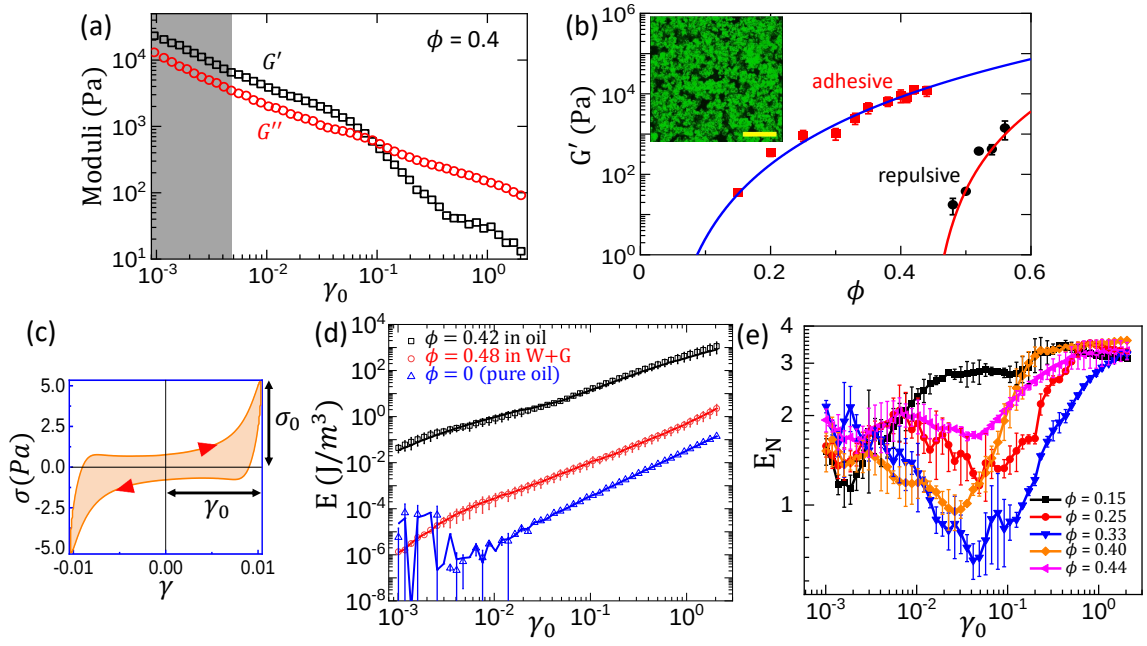

Figure 3.1: (a) Elastic (G') and viscous (G'') moduli as a function of applied strain amplitude γ_0 for Cornstarch particles (CS) dispersed in Paraffin oil for a volume fraction (ϕ) = 0.4. (b) G' vs. ϕ for CS in water (black circles) and CS in Paraffin oil (red squares). The error bars represent the standard deviation of G' values over the range of γ_0 indicated by the shaded region in panel (a). The solid lines are fits to the empirical relation $G' = G_\phi(\phi - \phi_J)^\alpha$ with $\alpha = 5.1$, $\phi_J = 0.02$ for CS in Paraffin oil and $\alpha = 4.6$, $\phi_J = 0.44$ for CS in water. Inset shows maximum intensity projection of typical Confocal z-stack images for CS in Paraffin oil system inside a gravitationally settled bed. Scale bar: 150 μm. (c) A typical elastic Lissajous plot (orange curve) showing intra-cycle strain stiffening. The peak stress σ_0 and strain amplitude γ_0 for the Lissajous plot are also indicated. Blue bounding box denotes the Lissajous plot for an ideal plastic material for the same σ_0 and γ_0. (d) Variation of dissipated energy density (E) as a function of γ_0 for CS in Paraffin oil ($\phi = 0.42$), CS in water-glycerol mixture ($\phi = 0.48$) and pure solvent (Paraffin oil) as indicated by different symbols. The solid lines indicate $E = \pi \gamma_0^2 G''$ and the error bars are the standard deviation from two independent measurements. (e) Normalized energy dissipation (E_N) as a function of γ_0 for different ϕ values indicated in the figure. Data points represent the mean values and error bars represent the standard deviations of at least three independent experimental runs (except for $\phi = 0.15$, where only two runs are considered).

for suspensions of CS particles dispersed in a density matched hydrophobic organic liquid (see Materials and methods, section 2.3.1 and Fig. 3.2 (b)). This indicates that such behavior is not caused by density mismatch. This non-linear response is further confirmed by significant contribution of the higher harmonics of G' (Fig. 3.3). Interestingly, in some cases, I observe noticeable even harmonic values, as also reported for highly non-linear polymeric systems [53]. However, I find that for repeated experimental runs, the average even harmonic contributions remain negligible compared to the odd harmonics (Fig. 3.3).

To study the effect of inter-particle interactions in controlling the mechanical properties of the system under small perturbations, I plot G' values averaged over strain amplitude range $0.001 < \gamma_0 < 0.005$ (shown by the shaded region in Fig. 3.1(a)) for different ϕ values in case of both adhesive (CS in Paraffin oil) and repulsive (CS in water) suspensions in Fig. 3.1(b). I find that the adhesive interactions give rise to significant elasticity at ϕ values much lower compared to that required for the repulsive suspension to have a similar elasticity, as has been observed in numerical simulations [47] and other experimental studies [54] as well. For adhesive inter-particle interactions, contact networks comprising of fractal aggregates (see Fig. 3.4 and refer to the Appendix of this chapter) impart stability to the system for average coordination numbers well below the Maxwell isostaticity criterion [55]. Using Confocal imaging (section 2.2.3) I indeed observe such a system spanning porous structure inside a stable bed settled under gravity (Inset of Fig. 3.1(b)) (See the movies at https://drive.google.com/drive/folders/1tBpH4at94DK27DMF_6LuBWfIxBLZtD1a?usp=sharing and refer to Appendix for movie description). These porous structures are stabilized by the adhesive interactions to support their own weight which also explains the origin of bulk elasticity in the system for volume fractions far below the random close packing limit (≈ 0.56) obtained in the presence of steric repulsion alone [56]. As expected, I see that such porous structures are not stable under gravity in presence of steric-repulsive inter-particle interactions alone (Refer to the movies at https://drive.google.com/drive/folders/1tBpH4at94DK27DMF_6LuBWfIxBLZtD1a?usp=sharing and to Appendix for movie description). I observe that the variation of G' as a function of ϕ is compatible with a proposed empirical law [54]: $G' = G_\phi(\phi - \phi_J)^\alpha$ for both adhesive and repulsive suspensions (Fig. 3.1(b)). However, I find that the exponent α and the parameter ϕ_J are different for these two suspensions. This is not surprising, since, these parameters depend on detailed inter-particle interactions, as also observed earlier [54].

For different ϕ values, I also record intra-cycle stress (σ) vs strain (γ) for each data point of G', G'' vs γ_0 to obtain Lissajous plots. One such plot is depicted in Fig. 3.1(c)

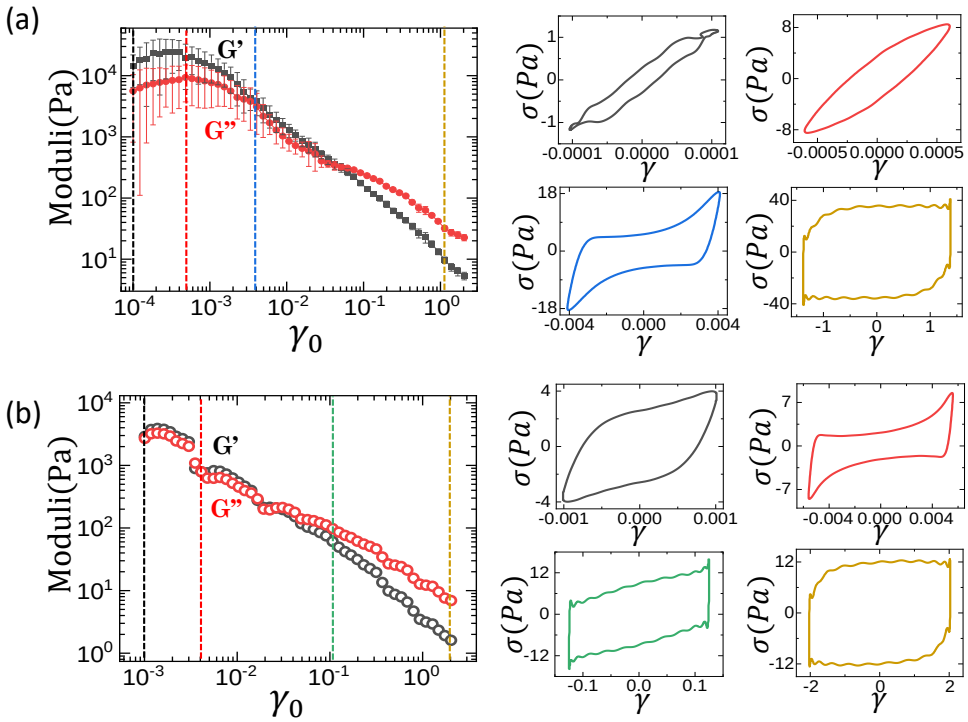

Figure 3.2: (a) Elastic G' and viscous moduli G'' vs strain amplitude γ_0 for Cornstarch (CS) particles dispersed in Paraffin oil averaged over three independent measurements (to see the trend clearly at small values of γ_0) over γ_0 range of 0.0001 to 2. The error bars are the standard deviations. Absence of a linear region for γ_0 values as low as one order below the range shown in Fig. 3.1 implies that some rearrangements are always happening in the system, even at very low strains. Right panel shows the typical Lissajous plots (obtained from one of the three experimental runs) at four well spaced γ_0 values indicated by dotted lines. (b) Typical variation of Elastic (G') and Viscous(G'') moduli as a function of γ_0 for CS particles dispersed in density matched organic liquid (see Materials and methods and section 2.3.1). Right panel shows elastic Lissajous plots at four well spaced γ_0 values indicated by the dotted lines in G', G'' vs γ_0 plot. I see similar non-linear features (strain stiffening and absence of linear region for small strain amplitudes) for this system as I see for CS in Paraffin oil (Fig. 3.1 and Fig. 3.6). This indicates that absence of linear region for very small γ_0 values is a general feature of such adhesive systems. I would like to also point out that at large strain values, Lissajous plots look similar in both cases. This is due to the fact that in the fluidized state, the response is dominated by the instrument's inertia rather than from the system itself. In both cases, volume fraction ϕ=0.4.

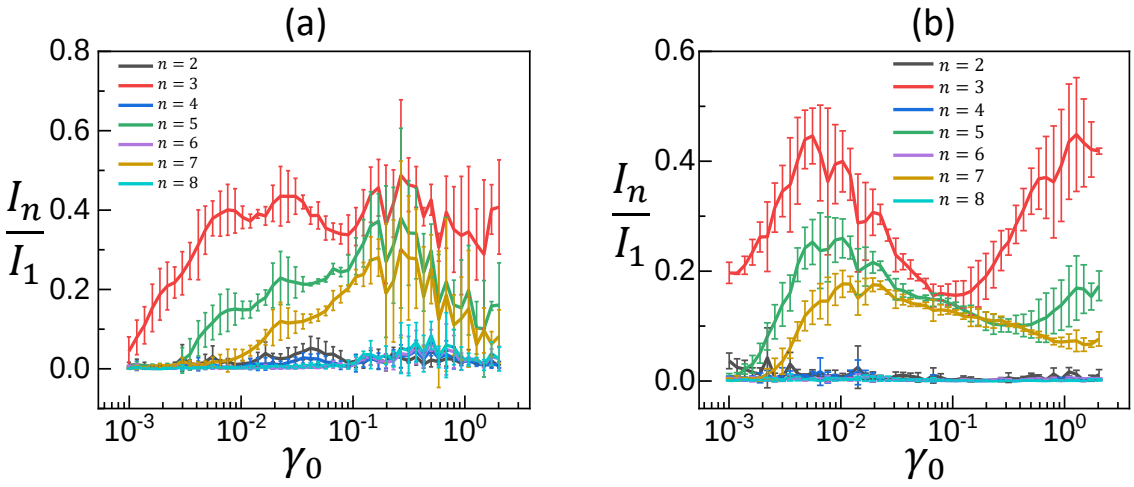

Figure 3.3: (a) Relative contribution of the higher harmonics of elastic modulus (G') with respect to the fundamental (I_n/I_1) as a function of strain amplitude γ_0 averaged over 3 independent measurements for Cornstarch (CS) particles dispersed in Paraffin oil (panel (a)) and in density matched organic liquid(panel (b)) . In both cases, $I_n/I_1 = |G'_n/G'|$ and volume fraction $\phi = 0.4$.

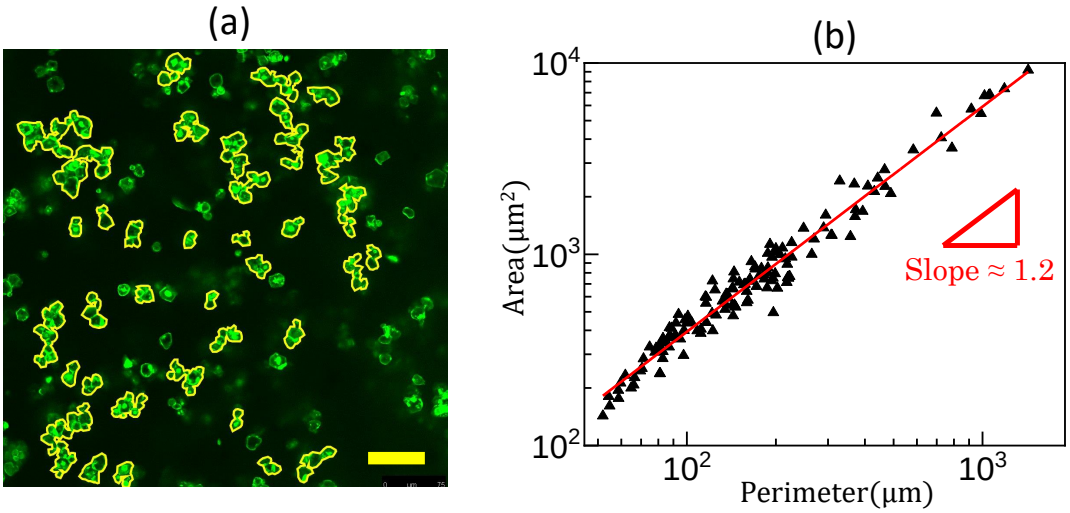

Figure 3.4: (a) A typical Confocal slice of the settled bed of Cornstarch (CS) particles in Paraffin oil. The boundaries of the 2-D projected particle-clusters (having different sizes) are marked in yellow. Scalebar: 75 μm. (b) Variation of the projected area (A) of CS particle clusters obtained from many of such Confocal slices as a function of perimeter (P). By plotting the A vs P in log-log scale (refer to the Appendix of this chapter), I obtain the 2D fractal dimension $d_f \approx 1.2$ from the slope as shown in the figure.

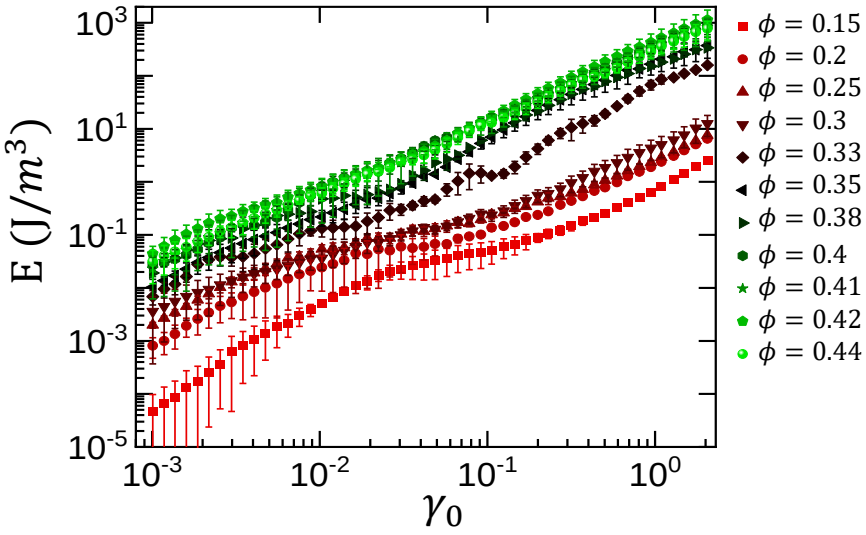

Figure 3.5: Variation of dissipated energy density (E) as a function of strain amplitude γ_0 for Cornstarch (CS) particles dispersed in Paraffin oil for volume fraction ϕ ranging from 0.15 to 0.44.

showing a clear signature of non-linear strain stiffening, when the differential shear modulus $K = \frac{d\sigma}{d\gamma}$ increases with increasing strain. The area enclosed by the Lissajous plot gives the intra-cycle energy dissipation per unit volume (dissipated energy density): $E = \oint \sigma(\gamma)\, d\gamma$. I compare the variation of E as a function of γ_0 for both adhesive (CS in Paraffin oil) and repulsive suspensions (CS in water-glycerol mixture) in Fig. 3.1(d). I observe that E increases monotonically with increasing γ_0 as well as ϕ values (see Fig. 3.5). Importantly, I see that the dissipated energy for the adhesive system remains several orders of magnitude higher than that for the repulsive system over the entire strain range. CS particles are hydrophilic, so when dispersed in Paraffin oil, they form an adhesive suspension (see section 2.3.1). I should note that in both repulsive (CS in water, see section 2.3.2) and attractive/adhesive (CS in Paraffin oil) suspensions, steric repulsion is present but additionally in case of attractive/adhesive suspensions, the particles stick together on contact and there is an energy cost to break such contacts. This explains the hugely enhanced dissipation in the attractive/adhesive system compared to the repulsive one. In all cases, I find that the analytical expression $E = \pi G'' \gamma_0^2$ captures the variation of the dissipated energy accurately (Fig. 3.1(d)). However, I have fitted the corresponding G'' for each γ_0. Since for our system, G'' is not a constant but decreases with γ_0 roughly as a power law over the entire range of strain amplitudes (Fig. 3.1(a)), the point by point fitting is actually using a dependence of $E \sim \gamma_0^{\alpha}$ with the exponent $\alpha < 2$, unlike the case of pure viscous or linear visco-elastic materials [57] where $\alpha = 2$.

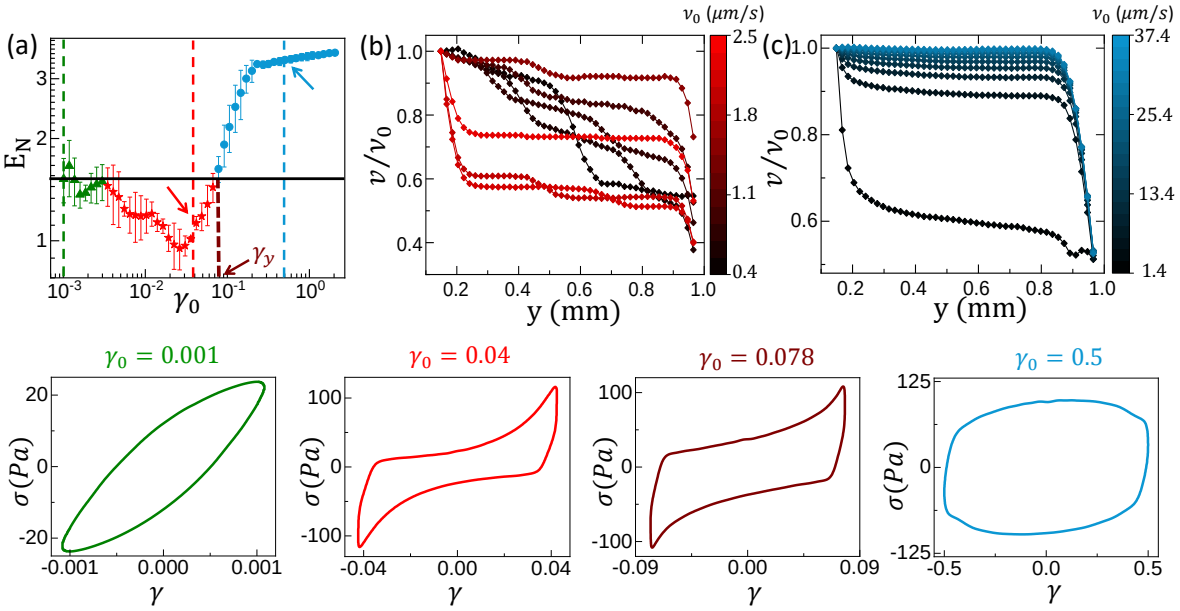

Figure 3.6: (a): Normalized energy dissipation E_N vs strain amplitude γ_0 for volume fraction $\phi = 0.4$. The horizontal black line indicates $E_N = E_N^0$, the average small strain value of E_N. The points for which $E_N < E_N^0$ and $E_N > E_N^0$ are marked with red stars and blue circles, respectively. The arrows indicate the γ_0 values for which the velocity profiles are shown in (b) and (c). The yield strain value (γ_y) is also indicated in the figure. Velocity profiles across the gap between the edge of the top cone and the bottom plate normalized by the instantaneous maximum velocity (v_0) of the moving bottom plate for $\gamma_0 = 0.04$ (panel (b)) and $\gamma_0 = 0.5$ (panel (c)). The color gradients indicate the instantaneous maximum velocity in the sample (approximately equal to the bottom plate velocity at that instant) during one quarter of an oscillatory applied strain cycle. The bottom row indicates typical Lissajous plots corresponding to different regions of the E_N vs γ_0 curve (marked by vertical dashed lines) shown in panel (a). The corresponding γ_0 values are also indicated. The error bars in panel (a) indicate the standard deviations from three independent measurements.

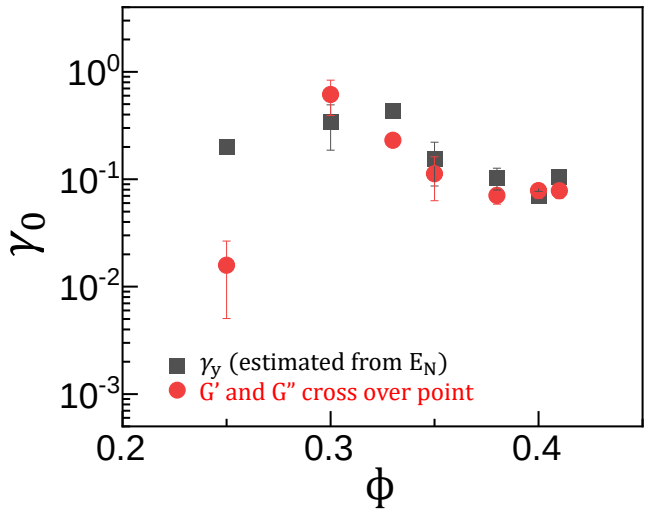

Figure 3.7: Variation of the yield strain γ_y (defined using the normalized energy dissipation E_N, as mentioned in the Results and discussion) and the cross-over strain amplitude of elastic (G') and viscous(G'') moduli over that range of volume fraction ϕ where E_N shows a non-monotonic variation with strain amplitude γ_0. Error bars indicate standard deviations over three independent measurements. I get very similar trends (except for $\phi = 0.25$), in both the cases. This observation rationalizes our definition of yield strain in terms of the normalized energy dissipation in the system.

I find that dissipated energy E, which has a monotonic dependence on both γ_0 and ϕ, does not provide much information about the non-linearity in the system, as indicated by the similar nature of the curves in Fig. 3.5. Thus, to capture the non-linearity and dissipation in the system over a wide range of parameters, I define normalized energy dissipation ([58] and references therein), $E_N = \frac{E}{\sigma_0 \gamma_0}$, where σ_0 is the peak stress corresponding to an applied strain amplitude γ_0. Physically, the quantity $4\sigma_0\gamma_0$ denotes the dissipation for an ideal plastic material as indicated by the blue bounding box in Fig. 3.1(c). I show the variation of E_N as a function of γ_0 over a range of ϕ values (Fig. 3.1(e)). Interestingly, I find a non-monotonic variation of E_N as a function of both γ_0 as well as ϕ. The decrease in E_N with increasing γ_0 arises due to the strain stiffening behavior shown by the system (Fig. 3.1(c)). Similar strain stiffening and plasticity is also observed for the density matched system (Fig. 3.2 (b)) mentioned earlier. These observations demonstrate that our experimental results for adhesive granular suspensions are independent of gravity induced effects.

I now take a closer look at the non-monotonicity of E_N to understand the yielding behavior of the system. Fig. 3.6(a) shows the typical variation of E_N as a function of

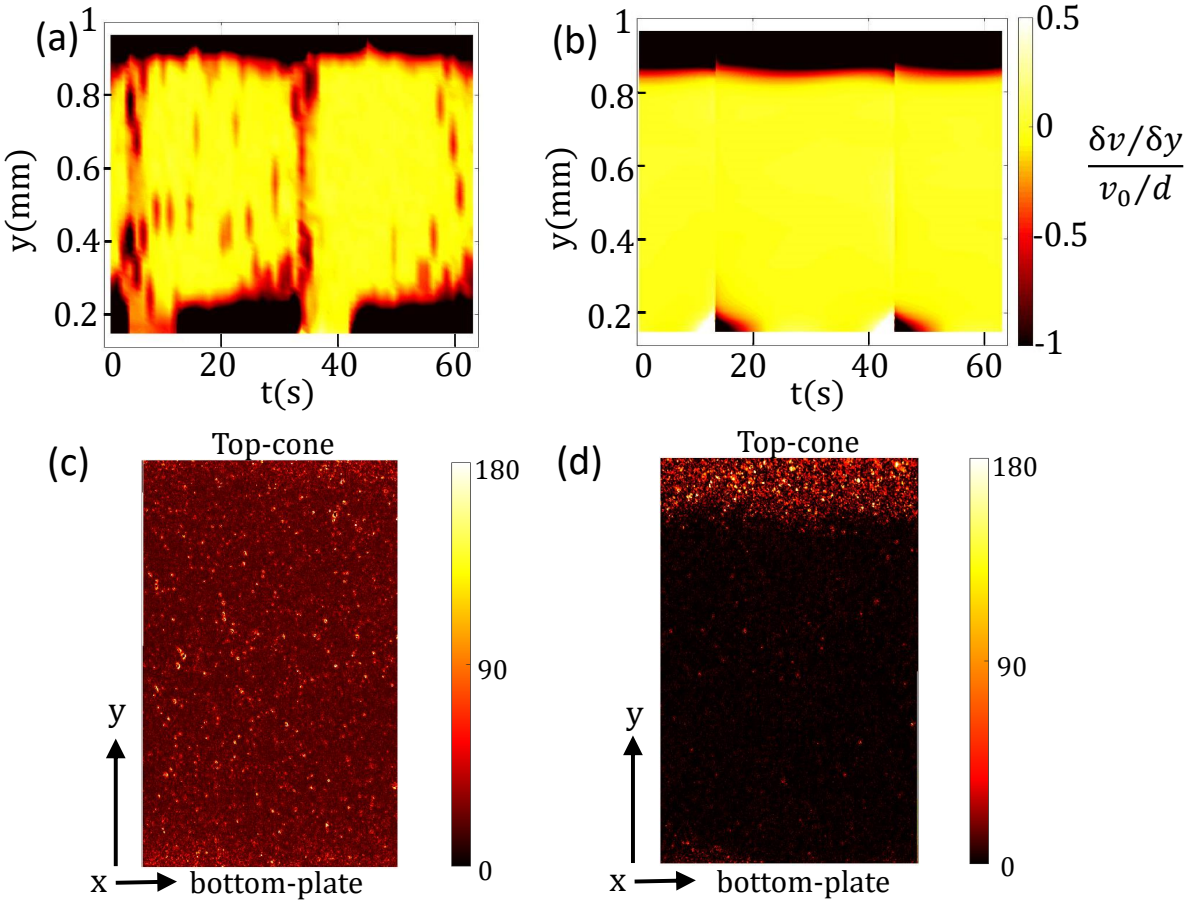

Figure 3.8: (a) and (b) show the space-time plot (in y-t plane) of dimensionless velocity gradient (indicated by the colourbar) across the shear gap in the system (volume fraction $\phi = 0.4$) over a complete cycle of oscillation for strain amplitude $\gamma_0 = 0.04$ and $\gamma_0 = 0.5$, respectively. Here, time t varies from 0 to T (time period of the applied oscillatory strain). For our measurements, $T \approx 63$s. The system undergoes two strain reversals at ≈ 16s and ≈ 47s, respectively. (c) and (d) indicates the stroboscopic difference between images captured at $\gamma(t)$ and $\gamma(t+T)$ for $\gamma_0 = 0.04$ and $\gamma_0 = 0.5$, respectively. These results are obtained from the boundary imaging that probes a thin sample layer near the suspension-air interface.

γ_0 for the CS - Paraffin oil system ($\phi = 0.4$). For small γ_0 , the average value E_N is denoted by E_N^0. With increasing γ_0, the value of E_N first decreases from E_N^0 and reaches a minimum. At intermediate values of γ_0, E_N increases and becomes larger than E_N^0, finally saturating beyond $\gamma_0 \geq 0.2$ for the higher γ_0 values (Fig. 3.6(a)). In the region where $E_N \leq E_N^0$, the system displays a strain stiffening response which disappears in the region with $E_N > E_N^0$, where the mechanical response shows strain-weakening/plasticity as indicated by the Lissajous plots in Fig. 3.6. For soft visco-elastic solids under an oscillatory shear, the yield strain is defined by the critical strain amplitude beyond which the elastic modulus G' starts to drop from its constant (linear response) value [59]. This yield point is usually close to the crossover point of G' and G'' (flow point). Since in our system I do not find a linear response regime even for strain values far below the flow point as seen in Fig. 3.1(a) (also, Fig. 3.2 (a)), the yield strain in our case cannot be defined by the conventional manner. Also, as our system is highly non-linear, the fundamental harmonics (G' and G'') alone are not sufficient to capture the flow behavior accurately. Hence, I define the yield strain as the strain amplitude (γ_y) beyond which the normalized dissipation E_N exceeds E_N^0 as indicated by the solid line in Fig. 3.6(a). I find that γ_y comes fairly close to the flow point (Fig. 3.7). Beyond γ_y, the dissipation in the system shows a significant increase as shown by the Lissajous plots in Fig. 3.6. Similar enhancement of dissipation beyond the yielding transition has also been observed earlier [8].

Next, I look at the flow behavior of the system by mapping out the velocity profiles across the shear gap using boundary imaging during the applied oscillatory deformations. The schematic of rheology and in-situ optical imaging set-up of the sample boundary is shown in Fig. 2.1 in Chapter-2. Due to the opaque nature of particles, I can image only a thin layer of sample near the suspension-air interface. Since I apply an oscillatory strain, instantaneous velocity of the moving bottom plate v_0 continuously increases from 0 to v_{max} over one quarter of a sinusoidal cycle of strain deformation (measured from a turning point). Here, v_{max} is the maximum plate velocity for a given strain amplitude γ_0: $v_{max} = \omega\gamma_0 d$ (d: shear gap, ω: angular frequency). I show the velocity profiles across the shear gap obtained from a single measurement for few discrete values of v_0 varying between 0 to v_{max} for two different γ_0 values in Fig. 3.6(b) ($\gamma_0 = 0.04$) and 3.6(c) ($\gamma_0 = 0.5$), corresponding to the two phases identified in Fig. 3.6(a). Here, the plane of imaging is x-y with the flow direction along 'x' and velocity gradient along 'y' (see Fig. 2.1). Different v_0 values are colour-coded as indicated by the colorbars in the figure. Also, as the variation of v_0 is significant (0 to v_{max}) it is difficult to show the absolute velocity

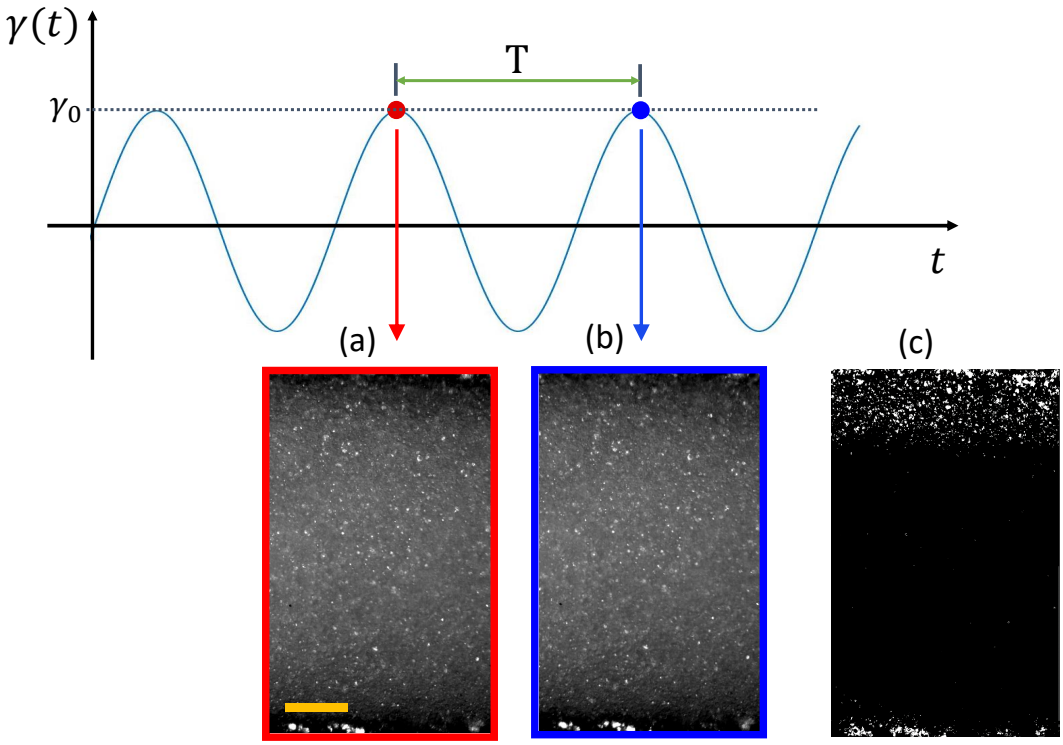

Figure 3.9: Top panel shows a typical sinusoidal strain input from the LAOS (Large Amplitude Oscillatory Shear) measurements. Points indicated in red and blue are at the same part of the cycles (here chosen at the turning points) but, separated by one time period (T) as indicated. The panels (a) and (b) show the images taken at the indicated points (image frame colours correspond to the points on the sinusoidal curve). Image (c) represents the stroboscopic image which is obtained by taking a difference between the images shown in (a) and (b). Scale bar represents 150 μm.

profiles in the same plot for all v_0 values. Thus, in Figs. 3.6(b) and 3.6(c) the profiles are normalized using the corresponding v_0 values. In both the cases I observe strong shear-banding as also reported for other adhesive/attractive systems [44, 46, 47]. Interestingly, I also observe that for $\gamma_0 = 0.04$, the velocity fluctuations are neither systematic in space nor in time (Fig. 3.6(b)), whereas, for $\gamma_0 = 0.5$ such fluctuations are absent and the velocity profiles become much more self similar, particularly, for the higher v_0 values (Fig. 3.6(c)).

I now focus on the spatio-temporal distribution of velocity gradients in the system over a complete cycle of strain deformation. I define a dimensionless gradient given by the ratio of the local velocity gradient and the average velocity gradient across the shear gap (assuming an affine deformation) measured at the same instant of time: $\frac{\delta v/\delta y}{v_0/d}$. In Fig. 3.8(a) and 3.8(b), I show space-time plots of the dimensionless velocity gradient over an entire cycle of strain deformation. I consider discrete velocity profiles across the shear-gap equally spaced in time over one full cycle of sinusoidal strain deformation for $\gamma_0 =$ 0.04 (Fig. 3.8(a)) and 0.5 (Fig. 3.8(b)), respectively. Here, the horizontal axis represents the time and the vertical axis represents the position along the direction of the velocity gradient (Fig. 2.1). The colour-coding represents the strength of the gradient. I observe that strong local gradients appear in spatio-temporally random locations for $\gamma_0 = 0.04$ (Fig. 3.8(a)), but, such gradient distribution remains smooth for $\gamma_0 = 0.5$ (Fig. 3.8(b)), except for the regions near the boundaries at the turning points. For our experiments, the time period of one cycle of oscillation T 63 seconds (corresponding to a frequency of 0.1 rad/s). Thus the two turning points (where strain reversals happen) occur at 16 seconds and 47 seconds, respectively. Remarkably, both below and above yielding, the velocity gradient over a significant portion of the sample (away from the shearing boundaries) remains negligible. This is also evident from the slope of the velocity profiles shown in Fig. 3.6(b) and 3.6(c). This indicates that across the fluidization/yielding transition, there are coexisting solid-like and fluid-like regions inside the sample. Even deep inside the fluidized phase at large γ_0 values, such coexistence remains, with the fluidized regions confined near the shearing boundaries. It is interesting to note that particularly for higher γ_0 values beyond yielding, the velocity gradient near the top cone is stronger than that near the bottom plate (Fig. 3.8(b)) as also observed for other ϕ values. Although, at high volume fractions ($\phi > 0.22$) the system forms a yield stress solid, there can still be a slight asymmetry in the strength of inter-particle contacts induced by the gravitational stress due to the density mismatch between CS and Paraffin oil. Owing to the slightly weaker contacts, the suspension near the top cone gets fluidized relatively easily under a

significant applied shear strain.

Next, I look at the irreversible particle reorganizations in the system by calculating stroboscopic image difference as obtained from the boundary imaging. Basically, for a given γ_0, I calculate the difference between two gray-scale images of the sample-air boundary across the shear gap captured at time t and $t + T$ (Fig. 3.9). If the strain deformation inside the sample layer is completely reversible, such difference image should show zero intensity (within the limits of noise such as dark noise, source intensity fluctuations, etc.) everywhere. On the other hand, finite intensity in specific locations indicates irreversible particle rearrangements (localized plastic deformations) in the system. I see from Fig. 3.8(c) and (d) that irreversible rearrangements take place uniformly throughout the sample below yielding, but such events get strongly localized near the shearing boundaries for larger strain values above yielding. This behavior is strongly correlated with the velocity gradient distribution in the system (Fig. 3.8(a) and (b)): the plastic rearrangements predominantly take place at spatial positions where the local velocity gradients are significant, as expected.

As mentioned earlier, inter-particle interactions in dense suspensions are extremely complex and many body in nature, with an interesting dependence on the applied stress. Recent studies [37, 39] show that jamming packing fractions (ϕ_J) can be used to quantify such inter-particle interactions. To directly measure the jamming packing fractions for our system, I use particle settling experiments (see Materials and methods). Although, to our knowledge, there are no reports of such experiments to understand inter-particle interactions in adhesive granular suspensions, settling under centrifugation has been used in earlier studies to obtain insights into the rheological behaviors in repulsive frictional systems showing shear thickening [60, 61]. The basic principle of such settling experiments involves an evolution of the system from an under-constrained initial state (a suspension with relatively lower volume fraction of particles), so that, under a given forcing condition (gravity/centrifugation) the particle pack can get more and more compact and be able to evolve towards the jamming packing fraction in the asymptotic/long-time limit. The jamming packing fraction for a given forcing condition is solely determined by the inter-particle interactions and is invariant for a given system. The details of the settling dynamics depends on the initial volume fraction of the under-constraint state and is not important in this work, as well as, the studies mentioned earlier [60, 61]. In our case, I denote the average volume fraction inside a stable settled bed for a particular forcing condition as ϕ_{bed} that indicates the corresponding jamming packing fraction. Essentially, ϕ_{bed} is the minimum particle volume fraction required to constrain the sliding/rolling motion

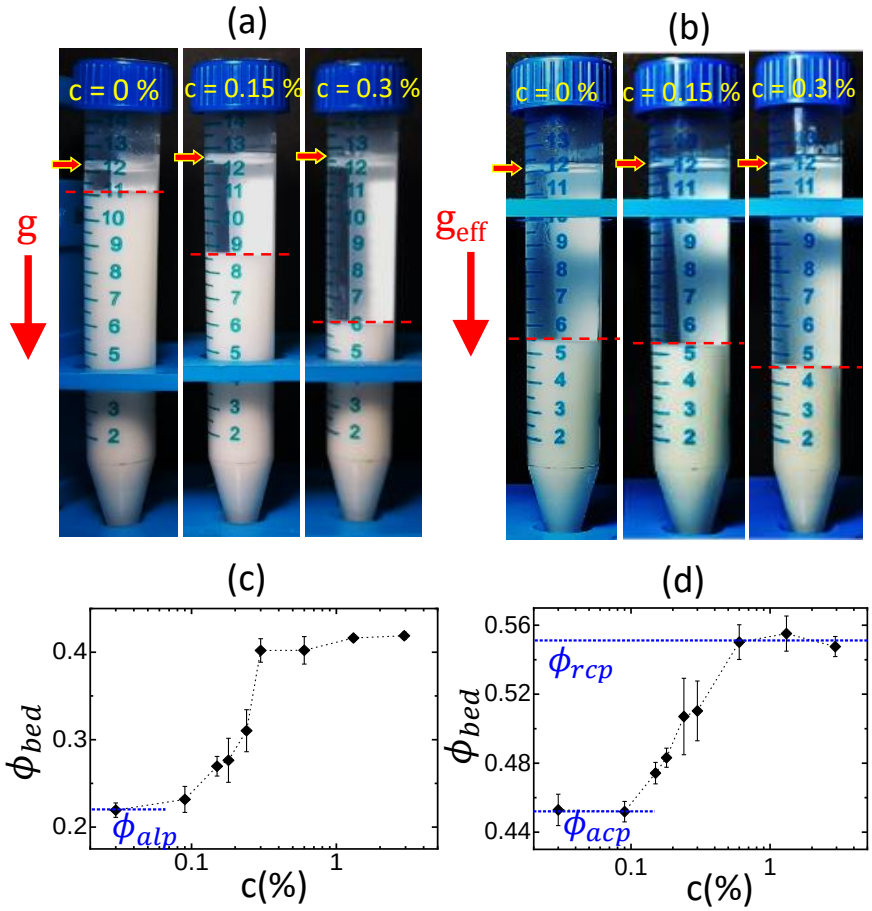

Figure 3.10: (a) Stable settled bed heights obtained under gravity for different surfactant concentrations (c) as indicated in the figure. (b) Same obtained under centrifugation at a rotation rate of 2000 rpm ($g_{eff} = 455g$, g: acceleration due to gravity). Variation of the packing fraction inside the settled bed (ϕ_{bed}) under gravity (panel (c)) and under centrifugation at 2000 rpm (panel (d)) with increasing surfactant concentrations. In all cases the initial volume fraction of the sample is 0.2. The value of ϕ_{bed} at zero surfactant concentration under gravitational settling gives ϕ_{alp} as shown in (c). ϕ_{bed} at zero surfactant concentration for centrifugal settling gives ϕ_{acp} and for high surfactant concentration at saturation gives ϕ_{rcp} as indicated in (d). In (c) and (d) the error bars are the standard deviation for four independent measurements.

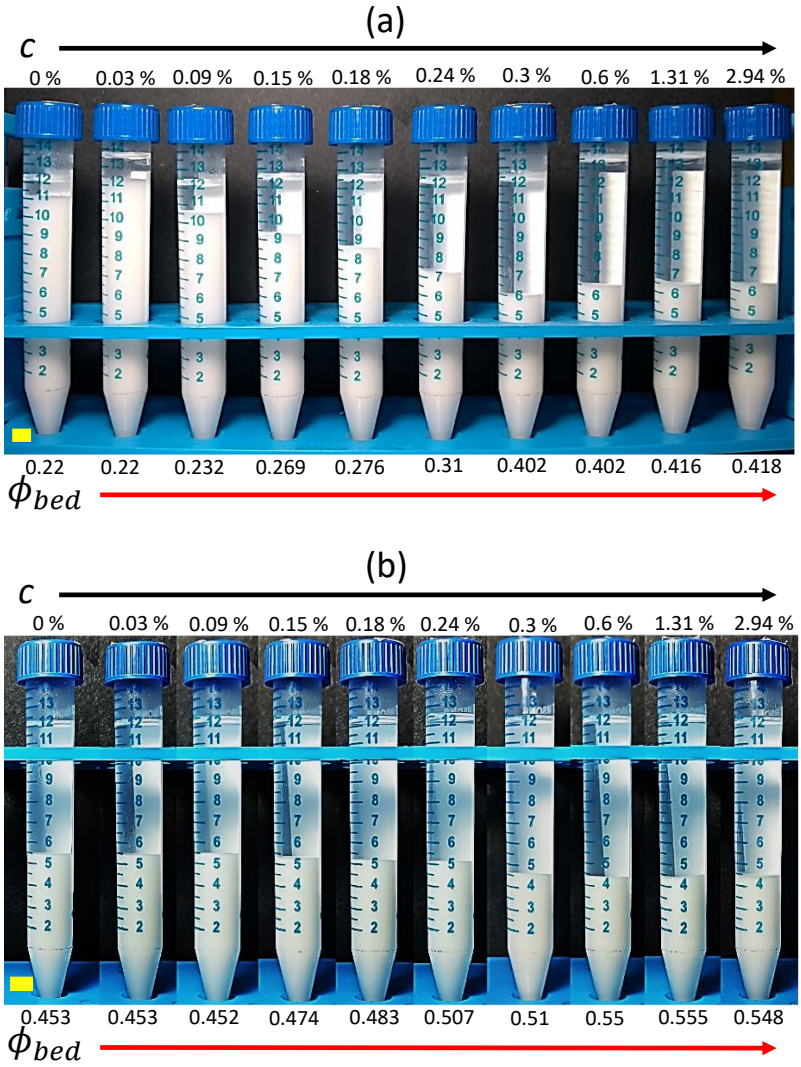

Figure 3.11: Images of the settled beds as function of surfactant concentration (c) for gravitational settling (panel (a)) and centrifugation at 2000 rpm (panel (b)). The packing fraction inside the beds (ϕ_{bed}) are also indicated. In all cases the initial volume fraction (ϕ) of the suspensions is 0.2. Scalebar $\approx$ 6.5 mm.

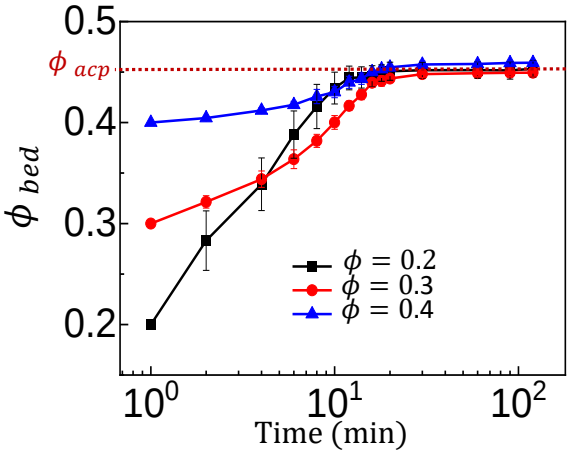

Figure 3.12: Variation of settled bed packing fraction ϕ_{bed} with time under centrifugation at 2000 rpm for different starting volume fractions ϕ as indicated.

of the particles against the stress acting on the bed. I show the typical images of stable settled beds formed under gravity (Fig. 3.10(a)) and centrifugation at 2000 rpm (Fig. 3.10(b)) for different inter-particle interactions tuned by addition of surfactant (also see Fig. 3.11). I observe from Fig. 3.10(a) that for just CS in Paraffin oil, $\phi_{bed} \approx 0.22$ that corresponds to the adhesive loose packing of the system (ϕ_{alp}). This value of ϕ_{alp} is far below the volume fraction for random close packing of CS particles having steric-repulsive interaction [56]. This indicates a highly porous particle arrangement inside the settled bed for the adhesive system. When I add the non-ionic surfactant (Span-60) to the system, the hydrophilic part of the surfactant molecules gets adsorbed onto the surface of the particle while the hydrophobic part easily extends into the Paraffin oil. With the addition of increasing amount of surfactant, the particle surface is expected to get gradually covered with enough surfactant molecules so that it becomes hydrophobic (refer to the Appendix of this chapter). This effectively reduces the solvent induced adhesive interaction between the particles and makes them disperse better (see schematics in Fig. 3.13) which leads to a disintegration of the fractal clusters resulting in a more efficient packing of the particles. As a result, the settled bed height decreases due to more compact particle organization. In Fig. 3.10(c) I show the variation of ϕ_{bed} as a function of surfactant concentration (c) for gravitational settling. With increasing c, ϕ_{bed} increases from ϕ_{alp} (for $c = 0$) and saturates beyond $c > 0.3$ %. Similar trend of ϕ_{bed} vs c is also observed under centrifugation (Fig. 3.10(d)), where the effective acceleration (g_{eff}) is much higher than the acceleration due to gravity (g) (see Materials and methods). I choose the value of g_{eff} such that the resulting inter-particle stress scale is much higher than that probed in the rheology measurements

(refer to Appendix of this chapter). Under this condition, ϕ_{bed} (for $c = 0$) gives the adhesive close packing (ϕ_{acp}) and the saturation at higher values of $c > 0.6\%$ gives the random close packing (ϕ_{rcp}) of the system in the limit of hard-sphere repulsion. I find $\phi_{acp} \approx 0.45$ and $\phi_{rcp} \approx 0.55$. This value of ϕ_{rcp} is close to that reported for CS particles with repulsive interactions [56]. I also confirm that the obtained values of ϕ_{acp} and ϕ_{rcp} are not sensitive to the starting volume fractions (see Fig. 3.12) and the different g_{eff} values that I use. Such invariance further indicates that jamming packing fractions are directly correlated to the inter-particle interactions in the system, as mentioned above. From Fig. 3.10(c) and (d), I find that the change in ϕ_{bed} as a function of surfactant concentration is much more abrupt under gravitational settling as compared to settling under centrifugation. A possible explanation can be that for the minimum amount of added surfactant, under gravitational settling the average coordination number of particles inside the settled bed (which depends on the jamming packing fraction, see for example, Ref. [39]) remains much lower compared to that for settling under centrifugation. Thus, beyond the critical surfactant concentration a sudden compaction is possible for gravitational settling due to lack of constraints for particle rearrangements (due to lower coordination number). However, owing to the higher coordination number, such sudden compaction is not possible for settling under centrifugation and compaction happens only gradually. However, understanding the detailed microscopic dynamics needs future studies.

Our ability to tune the inter-particle interactions enables us to investigate the role of adhesion on the observed non-linear strain stiffening and the energy dissipation in the system. In Fig. 3.13, I show the schematics depicting how the fractal clusters of the hydrophilic particles disintegrate and finally disperse in the hydrophobic solvent with increasing surfactant concentration. From rheological measurements, I find that increasing the amount of surfactant causes a dramatic reduction of the energy dissipation (E) in the system (Fig. 3.14). I show the variation of E_N vs γ_0 for $\phi = 0.35$, with different surfactant concentrations (c) in Fig. 3.13. Remarkably, I find that the non-monotonic behavior of E_N completely disappears with the addition of sufficient amount of surfactant (see Fig. 3.13) implying that strain stiffening also goes away under this condition (shown in Fig. 3.15). This observation further confirms that adhesive interactions give rise to the non-linear strain stiffening in the system through the shear induced deformation of fractal particle clusters. Moreover, with increasing values of c, the velocity across the shearing gap also approaches a linear profile from a shear-banding one (Fig. 3.16).

Finally, I summarize our results for the CS in Paraffin oil system using a generalized phase diagram in Fig. 3.17. For lower values of ϕ (below ϕ_{alp}), gravitational settling forms

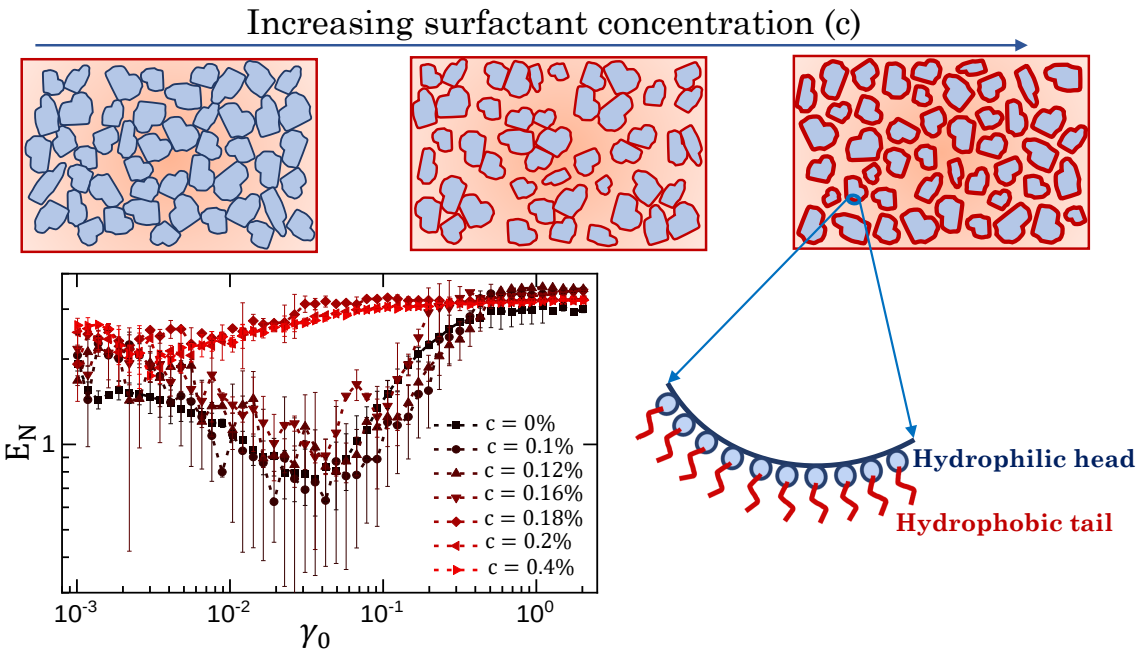

Figure 3.13: Schematics showing the gradual dispersion of fractal clusters with increasing surfactant concentration (top row). The adsorption of the hydrophilic heads of the surfactant molecules on the particle surface is also indicated. Variation of normalized energy dissipation E_N as a function of strain amplitude γ_0 for volume fraction $\phi = 0.35$ for increasing surfactant concentration as indicated (bottom left panel). Here, the error bars indicate standard deviation for two independent experimental runs.

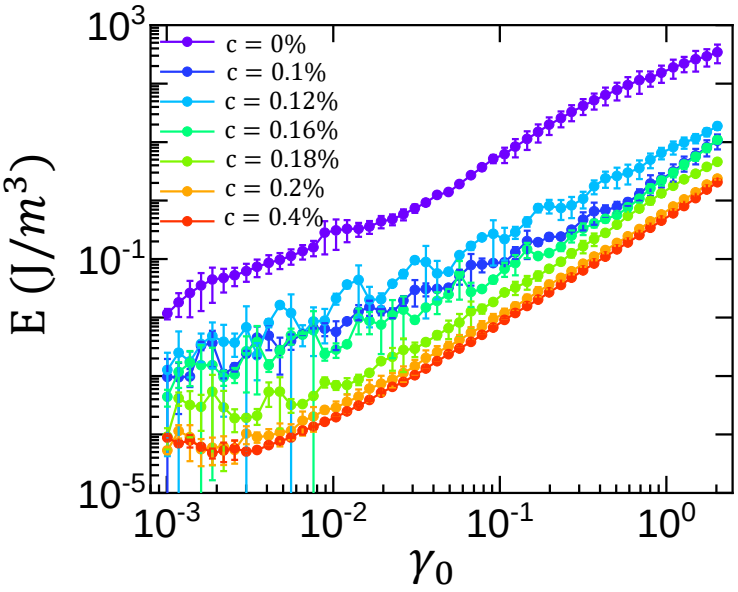

Figure 3.14: Variation of dissipated energy density (E) as a function of strain amplitude γ_0 for volume fraction $\phi = 0.35$ with increasing concentration of surfactant (c).

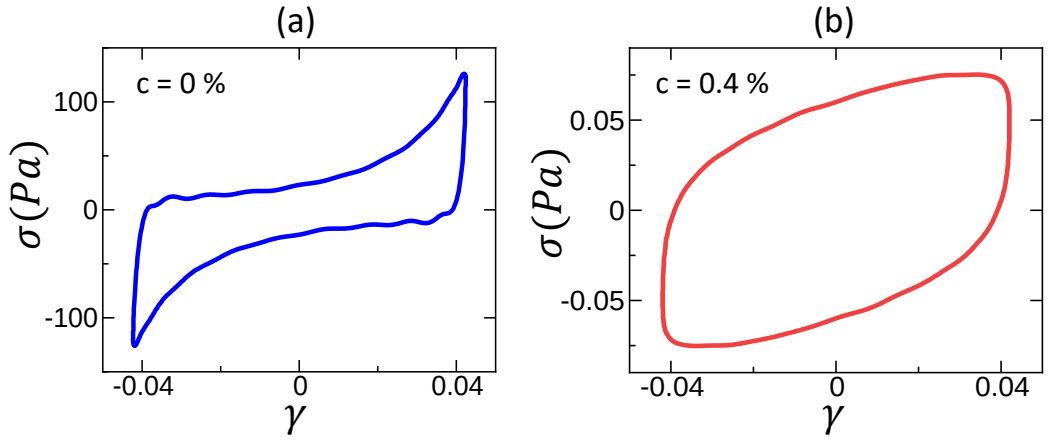

Figure 3.15: Elastic Lissajous plot at an intermediate value of strain amplitude γ_0 during the LAOS (Large Amplitude Oscillatory Shear) measurement for volume fraction $\phi = 0.4$ without surfactant (panel (a)) and with a surfactant concentration c = 0.4 % (panel (b)). I see that with the addition of sufficient amount of surfactant, the stress values dramatically drop and also the strain stiffening behaviour completely disappears.

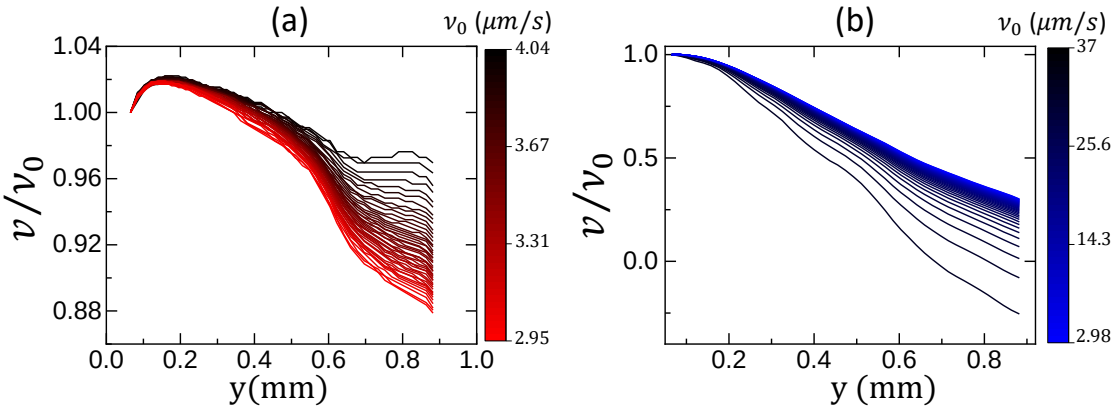

Figure 3.16: Velocity profiles across the gap between the cone and the plate normalized by the instantaneous maximum velocity of the sample (near the moving plate beyond the plate roughness) for sample volume fraction $\phi = 0.4$ with surfactant concentration c = 0.4 % at strain amplitude (a) $\gamma_0 = 0.1$ and (b) $\gamma_0 = 0.5$. The colour gradient indicates the instantaneous plate velocity v_0 during an oscillatory applied strain cycle.

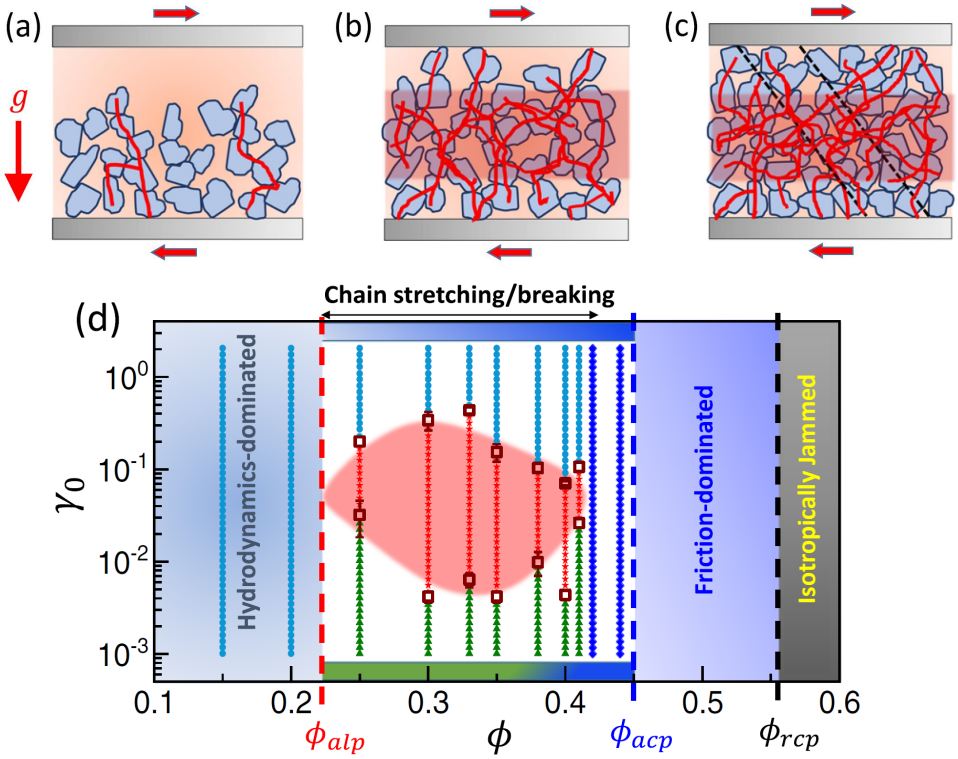

Figure 3.17: Schematics showing the configurations under gravity for different volume fractions (ϕ) of CS in Paraffin oil during the rheology measurements. (a) For $\phi < \phi_{alp}$, the adhesive particle contacts (red solid lines) cannot span the entire gap due to settling. (b) $\phi_{alp} < \phi < \phi_{acp}$ contact networks span the gap. In this region, the system forms load bearing chains under extension but not along the compression direction. For even higher ϕ values (panel (c)), such compressive force chains (dashed black lines) stabilized by inter-particle friction can also form. The shaded region midway from both the plates (panels b and c) indicate the solid-like region inside the sample. These scenarios are summarized in a phase diagram in panel (d) in the parameter plane of ϕ and strain amplitude (γ_0). Different regions are marked based on the rheological response of the system. For $\phi < \phi_{alp}$ I get a viscous behavior (light blue circles) over the entire range of γ_0. For $\phi_{alp} < \phi < \phi_{acp}$ I observe a non-monotonic strain response of E_N related to the stretching and breaking of particle chains. The data points shown by green triangles indicate the region where $E_N \approx E_N^0$; red stars indicate the region where $E_N < E_N^0$ and strain stiffening is observed; light blue circles mark the region of $E_N > E_N^0$ where the system shows progressively larger dissipation. Such non-monotonicity disappears (dark blue diamonds) near $\phi \to \phi_{acp}$, where $E_N > E_N^0$ for all values of γ_0. $\phi = \phi_{rcp}$ indicates the random close packing for CS particles in the limit of hard-sphere repulsion. For $\phi \geq \phi_{rcp}$, the system is isotropically jammed. The critical volume fractions ϕ_{alp}, ϕ_{acp} and ϕ_{rcp} are obtained from the particle-settling experiments. The error bars at the strain stiffening boundaries are estimated from the standard deviation of three independent measurements indicating fuzziness associated with the strain stiffening boundaries.

a bed of particles near the bottom plate and a solvent layer is observed near the top cone of the rheometer, as shown by the schematic Fig. 3.17(a). The contact networks formed by the particles cannot span the entire gap between the shearing cone and plate, and the system behavior remains viscous dominated over the entire range of strain amplitude (Fig. 3.17(d)). However, for values of ϕ larger than ϕ_{alp}, the settled particle bed can span the entire shear-gap (schematic Fig. 3.17(b)). The system develops a finite yield stress like a soft visco-elastic solid. In the regime $\phi > \phi_{alp}$ (but well below ϕ_{acp}), the system shows significant resistance in response to applied strain due to the stretching of adhesive contacts, however, ϕ is still low enough to not support system spanning force chains along the compression direction. Here, the system transforms from a quasi-linear visco-elastic solid to a strain-stiffening solid ($E_N < E_N^0$) and finally to a viscous/plastic material ($E_N > E_N^0$) with increasing γ_0, as shown in Fig. 3.17(d). I note that the strain stiffening does not take place for $\gamma_0 < 0.003$ (Fig. 3.17(d)). This indicates that significant deformation of the fractal clusters are required for the observed strain stiffening response. Interestingly, the strain stiffening disappears for ϕ values close to ϕ_{acp}. For such high volume fractions, the system spanning force chains can also form along the compression direction (Fig. 3.17(c)) [37, 56]. Thus, strain deformations give rise to considerable frictional interaction between the particles. This results in an enhanced dissipation masking the strain stiffening response. This explains the fact that despite significant adhesive interactions, E_N remains higher than E_N^0 in this regime. Although, strain stiffening has been reported for colloidal gels formed by Brownian particles [41, 43] such complex non-monotonic variation of strain stiffening as a function of both strain amplitude and particle volume fraction have never been observed for these systems. I also observe that close to ϕ_{acp} sample mixing becomes extremely difficult and sample appears almost dry. Due to this I can not experimentally probe the regime $\phi_{acp} < \phi < \phi_{rcp}$ (Fig. 3.17(d)). Based on our present statistical accuracy, the complex nature of the phase boundaries seems to be a genuine feature of the system. Nonetheless, in future an improved statistical accuracy by considering much larger number of independent experimental runs and varying system sizes can reveal the nature of the phase boundaries more accurately. I want to reemphasize that the complex dynamics originating from the stretching/breaking of adhesive contacts and formation of frictional contacts take place near the shearing boundaries, while the bulk of the sample moves like a solid-plug as pointed out in Fig. 3.17(b) and (c). This is a major new addition to the recent physical picture of the flow behavior in similar systems [37].

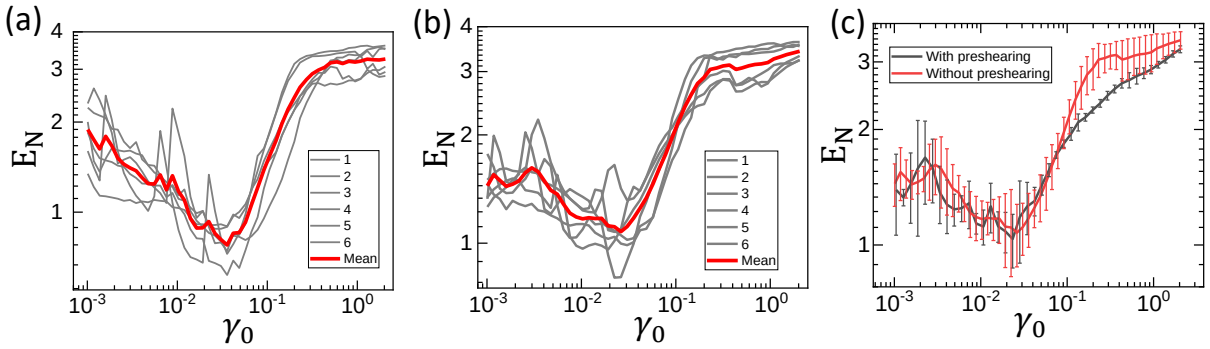

Figure 3.18: Variation of normalized energy dissipation (E_N) as a function of strain amplitude γ_0 for six independent measurements (gray lines) along with the average of these six measurements (thick red line) for Cornstarch (CS) in Paraffin oil with volume fraction $\phi = 0.35$ (panel (a)) and $\phi = 0.4$ (panel (b)). (c) Variation of E_N vs γ_0 in the presence and absence of pre-shearing. For the pre-sheared data, average is taken between 3 independent measurements. For each measurement, I performed two LAOS runs on the same loading of the sample with a 100s interval in between when the sample was left undisturbed (see Materials and methods). So, the second LAOS run gives the pre-sheared data. The red curve (measurements with no pre-shearing) is obtained from the measurements shown in panel (b). For both these data error bars indicate standard deviations.

3.4 Conclusion

I study yielding and energy dissipation in granular suspensions of adhesive frictional particles. I find that the normalized energy dissipation E_N shows an interesting non-monotonic dependence on both applied strain amplitude (γ_0) and volume fraction (ϕ). I show that such non-monotonic behavior is intimately linked to the interplay between interparticle adhesion and friction in the system. From optical imaging, I observe strain localization and random spatio-temporal fluctuations in local velocity gradients. Using stroboscopic image sampling, I demonstrate a direct correlation between such fluctuations and irreversible particle rearrangements. Interestingly, the non-monotonic variation of E_N for intermediate γ_0 values is similar to that observed for variation of system energy in poorly annealed glasses [8, 62, 63], where the applied oscillatory strain can mechanically anneal the system which can compete with the initial thermal annealing. However, contrary to the numerical studies mentioned above, for our system I observe non-monotonicity in a derived quantity E_N, but, the dissipated energy density (E) remains monotonic in γ_0 (Fig. 3.1(d)). Furthermore, I do not observe any increase in the bulk rigidity of the system for intermediate strain values as confirmed by the steady drop in G' with increasing γ_0 (Fig. 3.1(a)). This indicates that the nature of non-monotonicity observed in E_N is

different from that observed in numerical studies on poorly annealed glasses. I also find that pre-shearing (mechanical annealing) does not have an effect on the non-monotonicity of E_N (Fig. 3.18). However, possible connection between the observed non-monotonicity in glassy and adhesive granular systems needs more detailed exploration in future.

A salient feature of our study is that I directly measure the critical jamming packing fractions using particle-settling experiments. Remarkably, I show that the critical jamming packing fractions, estimated from these experiments, successfully capture the essential physics behind the different flow regimes observed over a wide range of volume fractions and applied strain amplitudes. For particle settling experiments, density mismatch between the particles and the solvent is required. However, the striking rheological response like, non-linear strain stiffening and plasticity is found to be quite a general feature of adhesive granular suspensions which are unaffected by gravitational effects.

I find, using stroboscopic imaging, a clear difference between irreversible particle arrangements above and below yielding: below yielding such events happen throughout the system, whereas, above yielding they remain confined near the boundaries. To our knowledge such difference has not been reported in the context of yielding in adhesive granular suspensions. Furthermore, existing theoretical models generally assume a system-wide fluidization beyond yielding which need not be true always, as I clearly demonstrate from the coexisting solid- and fluid-like regions in these systems. Thus, our experiments put additional constraints on the recently proposed models [36, 37] of yielding in adhesive granular suspensions. As mentioned earlier, boundary imaging can probe only a thin layer of the sample near the suspension-air interface. It will be interesting to extend similar stroboscopic analysis for the entire system in three-dimension. For this, one can consider techniques like ultrasound velocimetry as mentioned in [44]. However, this remains outside the scope of the present study.

The non-linear strain stiffening observed for intermediate applied strain values is reminiscent of similar phenomena in semiflexible biopolymer networks [64] and colloidal gels forming strand-like structures [41, 43]. Using fluorescently labeled CS particles, I indeed observe system-spanning network-like connected structures formed by fractal clusters of adhesive particles. Thus, for intermediate packing fractions, the strain stiffening can take place due to the stretching of these contacts for moderate strain values, but larger applied strains can break the contacts giving rise to enhanced plasticity and dissipation. Addition of surfactant inhibits the adhesive interactions and thus disrupts the formation of such system spanning connected structures. Consequently, no strain stiffening is observed. Importantly, the nature of strain stiffening and its complex dependence on both

strain amplitude and particle volume fractions, as observed here for the granular systems, is distinct from that reported for colloidal gels. This is not surprising in view of the difference in yielding mechanism in these two classes of systems as highlighted in recent studies [37, 38]. However, a detailed phase diagram over a large parameter range similar to our study is currently lacking for colloidal gels which remains an interesting future direction. It is important to note that the presence of surfactant molecules on the particle surface not only reduces the interparticle adhesion, but can also significantly modify the interparticle friction coefficients. However, quantifying such effects in our system remains an interesting future challenge.

Our study provides a complete picture of flow and yielding behavior in dense granular suspensions of adhesive amorphous particles and can have important implications for both theoretical as well as experimental studies in future.

3.5 Appendix

3.5.1 Appendix-1: Movie description

20X: In this movie, I show an animation of the reconstructed 3D images (obtained from the maximum intensity projection for each image in the z-stack) of CS in Paraffin oil without (left panel) and with 0.2 % surfactant (right panel) under 20X magnification. In both the cases, the initial volume fraction of CS is 0.05. The z-stack images were captured using a confocal microscope with a z-spacing of 0.68 μm once the particles are settled to form a stable bed. Since the intensity of the images gets reduced with increasing depth due to the opaque nature of the particles, gamma and brightness/contrast correction was applied to the images before the 3D reconstruction. It can be seen that the thickness of the 3D volume is more for the adhesive system (without surfactant) as compared to that for the repulsive system (with added surfactant). This confirms our hypothesis that once the inter-particle adhesive interaction is removed, the particle strands can no longer sustain their weight and hence collapse to form a more uniformly distributed bed. The 2D distribution of the particles in the x-y plane (as seen from the starting images in the animation) shows a very uniform distribution in the repulsive case (with surfactant) as compared to the adhesive case (without surfactant) where clear particle aggregation and void formation can be observed.

40X: In this movie, I show an animation of the reconstructed 3D images of CS in oil system without (left panel) and with surfactant (right panel) under 40X magnification.

Other parameters are same as for the movie 20X. Once again the thickness of the 3D volume is more in the case without surfactant (the adhesive system) as compared to the surfactant case (the repulsive system). The 2D image of the particle distribution in x-y plane with the higher magnification shows the structural heterogeneity in the adhesive case even more clearly than that observed with 20X.

3.5.2 Appendix-2: Calculation of fractal dimension

Due to the large refractive index mismatch between the Cornstarch particles and Paraffin oil, I cannot look deep inside the 3-D particle packing (inside the settled bed) using Confocal imaging. Also, due to the large size of the particles (avg. diameter ≈ 15 μm), standard light scattering techniques are not feasible to determine 3-D fractal dimension in our system. As mentioned in [65], the fractal morphology in 3D systems only extends upto a microscopic cutoff length scale, beyond which the system follows a R^3 dependence. To quantify the fractal nature of the system keeping the above mentioned constraints in mind, I use Confocal imaging to determine the 2-D fractal dimension. From the Confocal slices obtained from z-stack I find out relation between the projected area (A) and the perimeter (P) for many different cluster sizes. For non-fractal assemblies $A \sim P^2$ whereas for fractal systems $A \sim P^{d_f}$ with $d_f < 2$. I show the log-log plot of A vs P in Fig. 3.4 where I observe a power-law behaviour. The slope of the curve gives the fractal dimension d_f. From Fig. 3.4 I get $d_f \approx 1.2$, indicating the fractal nature of the system.

3.5.3 Appendix-3: Calculation of average stress scale inside the settled bed

To estimate the average inter-particle stress inside a stable settled bed, I consider the total stress acting on a Cornstarch (CS) particle at the mid-point (point 'O') of the settled bed (along the length of the tube). Here, I assume a uniform distribution of CS particles inside the settled bed. The total stress on a particle at 'O' has two contributions: stress acting on a particle at this point assuming the particle to be isolated and the stress due to part of the bed above it (for gravitational settling) or, the part towards the axis of rotation (for settling under centrifugation).

Considering a typical case of centrifugation, the distance of the mid-point of bed from the axis of rotation is $R = 15.17$ cm. The length of half of the settled bed is $l = 1.77$ cm. The distance of the center of mass of the part closer to the axis of rotation compared to the point 'O' is $R_1 = R - l/2 = 14.3$ cm. I use $R_{CS} = 7.5$ μm (refer to section 2.3.1) as

the average particle radius, and the rotation speed $\omega \approx 209$ rad/s (converted from 2000 rpm). The density of CS and Paraffin oil (PO) is 1.6 g/cc and 0.89 g/cc respectively. The volume fraction of the starting sample is 0.2, however, after centrifugation the volume fraction inside the bed is found to be $\phi_{bed} \approx 0.44$.

So, the stress on the free particle is $\sigma_{isolated} = \frac{4}{3} R_{CS}(\rho_{CS} - \rho_{PO})\,\omega^2 R$ and that due to half of the bed above is $\sigma_{bed} = l\,(\rho_{CS} - \rho_{PO})\,\omega^2 R_1 \phi_{bed}$. The total stress value I get is 35 kPa which is much higher than the maximum stress I observe in our rheological measurements ($\approx$ 150 Pa) for the sample with the highest volume fraction ($\phi = 0.44$).

Similarly for gravitational settling, the stress on the isolated particle is $\sigma_{isolated} = \frac{4}{3} R_{CS}(\rho_{CS} - \rho_{PO})$g and stress from the half of the bed on top is $\sigma_{gravity} = l(\rho_{CS} - \rho_{PO})$g, the sum of which comes out to be 123 Pa (I use g= $9.8 m/s^2$).

In both the cases of settling under gravity and centrifugation, I find that the contribution from the isolated particle is negligible in comparison to the contribution from the part of the settled bed that comes into play.

3.5.4 Appendix-4: Estimation of the surface density of surfactant molecules

As mentioned in the Results and discussion, with the addition of sufficient amount of surfactant, the adhesive interaction between the Cornstarch (CS) particles gets eliminated. I use the non-ionic surfactant Span-60 which has a molar mass of 430.62 g. For simplification, I assume CS particles to be spherical with a radius (R_{CS}) of 7.5 μm (see Fig. 2.6).

For a given volume of CS (V_{CS}) and Paraffin oil (V_{PO}), volume fraction of the suspension ($\phi = \frac{V_{CS}}{V_{CS}+V_{PO}}$). From V_{CS} I calculate the number of CS particles: $N_{CS} = \frac{V_{CS}}{\frac{4}{3}\pi R_{CS}^3}$. Now, using the surfactant concentration (c), I get the total mass of the surfactant molecules (m_S) from the relation $c = \frac{m_S}{m_S+m_{CS}}$, where m_{CS} is the total mass of CS particle. I note, $m_{CS} = \rho\ V_{CS}$ and $\rho = 1.6$ gm/cc, the density of CS particles. From this I get the total, number of surfactant molecules (N_S) as $\frac{m_S \times N_A}{430.62}$ (N_A: Avogadro Number). So I calculate the number of surfactant molecules per CS particle as $N = \frac{N_S}{N_{CS}}$ and the average surface density as $\frac{N}{4\pi R_{CS}^2}$.

I estimate N and the average surface density (Γ) of the surfactant molecules on the particle surface in the following three cases: first when the surfactant concentration is just enough to start reducing the adhesive interaction between the particles. From Fig. 3.10(d) I see that this happens at a surfactant concentration of 0.09% (where the settled

bed packing fraction begins to increase from ϕ_{acp} value). At this concentration of surfactant, for a starting volume fraction of 0.2, I get $N = 3.6 \times 10^9$ and $\Gamma = 5 \times 10^6/\mu\text{m}^2$.
Next I calculate the surfactant density at a concentration of 0.6% (Fig. 3.10(d)) which is the minimum c required for the settled bed packing fraction to just reach ϕ_{rcp}. This is the minimum surface coverage of the surfactant molecules that is just enough to completely suppress the adhesion between the particles. Under this condition, for a starting volume fraction of 0.2, I get $N = 2.4 \times 10^{10}$ and $\Gamma = 3.4 \times 10^7/\mu\text{m}^2$.
Lastly, I calculate the surfactant coverage for volume fraction 0.35 at a surfactant concentration of 0.18% (Fig. 3.13). At this coverage, I no longer get a non-monotonic variation of E_N. This coverage should be somewhere in between the previous two cases described above. I get $N = 6.7 \times 10^9$ and $\Gamma = 9.4 \times 10^6/\mu\text{m}^2$, which is indeed between the two limits as expected.

Bibliography

[1] Sebanti Chattopadhyay, Sharadhi Nagaraja, and Sayantan Majumdar. Effect of adhesive interaction on strain stiffening and dissipation in granular gels undergoing yielding. *Commun. Phys.*, 5(126):1–10, May 2022.

[2] Jie Lin, Edan Lerner, Alberto Rosso, and Matthieu Wyart. Scaling description of the yielding transition in soft amorphous solids at zero temperature. *Proc. Natl. Acad. Sci. U.S.A.*, 111(40):14382–14387, Oct 2014.

[3] Daniel Bonn, Morton M. Denn, Ludovic Berthier, Thibaut Divoux, and Sébastien Manneville. Yield stress materials in soft condensed matter. *Rev. Mod. Phys.*, 89(3):035005, Aug 2017.

[4] Antina Ghosh, Zoe Budrikis, Vijayakumar Chikkadi, Alessandro L Sellerio, Stefano Zapperi, and Peter Schall. Direct observation of percolation in the yielding transition of colloidal glasses. *Physical review letters*, 118(14):148001, 2017.

[5] N Koumakis and G Petekidis. Two step yielding in attractive colloids: transition from gels to attractive glasses. *Soft Matter*, 7(6):2456–2470, 2011.

[6] KN Pham, G Petekidis, D Vlassopoulos, SU Egelhaaf, PN Pusey, and WCK Poon. Yielding of colloidal glasses. *EPL (Europhysics Letters)*, 75(4):624, 2006.

[7] Vincent Grenard, Thibaut Divoux, Nicolas Taberlet, and Sébastien Manneville. Timescales in creep and yielding of attractive gels. *Soft matter*, 10(10):1555–1571, 2014.

[8] Premkumar Leishangthem, Anshul D. S. Parmar, and Srikanth Sastry. The yielding transition in amorphous solids under oscillatory shear deformation. *Nat. Commun.*, 8(14653):1–8, Mar 2017.

[9] Smarajit Karmakar, Edan Lerner, and Itamar Procaccia. Statistical physics of the yielding transition in amorphous solids. *Phys. Rev. E*, 82(5):055103, Nov 2010.

[10] Craig E. Maloney and Anaël Lemaître. Amorphous systems in athermal, quasistatic shear. *Phys. Rev. E*, 74(1):016118, Jul 2006.

[11] Nathan C. Keim and Paulo E. Arratia. Yielding and microstructure in a 2D jammed material under shear deformation. *Soft Matter*, 9(27):6222–6225, 2013.

[12] DV Denisov, KA Lörincz, JT Uhl, KA Dahmen, and P Schall. Universality of slip avalanches in flowing granular matter. *Nature communications*, 7(1):1–6, 2016.

[13] Prabhat K. Jaiswal, Itamar Procaccia, Corrado Rainone, and Murari Singh. Mechanical Yield in Amorphous Solids: A First-Order Phase Transition. *Phys. Rev. Lett.*, 116(8):085501, Feb 2016.

[14] Ido Regev, John Weber, Charles Reichhardt, Karin A. Dahmen, and Turab Lookman. Reversibility and criticality in amorphous solids. *Nat. Commun.*, 6(8805):1–8, Nov 2015.

[15] E. D. Knowlton, D. J. Pine, and L. Cipelletti. A microscopic view of the yielding transition in concentrated emulsions. *Soft Matter*, 10(36):6931–6940, Aug 2014.

[16] Gaurav Prakash Shrivastav, Pinaki Chaudhuri, and Jürgen Horbach. Yielding of glass under shear: A directed percolation transition precedes shear-band formation. *Phys. Rev. E*, 94(4):042605, Oct 2016.

[17] Alexandre Nicolas, Ezequiel E Ferrero, Kirsten Martens, and Jean-Louis Barrat. Deformation and flow of amorphous solids: Insights from elastoplastic models. *Reviews of Modern Physics*, 90(4):045006, 2018.

[18] Srikanth Sastry. Models for the yielding behaviour of amorphous solids, 2020.

[19] Yuchen Zhao, Jonathan Barés, and Joshua ES Socolar. Yielding, rigidity, and tensile stress in sheared columns of hexapod granules. *Physical Review E*, 101(6):062903, 2020.

[20] Hugh J Barlow, James O Cochran, and Suzanne M Fielding. Ductile and brittle yielding in thermal and athermal amorphous materials. *Physical Review Letters*, 125(16):168003, 2020.

[21] Gavin J Donley, John R de Bruyn, Gareth H McKinley, and Simon A Rogers. Time-resolved dynamics of the yielding transition in soft materials. *Journal of Non-Newtonian Fluid Mechanics*, 264:117–134, 2019.

[22] Joshua A Dijksman, Geert H Wortel, Louwrens TH van Dellen, Olivier Dauchot, and Martin van Hecke. Jamming, yielding, and rheology of weakly vibrated granular media. *Physical review letters*, 107(10):108303, 2011.

[23] Chen Liu, Suman Dutta, Pinaki Chaudhuri, and Kirsten Martens. Elastoplastic approach based on microscopic insights for the steady state and transient dynamics of sheared disordered solids. *Physical Review Letters*, 126(13):138005, 2021.

[24] Andrea J. Liu and Sidney R. Nagel. Jamming is not just cool any more. *Nature*, 396:21–22, Nov 1998.

[25] Abdoulaye Fall, N. Huang, F. Bertrand, G. Ovarlez, and Daniel Bonn. Shear Thickening of Cornstarch Suspensions as a Reentrant Jamming Transition. *Phys. Rev. Lett.*, 100(1):018301, Jan 2008.

[26] Ryohei Seto, Abhinendra Singh, Bulbul Chakraborty, Morton M. Denn, and Jeffrey F. Morris. Shear jamming and fragility in dense suspensions. *Granular Matter*, 21(3):82–8, Aug 2019.

[27] Adolfo Vázquez-Quesada, Roger Tanner, and Marco Ellero. Shear Thinning of Noncolloidal Suspensions. *Phys. Rev. Lett.*, 117(10), Aug 2016.

[28] Eric Brown and Heinrich M Jaeger. Shear thickening in concentrated suspensions: phenomenology, mechanisms and relations to jamming. *Reports on Progress in Physics*, 77(4):046602, 2014.

[29] Xiang Cheng, Jonathan H. McCoy, Jacob N. Israelachvili, and Itai Cohen. Imaging the Microscopic Structure of Shear Thinning and Thickening Colloidal Suspensions. *Science*, 333(6047):1276–1279, Sep 2011.

[30] Subhransu Dhar, Sebanti Chattopadhyay, and Sayantan Majumdar. Signature of jamming under steady shear in dense particulate suspensions. *J. Phys.: Condens. Matter*, 32(12):124002, Dec 2019.

[31] Abdoulaye Fall, François Bertrand, Guillaume Ovarlez, and Daniel Bonn. Yield stress and shear banding in granular suspensions. *Physical review letters*, 103(17):178301, 2009.

[32] Hugo Perrin, Cécile Clavaud, Matthieu Wyart, Bloen Metzger, and Yoël Forterre. Interparticle friction leads to nonmonotonic flow curves and hysteresis in viscous suspensions. *Physical Review X*, 9(3):031027, 2019.

[33] Yoël Forterre and Olivier Pouliquen. Flows of dense granular media. *Annu. Rev. Fluid Mech.*, 40:1–24, 2008.

[34] BM Guy, Michiel Hermes, and Wilson CK Poon. Towards a unified description of the rheology of hard-particle suspensions. *Physical review letters*, 115(8):088304, 2015.

[35] Dion J. Koeze and Brian P. Tighe. Sticky Matters: Jamming and Rigid Cluster Statistics with Attractive Particle Interactions. *Phys. Rev. Lett.*, 121(18):188002, Nov 2018.

[36] BM Guy, JA Richards, DJM Hodgson, E Blanco, and WCK Poon. Constraint-based approach to granular dispersion rheology. *Physical review letters*, 121(12):128001, 2018.

[37] J. A. Richards, B. M. Guy, E. Blanco, M. Hermes, G. Poy, and W. C. K. Poon. The role of friction in the yielding of adhesive non-Brownian suspensions. *J. Rheol.*, 64(2):405, Mar 2020.

[38] James A. Richards, Rory E. O'Neill, and Wilson C. K. Poon. Turning a yield-stress calcite suspension into a shear-thickening one by tuning inter-particle friction. *Rheol. Acta*, pages 1–10, Nov 2020.

[39] Abhinendra Singh, Christopher Ness, Ryohei Seto, Juan J. de Pablo, and Heinrich M. Jaeger. Shear Thickening and Jamming of Dense Suspensions: The ``Roll" of Friction. *Phys. Rev. Lett.*, 124(24):248005, Jun 2020.

[40] Matthieu Wyart and ME Cates. Discontinuous shear thickening without inertia in dense non-brownian suspensions. *Physical review letters*, 112(9):098302, 2014.

[41] T. Gisler, R. C. Ball, and D. A. Weitz. Strain Hardening of Fractal Colloidal Gels. *Phys. Rev. Lett.*, 82(5):1064–1067, February 1999.

[42] Jader Colombo and Emanuela Del Gado. Stress localization, stiffening, and yielding in a model colloidal gel. *Journal of rheology*, 58(5):1089–1116, 2014.

[43] Jan Maarten van Doorn, Joanne E. Verweij, Joris Sprakel, and Jasper van der Gucht. Strand Plasticity Governs Fatigue in Colloidal Gels. *Phys. Rev. Lett.*, 120(20):208005, May 2018.

[44] Lydiane Bécu, Sébastien Manneville, and Annie Colin. Yielding and Flow in Adhesive and Nonadhesive Concentrated Emulsions. *Phys. Rev. Lett.*, 96(13):138302, Apr 2006.

[45] Peter Schall and Martin Van Hecke. Shear bands in matter with granularity. *Annual Review of Fluid Mechanics*, 42:67–88, 2010.

[46] Teresa Liberto, Marie Le Merrer, Sébastien Manneville, and Catherine Barentin. Interparticle attraction controls flow heterogeneity in calcite gels. *Soft Matter*, 16(40):9217–9229, Oct 2020.

[47] Ehsan Irani, Pinaki Chaudhuri, and Claus Heussinger. Impact of Attractive Interactions on the Rheology of Dense Athermal Particles. *Phys. Rev. Lett.*, 112(18):188303, May 2014.

[48] Ehsan Irani, Pinaki Chaudhuri, and Claus Heussinger. Athermal rheology of weakly attractive soft particles. *Phys. Rev. E*, 94(5):052608, Nov 2016.

[49] Pinaki Chaudhuri, Ludovic Berthier, and Lydéric Bocquet. Inhomogeneous shear flows in soft jammed materials with tunable attractive forces. *Phys. Rev. E*, 85(2):021503, Feb 2012.

[50] Vishwas Venkatesh Vasisht, Gabrielle Roberts, and Emanuela Del Gado. Emergence and persistence of flow inhomogeneities in the yielding and fluidization of dense soft solids. *Physical Review E*, 102(1):010604, 2020.

[51] Murari Singh, Misaki Ozawa, and Ludovic Berthier. Brittle yielding of amorphous solids at finite shear rates. *Physical Review Materials*, 4(2):025603, 2020.

[52] Scott R Waitukaitis. *Impact-activated solidification of cornstarch and water suspensions*. Springer, 2014.

[53] T Neidhöfer, Manfred Wilhelm, and Hans Wolfgang Spiess. Fourier-transform-rheology on linear polystyrene melts. *Applied Rheology*, 11(3):126–133, 2001.

[54] V. Trappe, V. Prasad, L. Cipelletti, P. N. Segre, and D. A. Weitz. Jamming phase diagram for attractive particles. *Nature*, 411(6839):772–775, June 2001.

[55] J. Clerk Maxwell. L. On the calculation of the equilibrium and stiffness of frames. *London, Edinburgh, and Dublin Philosophical Magazine and Journal of Science*, 27(182):294–299, Apr 1864.

[56] Ivo R. Peters, Sayantan Majumdar, and Heinrich M. Jaeger. Direct observation of dynamic shear jamming in dense suspensions. *Nature*, 532:214–217, Apr 2016.

[57] K. van der Vaart, Yasser Rahmani, Rojman Zargar, Zhibing Hu, Daniel Bonn, and Peter Schall. Rheology of concentrated soft and hard-sphere suspensions. *J. Rheol.*, 57(4):1195, Jun 2013.

[58] FKG Schreuders, LMC Sagis, I Bodnár, P Erni, RM Boom, and AJ van der Goot. Small and large oscillatory shear properties of concentrated proteins. *Food Hydrocolloids*, 110:106172, 2021.

[59] Rubens R. Fernandes, Diogo E. V. Andrade, Admilson T. Franco, and Cezar O. R. Negrão. The yielding and the linear-to-nonlinear viscoelastic transition of an elasto-viscoplastic material. *J. Rheol.*, 61(5):893, Jul 2017.

[60] Nicolas Fernandez, Roman Mani, David Rinaldi, Dirk Kadau, Martin Mosquet, Hélène Lombois-Burger, Juliette Cayer-Barrioz, Hans J. Herrmann, Nicholas D. Spencer, and Lucio Isa. Microscopic Mechanism for Shear Thickening of Non-Brownian Suspensions. *Phys. Rev. Lett.*, 111(10):108301, September 2013.

[61] Chiao-Peng Hsu, Shivaprakash N. Ramakrishna, Michele Zanini, Nicholas D. Spencer, and Lucio Isa. Roughness-dependent tribology effects on discontinuous shear thickening. *Proc. Natl. Acad. Sci. U.S.A.*, 115(20):5117–5122, May 2018.

[62] Chen Liu, Ezequiel E Ferrero, Eduardo A Jagla, Kirsten Martens, Alberto Rosso, and Laurent Talon. The fate of shear-oscillated amorphous solids. *arXiv preprint arXiv:2012.15310*, 2020.

[63] Wei-Ting Yeh, Misaki Ozawa, Kunimasa Miyazaki, Takeshi Kawasaki, and Ludovic Berthier. Glass stability changes the nature of yielding under oscillatory shear. *Physical Review Letters*, 124:225502, 2020.

[64] Cornelis Storm, Jennifer J. Pastore, F. C. MacKintosh, T. C. Lubensky, and Paul A. Janmey. Nonlinear elasticity in biological gels. *Nature*, 435:191–194, May 2005.

[65] J. Bibette, T. G. Mason, Hu Gang, and D. A. Weitz. Kinetically induced ordering in gelation of emulsions. *Phys. Rev. Lett.*, 69(6):981–984, August 1992.

CHAPTER

FOUR

Mechanical memory formation in adhesive granular gels

All the results presented in this chapter are published in Chattopadhyay and Majumdar, J. Chem. Phys. 156, 241102 (2022) [1].

4.1 Introduction

Far-from-equilibrium systems can retain an imprint of past perturbations. Such memory retention is a common feature of many soft matter systems as explained in section 1.4.3. Significant recent interest has been on the memory formation in amorphous solids [2, 3, 4, 5]. Despite the diversity in microscopic details, presence of long-range correlations and complex energy landscapes, these materials show very similar localized rearrangements under stress. Each of such rearrangements can be thought of as a transition between two local energy minima of the system [6, 7]. Interestingly, these systems can also reach a steady state under cyclic deformations encoding a memory of the deformation amplitude. The approach to a steady state and memory formation in amorphous solids under cyclic shear has been demonstrated in numerical simulations of glassy and frictional granular systems [2, 3, 8, 9, 10, 11, 12]. Experimental studies have explored memory formation in soft glassy systems in both 2-D [4, 5, 13, 14] and 3-D [15], colloidal gels [16], cross-linked biopolymer networks [17, 18] . Many of these systems also have the ability to remember multiple inputs even in the absence of external noise.

The signature of the memory formed under cyclic shear is reflected as a sudden increase in particle Mean Square Displacement (MSD) as the readout strain crosses the training strain amplitude marking an onset of irreversibility in the system. However, the effect of such reversible-irreversible transition on the mechanical properties of the bulk material has rarely been explored. Experiments on dilute non-Brownian suspensions [19] and a soft glassy system of 2-D bubble raft [5] reports that encoding memory induces only a small change in shear modulus of the system. These observations indicate a limitation of widely tuning the material properties using an imposed training.

In this chapter, I report strong memory formation in an amorphous solid formed by dense granular suspensions of Cornstarch particles in Paraffin oil. I find that memory can be encoded for a wide range of strain amplitudes both above and below yielding. Remarkably, such memory effect is directly reflected as a sharp change in the differential shear modulus of the system. I observe that in the case of consecutive training with the strain amplitudes $\gamma_1 \leq \gamma_2 \leq ... \leq \gamma_n$, only the memory of largest amplitude γ_n is retained. However, if the system is trained with a smaller strain amplitude $\gamma_i (< \gamma_n)$ at the end of the training sequence, then the memory of γ_i can also be encoded. I show that such strong

memory originates from a training-induced non-trivial coupling-decoupling dynamics of the solid-like region inside bulk of the sample with the shearing plate via high shear rate bands near the boundaries. I also demonstrate the crucial role played by the inter-particle adhesion in forming such strong mechanical memory.

4.2 Materials and methods

For all our experiments, dense suspensions are prepared by dispersing Cornstarch (CS) particles (Sigma Aldrich) in Paraffin oil at a volume fraction (ϕ) = 0.4. Details of the particles and sample preparation are given in section 2.3.1. I use a MCR-702 stress controlled rheometer (Anton Paar), in separate motor transducer (SMT) mode, with sandblasted cone and plate geometry (C-P) for all our measurements (see section 2.2.1). The diameter of both cone and plate = 50 mm and the cone angle $\approx 2^{\circ}$. I do not pre-shear the samples after loading as the pre-shearing can also encode some memory in the system. I use the in-situ boundary imaging setup with a CCD camera (Lumenera) with a 5X long working distance objective (Mitutoyo) to capture the particle dynamics during the experiments (see section 2.2.1). Images are captured at a rate of 4 Hz with a resolution of 1000 x 2000 pixels^2 for all the measurements. For varying the adhesive interaction in the system, I use the non-ionic surfactant Span©60. More details about the system and the experimental set-up can be found in section 2.2.1 and [20].

4.3 Results and discussion

To train the system, I apply 300 cycles of a triangular-wave strain deformation with amplitude γ_T at a constant strain rate of 0.01 s^{-1}, as shown in Fig. 4.1(a). At this shear rate, the Reynolds Number $Re << 1$, indicating that inertial effects can be neglected. I use different colors to indicate the cycles in the beginning (magenta) and in the end (blue). In Fig. 4.1(b) and (c), I show the resulting intra-cycle stress (σ) as a function of number of cycles (N) for $\gamma_T = 0.02$. I notice that the peak stress (σ_{peak}) shows a systematic drop in the beginning (Fig. 4.1(b)) whereas near the end, it saturates to a steady state value of $\approx$ 15 Pa (Fig. 4.1(c)). Similar behaviour is also observed for other γ_T values (Fig. 4.1(d)). From Fig. 4.1(d) I also see that σ_{peak} for any N value decreases with increasing γ_T. This is related to the strain softening behaviour of the system: shear moduli G' and G'' decrease with increasing strain amplitude as shown in Fig. 4.2. I note that the nature of the stress waveform also evolves with N. This is more clearly observed from the

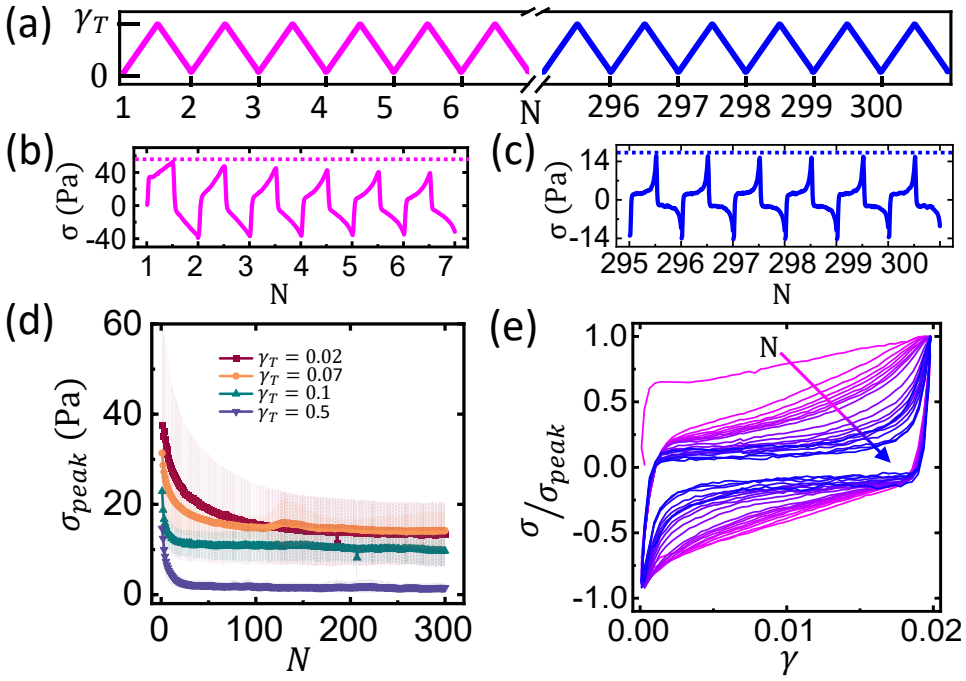

Figure 4.1: (a) Triangular wave strain deformation applied to the system for 300 cycles with a strain amplitude γ_T as indicated in the figure. The magenta color indicates cycles 1-6 and the blue color indicates cycles 295-300 as shown. (b) and (c) show intra-cycle stress (σ) vs number of cycles (N) corresponding to the regions mentioned in (a) for $\gamma_T = 0.02$. The dotted lines correspond to the peak stress (σ_{peak}) for N = 1 (panel (b)) and N = 295 (panel (c)) showing that σ_{peak} drops with increasing N in the beginning of the training, but finally saturates. (d) Variation of σ_{peak} with N for different γ_T values as indicated. The data is averaged over at least 3 independent measurements and error bars are the standard deviations. (e) Lissajous plots showing normalized intra-cycle stress (σ/σ_{peak}) vs. strain (γ) for few discrete N values. The arrow indicates increasing values of N.

variation of normalized σ vs. γ (Lissajous plot) in Fig. 4.1(e). Out of total 300 cycles, I show the Lissajous plots for only a few discrete N values. I observe from Fig. 4.1(e) that starting from a quasi-linear visco-elastic response for small values of N, the system gradually shows a highly non-linear response for larger N values, approaching a steady state. Also, as I go to larger N values, the slope of the Lissajous plots remains negligible for $\gamma << \gamma_T$ however, near γ_T, the slope increases sharply. This indicates the development of plasticity and strain-stiffening behaviour under training. Similar behaviour has also been observed for colloidal gels and cross-linked biopolymer networks under cyclic shear [17, 21].

Now, to see if the system encodes memory of the training amplitude, I apply a readout

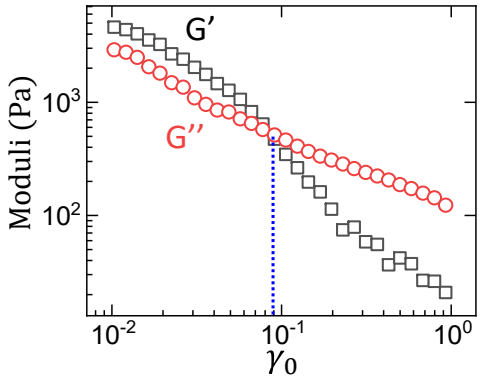

Figure 4.2: Variation of Elastic (G') and Viscous (G'') moduli as a function of applied oscillatory strain amplitude (γ_0). The dashed line indicates the strain value for the crossover of G' and G'' (yield strain), implying an onset of fluidization of the system. Here, I have used a sinusoidal waveform with angular frequency $\omega = 0.1$ rad/s. I found that the value of yield strain remains independent of ω (I have checked over the range 0.05 to 0.5 rad/s). The yielding onset obtained from the normalized energy dissipation [20] using triangular wave is in the same range as the yield strain obtained from the amplitude sweep data, as shown in this figure. Thus, in our case the nature of the imposed waveform does not affect yielding significantly (not shown).

after 300 cycles of training. The readout is a triangular wave pulse having the same strain rate of $0.01s^{-1}$ but with an amplitude $\gamma_R = 2\gamma_T$ as shown in Fig. 4.3(a) (top panel) for $\gamma_T = 0.02$. I plot σ vs γ of the readout cycle for $\gamma_T = 0.02$ in Fig. 4.3(b) (top panel, red curve). I observe a sharp change in the slope of σ as I cross $\gamma = \gamma_T$. For comparison, I apply the same readout to an untrained sample (Fig. 4.3(a), bottom panel) and plot the corresponding σ vs. γ in Fig. 4.3(b) (top panel, black curve) where I do not observe any such change. This difference is more clearly reflected in the differential shear modulus of the system $K(= \frac{d\sigma}{d\gamma})$ vs. γ as shown in Fig. 4.3(b) (bottom panel): the trained sample shows a sharp peak in K with value K_{peak} at $\gamma = \gamma_T$, indicating that the system encodes a strong memory of the training amplitude which can change the differential shear modulus of the system by a huge amount. In our case $K_{peak} >> K_{baseline}$ (with $K_{baseline}$ as the value of K at strain values slightly away from γ_T, where K varies relatively slowly), whereas for earlier studies [5, 19] $K_{peak} \sim K_{baseline}$, further highlighting that memory formation is much stronger in our case. Additionally, I find that once the system is trained at a particular γ_T, any memory of $\gamma < \gamma_T$ gets erased (Fig. 4.4). I discuss the possibility of encoding multiple memories in our system later in this chapter and in more detail in Chapter-5. I also find that the signature of encoded memory stays essentially the same, even when the readout is taken after 1000 s, implying that the relaxation of the structures

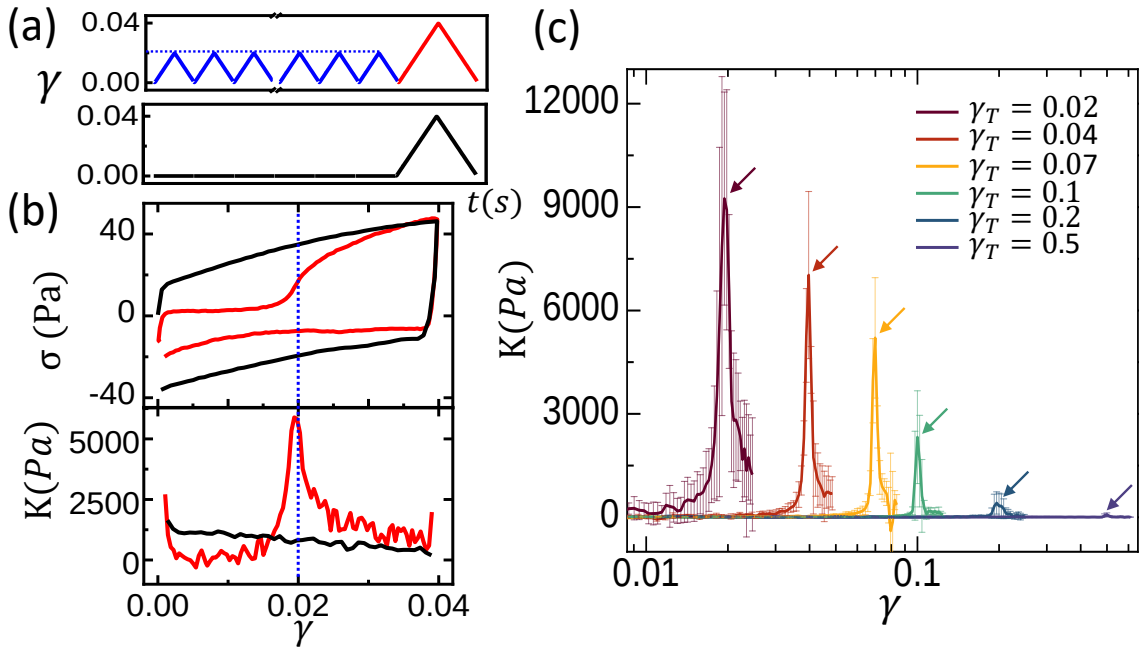

Figure 4.3: (a) Top: Training and readout protocol with $\gamma_T = 0.02$ and $\gamma_R = 0.04$, respectively. Bottom: Protocol of applying a single readout pulse ($\gamma_R = 0.04$) without any training. (b) Top panel: Stress (σ) vs strain(γ) plots obtained from the readouts shown in (a) with training (in red) and without training (in black). Bottom panel: The corresponding differential shear moduli $K = \frac{d\sigma}{d\gamma}$ vs. γ with same colour coding as the top panel. (c) Variation of K vs. γ for a wide range of γ_T values as indicated in the legend with arrows indicating the position of the peak of K for different γ_T values. Each data set is averaged over at least 4 independent measurements. Error bars are the standard deviations.

supporting the memory is very slow. (see Appendix of this Chapter).

To inspect the effect of training amplitude on the strength of memory formation, I encode and readout the memory for a range of γ_T values. For each γ_T I use a fresh loading of the sample. In Fig. 4.3(c), I plot average K vs. γ for various γ_T values. I find a steady drop in the strength of the memory (quantified by the peak values of K) as γ_T increases. In fact, beyond $\gamma_T = 0.1$, K_{peak} is significantly lower, albeit still present. This value of γ_T is close to the fluidization/yielding onset of the system (Fig. 4.2). Thus, in contrast to 2-D soft glassy system [5], I do not find any enhancement of memory effect near the yield point.

So far I have established that the encoded memory gets reflected as a large change in the value of differential shear modulus of the system. In order to understand the mechanism behind this striking behaviour, I perform in-situ optical imaging (in the flow(X)-gradient(Y) plane). Details of the set-up can be found in section 2.2.1 and also in [20]. A

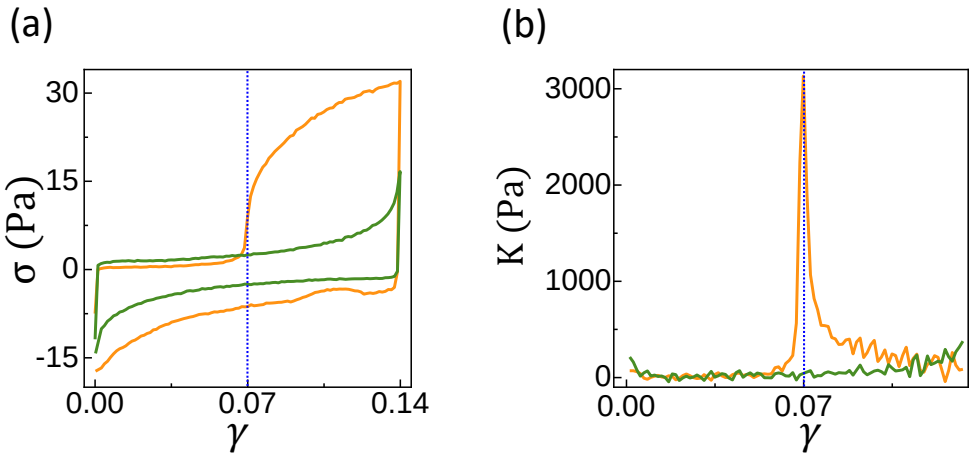

Figure 4.4: The system is first trained at strain amplitude $\gamma_T = 0.07$. Immediately after this, the system is continued to be trained at $\gamma_T = 0.14$ for a total of N = 20 cycles. I plot the intra-cycle stress (σ) vs. strain (γ) obtained for N = 1 (orange curve) and N = 20 (green curve) for $\gamma_T = 0.14$ in (a). Corresponding K vs. γ plots are shown in (b). I see that while N = 1 shows a signature of memory at $\gamma_T = 0.07$, there is no such signature for N = 20. Thus, the memory of the lower $\gamma_T = 0.07$ gets completely erased within just 20 cycles of training at the larger strain $\gamma_T = 0.14$. Dashed vertical lines indicate $\gamma_T = 0.07$.

typical image is shown in Fig. 4.5(a) where the bright speckles correspond to CS particles which protrude out of the suspension-air interface. Internal connectivity of the fractal network, giving rise to solid-like yield stress in the system, stabilizes such protruding particles against the stress due to surface tension. I map out the velocity profile across the shear-gap using Particle Imaging Velocimetry (PIV) during the training and readout experiments as shown in Fig. 4.6. I observe that except for narrow regions of high shear rate close to the shearing boundaries, the bulk of the sample moves like a solid plug with negligible velocity gradient. I use Kymographs to map out the space-time variation of the speckle distribution at different locations inside the sample acquired during training and readout experiments. For this, I first consider a series of images equally spaced in time. Then I choose a fixed line segment along the direction of shear (X-direction) (see Fig. 4.5). The velocity gradient is along the Y-direction. Thus the segment represents a fixed value of y = y_0. The 2-D representation of the intensity distribution $I(x, y_0, t)$ of the line segment as a function of space and time gives the Kymograph. Interestingly, if a relatively bright speckle (representing a protruding particle at the suspension-air interface) moves along the chosen fixed line under shear and the line always contains the position of the speckle , then the Kymograph can directly represent the particle trajectory (Fig. 4.7).

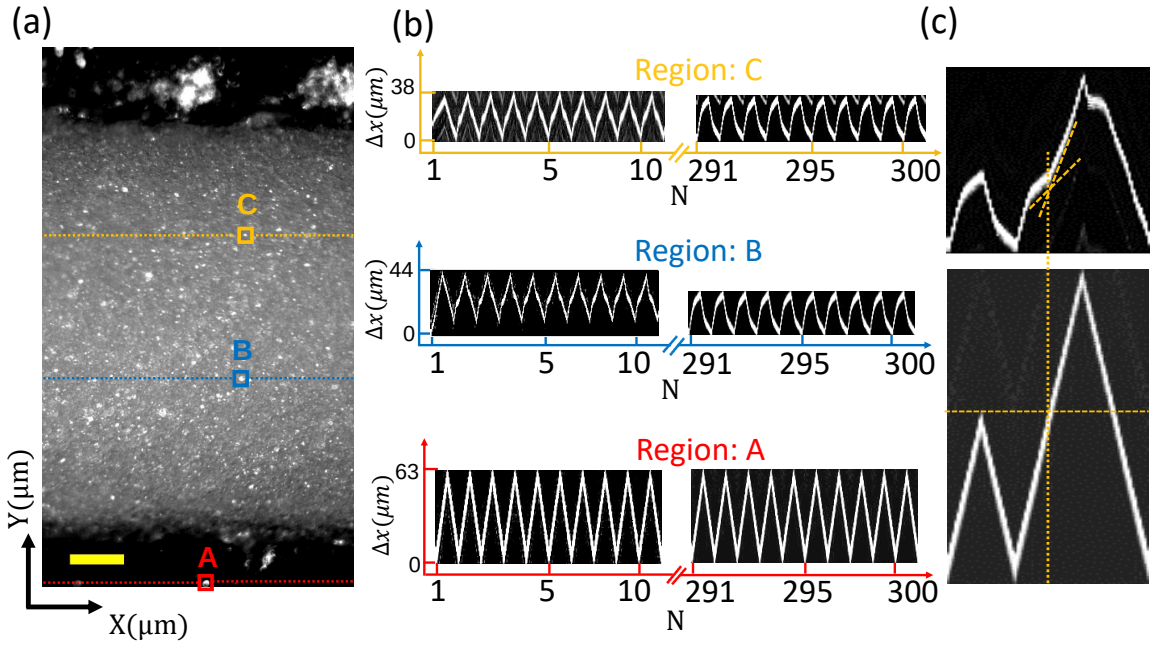

Figure 4.5: (a) A typical boundary image of the sample with the X-axis along the direction of flow and Y-axis along the gradient. Three points: A (on the plate), B and C (inside the bulk of the sample) indicated by boxes denote the location of the bright speckles for Kymograph analysis. The displacements of the bright speckles during the course of training are contained in the corresponding dotted lines. Corresponding Kymographs (for $\gamma_T = 0.07$) are shown in panel (b) for the first 10 (N: 1 - 10) and last 10 (N: 291 - 300) training cycles, as indicated. (c) Kymographs corresponding to the last training (N = 300) and the readout cycle for the point A (bottom panel) and B (top panel). Dashed lines indicate a change in slope of the particle trajectory as the readout strain crosses γ_T. Scale bar in (a) denotes 100 μm.

I consider Kymographs at three different locations: 1. on the moving plate (Region A), 2. inside the solid-like region close to the moving plate (Region B), and 3. inside the solid-like region close to the static cone (Region C) (see Fig. 4.5(a)). All these regions contain atleast one dominant bright speckle (indicated in the figure by square boxes) whose trajectory can be tracked during the training and readout. I show in Fig. 4.5(b) the Kymographs corresponding to these regions for the first 10 (N = 1 - 10) and last 10 (N = 291-300) training cycles. I find that the trajectory obtained for Region A (Fig. 4.5(b), bottom panel) precisely mimics the motion of the shearing plate during training. The self-similarity of the waveform establishes the robustness of the input shear. Interestingly, Kymographs for Region 2 and 3 show more complex displacement waveforms involving a gradual evolution in both amplitude and shape before reaching a steady state during the course of training. However, except for the first cycle (involving start-up transients)

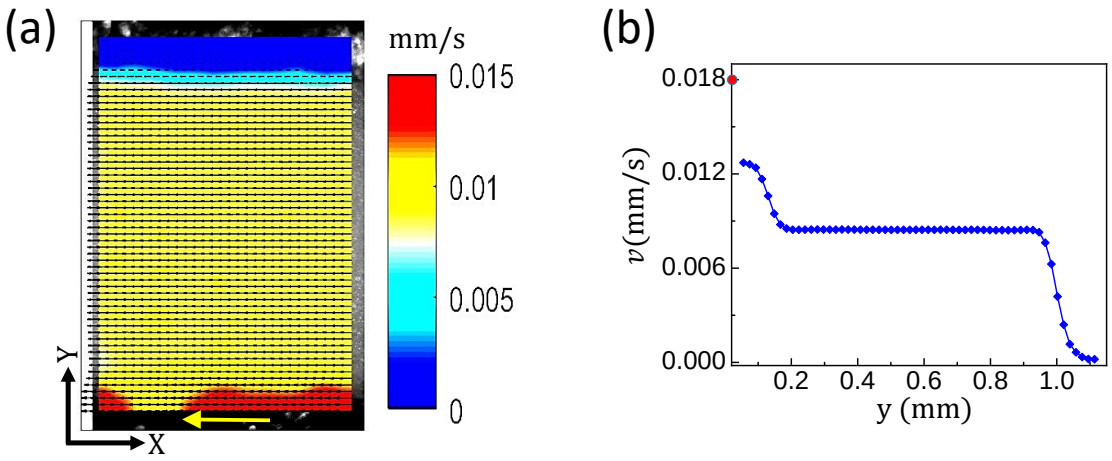

Figure 4.6: (a) A typical boundary image with superposed vector profile obtained from Particle Imaging Velocimetry (PIV) analysis (Materials and methods). (b) Velocity profile across the shear gap corresponding to the vector image shown in (a). Here, the velocity for each y value represents the average over all the velocity vectors at the same y coordinate but, varying x coordinates. It is clear from the vector representation and the velocity profile that the system has high shear rate bands near the shearing boundaries, while the bulk of the sample is moving like a solid plug with almost a constant velocity. The red dot on the velocity axis indicates the calculated plate velocity.

waveform in these regions remains very similar, further confirming the solid plug-like motion of the bulk of the sample.

Interestingly, the displacement waveform inside the solid-like region of the sample indicates a complex coupling-decoupling dynamics between the moving plate and the bulk of the sample through the high shear rate bands near the boundaries. Clearly such dynamics is developed through training as it is absent in the beginning (left panels of Fig. 4.5(b)). In the steady state, particle trajectories in the solid-like region of the sample settle down to a waveform which is very different from the input, demonstrating a slowing down of the bulk as the intra-cycle input strain (γ) approaches the training amplitude (γ_T). Now, I take a look at the readout by plotting Kymographs corresponding to the last training cycle (N = 300) and the readout cycle in Fig. 4.5(c). For clarity, I show the data only for Region A (bottom panel) and Region B (top panel) with expanded views. I find that the speckle-displacement during readout follows the last training cycle up to $\gamma = \gamma_T$. However, as γ crosses γ_T, there is a sudden increase in the slope of the trajectory (marked by dashed lines in Fig. 4.5(c), top panel). Similar change in slope is also observed for other speckle trajectories inside the solid-like region (Fig. 4.7). This implies that beyond γ_T, there is a sudden buildup of coupling between the solid-like region and the moving

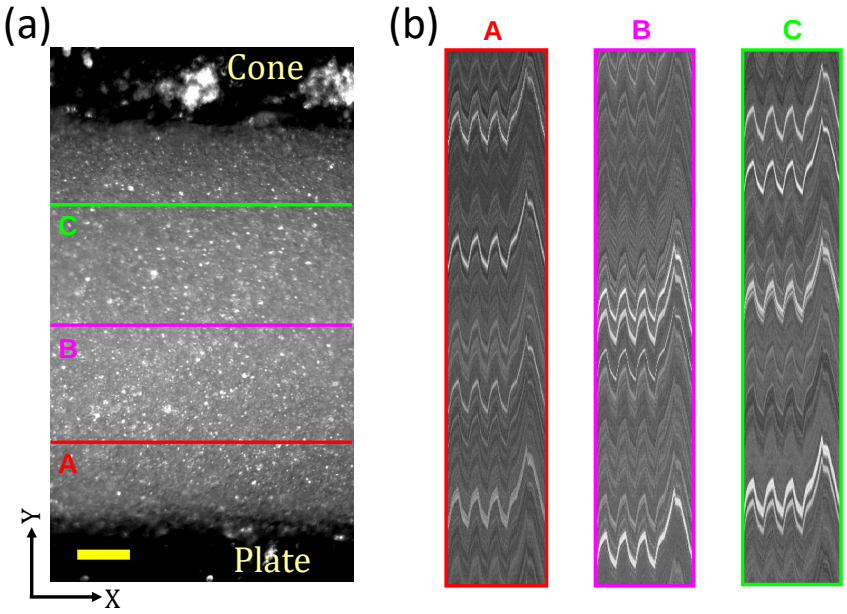

Figure 4.7: (a) A typical boundary image of the sample with lines depicting different regions inside the sample at varying distance from the moving plate. The scale bar represents 100 μm. (b) Corresponding Kymographs taken along the lines shown in (a). For clarity, only the last three training cycles (N: 298-300) and the readout is considered for each region. The multiple particle trajectories depicted in each Kymograph are the displacement waveforms for various speckles on the same line. The similarity of the waveforms, as well as, the discontinuity due to encoded memory indicates the solid plug-like motion of the bulk of the sample. Here $\gamma_T = 0.07$.

plate. This sudden coupling will lead to an abrupt increase in velocity of a large number of particles, which can explain the origin of the sharp peak of K around $\gamma = \gamma_T$. Such abrupt increase in velocity of the solid-like region inside the bulk of the sample also reflects in the velocity profile obtained from the PIV analysis (Fig. 4.8). Difference images constructed through stroboscopic sampling indicate a reversible to irreversible transition (RIT) in the sample beyond γ_T (Fig. 4.9) similar to earlier studies [3, 5, 19].

Next, I address the role of inter-particle adhesive interaction on the strong memory formation in our system. In the previous chapter, I reported that addition of a small amount of surfactant to the Cornstarch-Paraffin oil system can reduce the adhesive interaction between the particles as quantified by the systematic change in jamming volume fraction [20]. With sufficient amount of surfactant, the system completely transforms into a steric-repulsive one. Physically, as I increase the surfactant concentration (c), the large fractal clusters initially stabilized by inter-particle adhesion gradually disintegrate and finally form a well dispersed suspension as shown in the schematic Fig. 4.10(a). I prepare

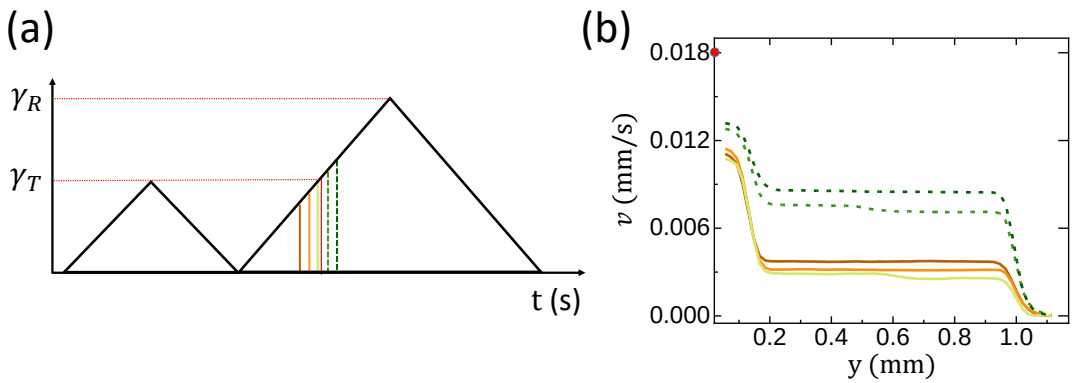

Figure 4.8: (a) A schematic showing the last training cycle (N = 300) and the readout cycle with horizontal lines marking the training strain amplitude γ_T and the readout strain amplitude γ_R. Here $\gamma_T = 0.07$ and $\gamma_R = 0.14$. Vertical lines indicate different strain values (both above and below γ_T) during the readout for which the instantaneous velocity profiles are shown in panel (b). (b) Corresponding velocity profiles across the shear gap obtained through PIV analysis (see Fig. 4.6). Solid lines are profiles just below γ_T and dashed lines are those just above γ_T. The colour coding is same as that in (a). I see that as the readout strain just crosses γ_T, the velocity of the solid plug-like region suddenly increases. This indicates a sudden buildup of contact between the solid plug and the moving plate. The red dot on the velocity axis indicates the calculated plate velocity.

samples with increasing c and subject them to the similar training and readout protocols mentioned earlier for different γ_T values. In Fig. 4.10(b), I plot the average peak values of K for different γ_T values obtained from the readouts for a range of c values. I see that the strength of memory (K_{peak}) decreases with increasing c and the system loses ability to form strong memory beyond sufficiently high concentration of surfactant ($c \geq 0.3$ %). However, even at the highest surfactant concentration, the memory signature is not totally absent, as can be seen from the log-log plot (inset of Fig. 4.10(b)) and also Fig. 4.11.

I find that for the same range of c, the training induced strain stiffening also becomes significantly weaker (Fig. 4.12). Thus, the memory formation in our system is intimately related to the strain stiffening response of the system. From the Kymograph analysis I do not find any discontinuity in the particle trajectory across γ_T in the readout for sufficiently high surfactant concentrations (Fig. 4.13).

Lastly, I address the possibility of encoding multiple memories in our system. As mentioned earlier, if the system is trained at γ_T, it erases all memory of $\gamma < \gamma_T$. Interestingly, I find that if the sample is trained with the smaller strain amplitude just before

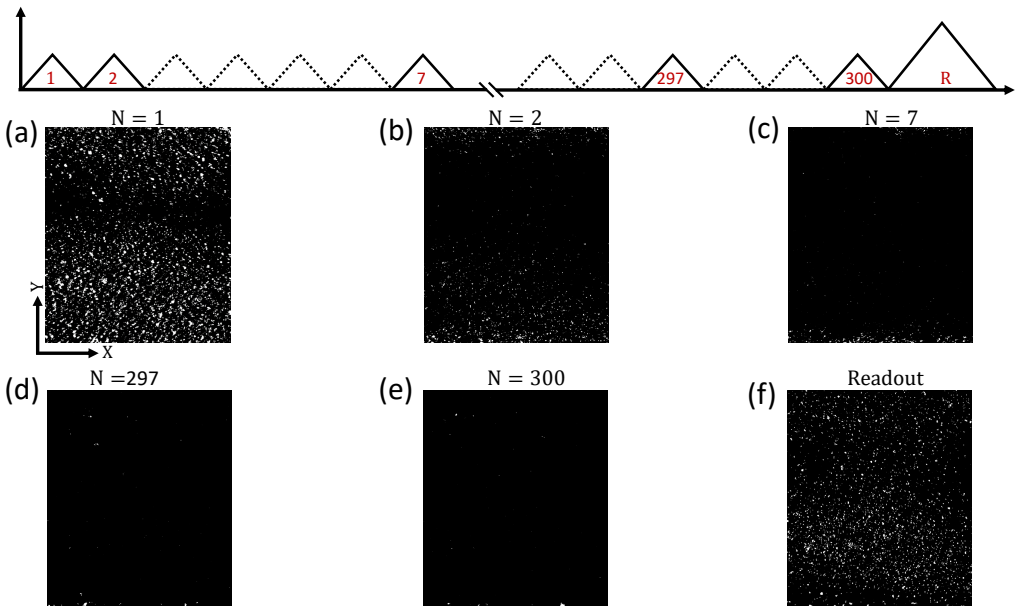

Figure 4.9: Stroboscopic difference between images of the system taken at the start and at the end of each cycle during the training and readout as shown in the schematic in the top panel. All images are cropped till the edges (including roughness) of the cone and plate. (a)-(e) Stroboscopic difference for different cycle number (N) indicated in the figure obtained during training. The bright spots in the difference images indicate the location of irreversible particle displacements that take place over the course of the N^{th} cycle. I see that the particle rearrangements systematically drop with increasing number of training cycles and become almost negligible near the end of the training sequence indicating essentially reversible particle trajectories. Panel (f) represents the stroboscopic image corresponding to readout. The high intensity spots in (f) indicates the irreversibility of the particle trajectories. Clearly, a reversible to irreversible transition (RIT) happens as the system crosses γ_T. The data shown here is for $\gamma_T = 0.07$ and $\gamma_R = 0.14$.

the readout, it can retain the memory of the smaller γ_T and more than one memory can be encoded, as has also been reported earlier for other systems [4, 19]. I use the following protocol: I apply 1 cycle of the larger training strain amplitude ($\gamma_{T2} = 0.04$) followed by 20 cycles of the smaller training strain amplitude ($\gamma_{T1} = 0.02$). This whole sequence is repeated 15 times and then I apply a readout strain $\gamma_R = 0.06$. The stress (σ) vs. strain (γ) plot for the readout shows sharp changes at $\gamma = 0.02$ and 0.04 (Fig. 4.14(a)), giving two prominent peaks for the differential shear modulus K (Fig. 4.14(b)). This indicates that the system has the ability to encode memories of more than one strain amplitude under a suitable training protocol.

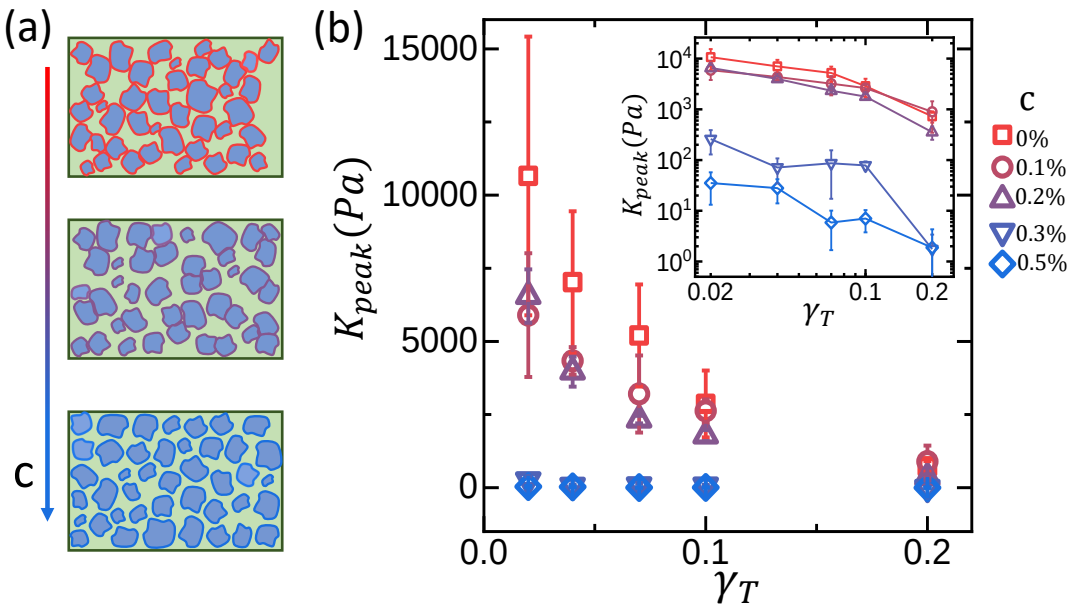

Figure 4.10: (a) Schematic indicating the gradual dispersion of fractal clusters with increasing surfactant concentration (c). For a given sample, c denotes the mass fraction of surfactant w.r.t. Cornstarch particles. (b) Variation of the peak values of differential shear modulus K_{peak} as a function of training strain amplitude γ_T for a range of c values indicated. Each data set is averaged over at least 3 independent measurements with the error bars denoting the standard deviations. Inset shows a log-log plot of the same.

4.4 Conclusion

I report strong memory formation in an adhesive dense particulate suspension under cyclic shear. The differential shear modulus of the bulk system shows a huge enhancement near the training strain amplitude (γ_T). A possible explanation for such striking effect is the following: in the presence of adhesion, the fractal particle clusters can form strand-like connected structures. Under cyclic shear deformations, such structures can reorganize and develop a slack up to γ_T. The adhesive interaction maintains the contact between the particles in these loose strand-like structures for strain values $\gamma < \gamma_T$. Similar strand plasticity has been reported in colloidal gels under cyclic shear [21]. For our case, such reorganization dynamics predominantly takes place in the high shear rate bands close to the shearing boundaries. Due to the slack in the particle strands, the plate can easily move without significantly disturbing the solid-like bulk region inside the sample for $\gamma < \gamma_T$. This gives rise to an apparent decoupling between the plate and the bulk sample in the steady state. However, when γ crosses γ_T during the readout, the loose strands suddenly get stretched and the coupling between the moving plate and the solid-like

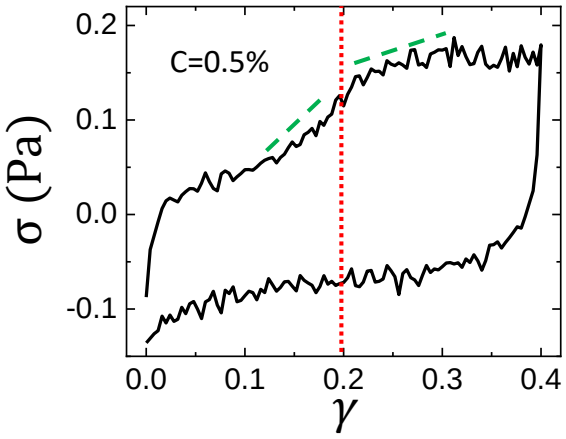

Figure 4.11: Readout Lissajous plot for volume fraction $\phi = 0.4$ with surfactant concentration c = 0.5% as indicated in the figure. Dashed vertical line indicates the training strain amplitude. Green dashed lines along the curve indicate the change in slope across the training strain amplitude, showing that there is still a weak signature of memory even in the limit of negligible adhesion in the system. However, from the inset of Fig. 4.10(b), I see that the mean value of K_{peak} is very small with large error bars. This is because in the limit of low adhesion, the absolute values of stress are quite low. This makes the the differential shear modulus data quite noisy.

region builds up. This results in a strong stress response. Interestingly, such a picture can also shed some light on the reduction in the strength of memory with increasing γ_T: for small γ_T values, a large number of clusters can contribute to strand formation, however for large γ_T values, many small clusters can get completely disintegrated and only large connected structures will contribute. Although, at present I cannot directly visualize the strand dynamics, the connection between the strand formation/plasticity and the observed memory effect is further supported by the role of adhesive interaction in the system (also see Appendix of this chapter). Once the inter-particle adhesion gets sufficiently weakened by addition of surfactant, the strand formation is no longer possible, as a result the memory effect gets diminished. This weaker memory, in principle, is similar to that observed earlier in dilute non-Brownian suspensions [19]. However, further work is needed to understand the exact correspondence.

Memory effect reported here is reminiscent of similar phenomena in transiently cross-linked biopolymer networks [17] and Mullin's effect in filled-polymeric systems [22]. Our system also shows a connection between the memory formation and reversible-irreversible transition like many repulsive particulate systems. Thus, adhesive particulate system can be thought of as an intermediate between repulsive dense suspensions and polymeric

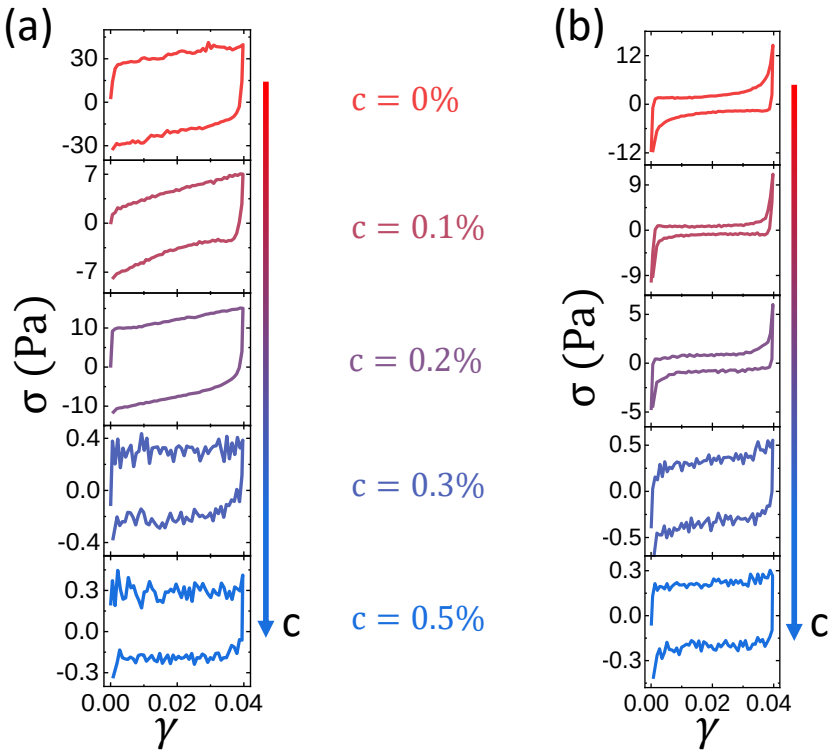

Figure 4.12: (a) Intra-cycle stress (σ) vs. strain (γ) corresponding to the first (N = 1, panel(a)) and the last training cycle (N = 300, panel (b)) for samples with different concentrations of surfactant (c) as indicated. The training induced strain stiffening behaviour gradually disappears with increasing surfactant concentration.

materials. Remarkably, our system presents a distinct advantage: since the particles are very robust and the adhesive particle-bonds are reversible, training and readout for a wide range of strain values does not cause any permanent damage to the system. The sample can be reloaded and reprogrammed arbitrarily. On the other hand, polymeric materials are prone to permanent damage due to breakage of filaments or chemical bonds. Interestingly, the strand picture together with the reversibility of adhesive bonds can explain the origin of multiple memories in our case. After encoding a memory at a smaller strain amplitude, application of a larger training strain can destroy the strands supporting the memory at smaller amplitude. However, after this, if the system is again trained at the smaller amplitude, the reversibility of the adhesive bonds ensures that some local connectivity can build up once more (Fig. 4.15), thus re-encoding the memory of smaller amplitude.

Due to the opaque nature of the particles, I can only probe the particle-dynamics on the sample surface. However, as our system is very dense (Fig. 4.5(a)), it is hard to directly probe training induced changes in the nodes or connectivity between the particles

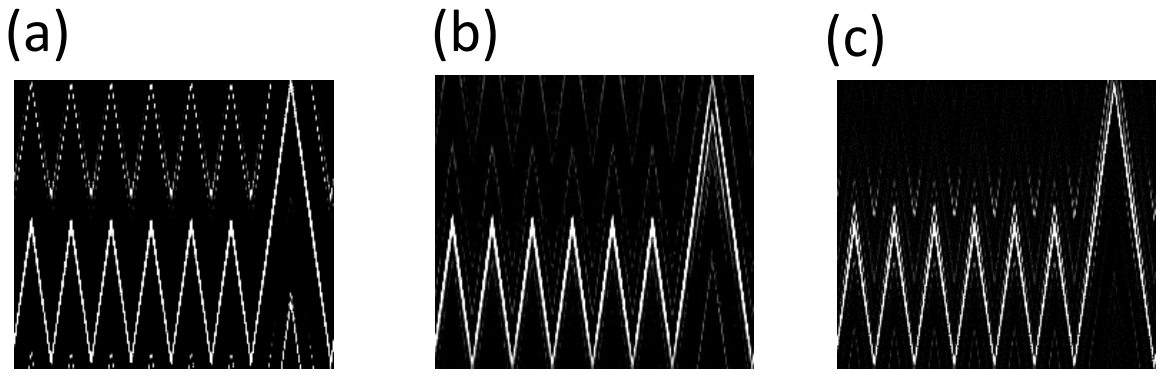

Figure 4.13: Kymographs of the last few training cycles (N: 295-300) and the readout cycle for the samples with a surfactant concentration $c = 0.5\%$. Kymographs corresponding to a point on the moving plate (panel (a)), at a point inside the bulk but near the moving plate (panel (b)), at a point inside the bulk but near to the stationary cone (panel (c)). I see that there is no kink in the particle displacement waveform as the readout strain crosses the training strain amplitude (compare with Fig. 4.5(c)). As already established, the memory encoded in the system for this concentration of surfactant is extremely weak. So, it is not surprising that we do not see any signature of it in the kymograph data.Here $\gamma_T = 0.07$, and $\gamma_R = 0.14$.

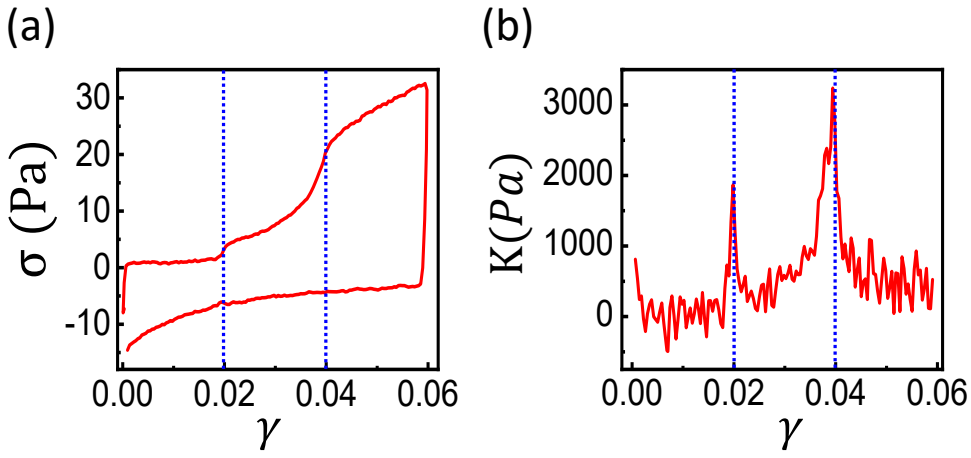

Figure 4.14: (a) Intra-cycle stress (σ) vs strain (γ) obtained from the readout for a sample trained at $\gamma_{T1} = 0.02$ and $\gamma_{T2} = 0.04$. (b) Corresponding K vs γ showing the signature of multiple memory formation.

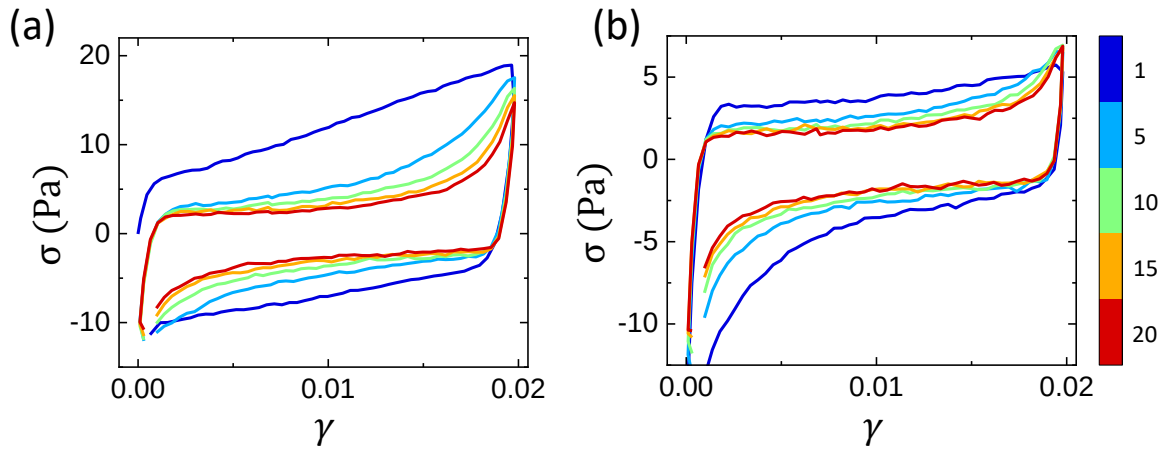

Figure 4.15: (a) The development of strain stiffening with repeated application of strain amplitude γ_{T1}=0.02 for N=20 cycles. The curves are plotted at discrete values of N as indicated by the colorbar. (b) Following the 20 cycles shown in (a), I apply one cycle of γ_{T2}=0.04. After this, I apply the triangular wave with γ_{T1}=0.02 for 20 cycles once again. I see that while the initial curves show a very plastic behavior, by the 20^{th} cycle, the system has developed strain stiffening once again. On applying the larger amplitude of γ_{T2}=0.04, the encoded memory of γ_{T1} gets destroyed as evidenced by the initial few curves of (b). However, on repeatedly applying γ_{T1}, the local structures are re-established and the system is able to strain stiffen at this amplitude once again, thus re-encoding the memory at γ_{T1}. This is possible because our system has inter-particle adhesive contacts that are physical bonds between the particles and thus, are reversible under breakage.

using boundary imaging alone. Mapping out the system dynamics in 3-D using optical/acoustic techniques remains a future challenge. Further theoretical insights regarding the mechanism of such strong memory effect in adhesive systems, including the formation of multiple memories can open up new avenues to explore. Our study can have important implications in designing programmable materials.

4.5 Appendix

4.5.1 Appendix 1: Effect of waiting time on the encoded memory in the system.

An important aspect of memory formation is the effect of the system's relaxation on the encoded memory signature in the system. To check that, I left the system undisturbed, after training, for different waiting times before taking readouts to see whether the re-

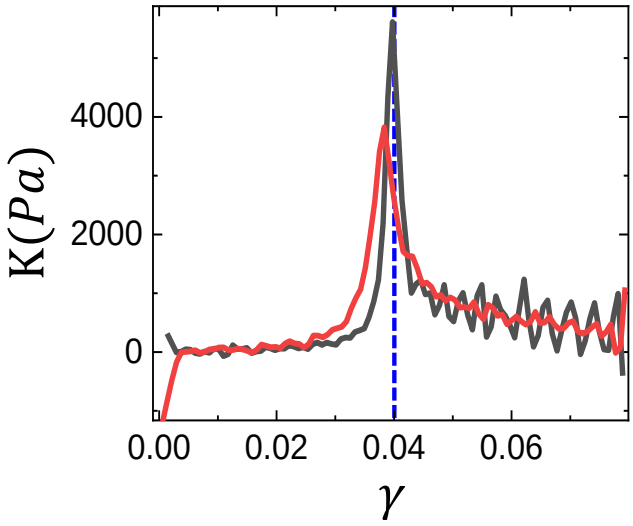

Figure 4.16: Effect of waiting time on the memory signature (black curve) when the system is left undisturbed for 1000 seconds after training, shown by the red curve. The system is trained at $\gamma_T = 0.04$ as indicated by the vertical dashed line.

laxation of the system affects the encoded memory. So far, I have only probed for a maximum of 1000 s waiting time, the data for which is shown in the Fig. 4.16. I find that the encoded memory signature is still significant after waiting for 1000s, albeit with a slight shift in the strain value corresponding to the peak of the differential shear modulus (K). This implies that the timescale for any relaxation of the particle networks is much longer. In our case, the timescale set by the shear rate of 0.01 s^{-1} (that I have used for our experiments) is 100s ($\frac{1}{\dot{\gamma}}$), which is small enough to prevent any significant relaxation of the contact networks and affect the memory formation in the system.

4.5.2 Appendix 2: Imaging of shear induced aggregation in the system

As mentioned in the conclusion, direct observation inside the bulk of the system is difficult, given the optical opacity of the system. Here I show an alternate imaging of this system using transparent geometry. The setup consists of two glass plates (PP43, Anton Paar) with the sample loaded between them. Using the same camera and objective as described in section 2.2.1 with a prism, I image the system from the bottom as depicted by the schematic in Fig. 4.17. The system is illuminated by a light source from the top and the transmitted light is captured by the imaging setup (see schematic).

I prepare the Cornstarch-Paraffin oil suspension at a volume fraction $\phi = 0.2$ and

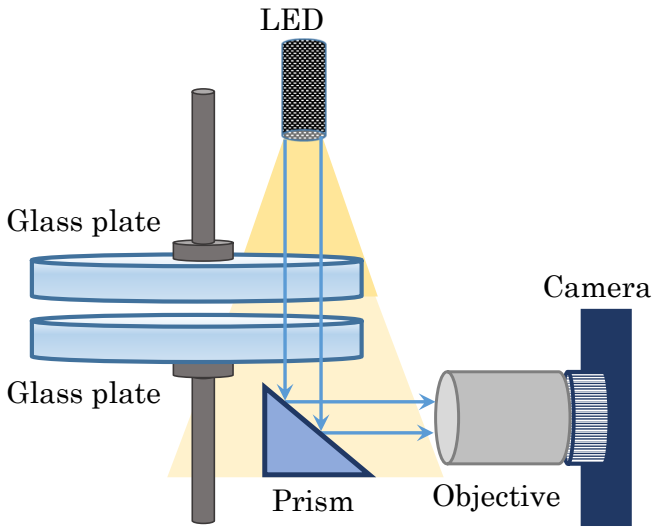

Figure 4.17: Schematic of the setup for transparent plate imaging of Cornstarch (CS) particles dispersed in Paraffin oil under applied shear.

apply an absolute strain of 2 repeatedly for 50 cycles using the triangular wave strain deformation described in the Results and discussion of this chapter. In Fig. 4.18, I show images of the system taken after a cycle. Top row indicates images taken in the beginning cycles while bottom row has images taken towards the end of the training sequence (as indicated in the image). While the particle distribution is roughly homogeneous in the beginning, I observe porosity buildup (indicated by the gaps and aggregates in the bottom row images) with repeated shearing of the system. I also imaged the system under static conditions (no shear) and as expected, I did not observe any aggregation, thus confirming that the observed structures/aggregates are shear-induced.

Bibliography

[1] Sebanti Chattopadhyay and Sayantan Majumdar. Inter-particle adhesion induced strong mechanical memory in a dense granular suspension. *J. Chem. Phys.*, 156(24), June 2022.

[2] Davide Fiocco, Giuseppe Foffi, and Srikanth Sastry. Oscillatory athermal quasistatic deformation of a model glass. *Phys. Rev. E*, 88(2):020301, Aug 2013.

[3] Davide Fiocco, Giuseppe Foffi, and Srikanth Sastry. Encoding of Memory in Sheared Amorphous Solids. *Phys. Rev. Lett.*, 112(2):025702, Jan 2014.

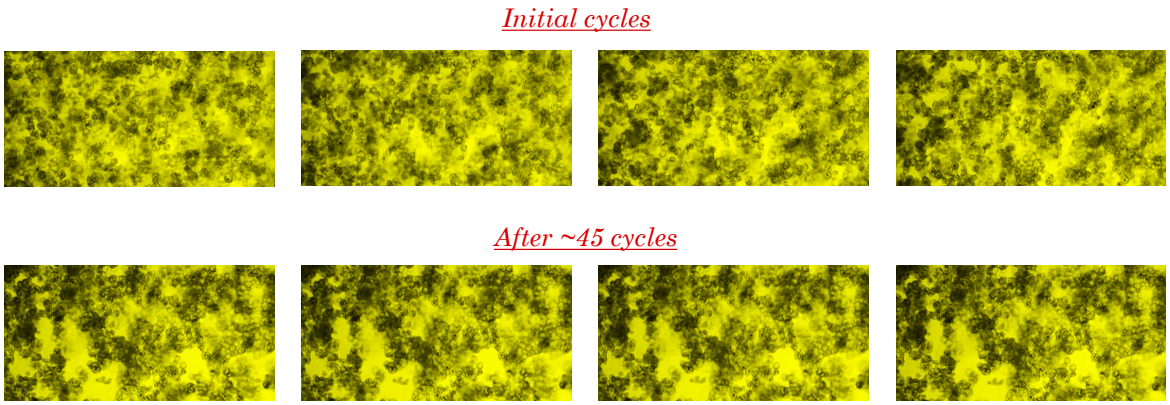

Figure 4.18: Figure shows images of the Cornstarch-Paraffin oil system captured using the transparent geometry under shear. Images shown are captured at the end of a cycle. Top panel shows the system during the initial cycles of deformation while the bottom panel shows the same for the last few training cycles. I observe formation of porous structures with repeated application of shear.

[4] Nathan C Keim, Jacob Hass, Brian Kroger, and Devin Wieker. Global memory from local hysteresis in an amorphous solid. *Physical Review Research*, 2(1):012004, 2020.

[5] Srimayee Mukherji, Neelima Kandula, A. K. Sood, and Rajesh Ganapathy. Strength of Mechanical Memories is Maximal at the Yield Point of a Soft Glass. *Phys. Rev. Lett.*, 122(15):158001, Apr 2019.

[6] Michael L Falk and James S Langer. Deformation and failure of amorphous, solidlike materials. *Annu. Rev. Condens. Matter Phys.*, 2(1):353–373, 2011.

[7] Ekin Dogus Cubuk, RJS Ivancic, Samuel S Schoenholz, DJ Strickland, Anindita Basu, ZS Davidson, Julien Fontaine, Jyo Lyn Hor, Y-R Huang, Y Jiang, et al. Structure-property relationships from universal signatures of plasticity in disordered solids. *Science*, 358(6366):1033–1037, 2017.

[8] Monoj Adhikari and Srikanth Sastry. Memory formation in cyclically deformed amorphous solids and sphere assemblies. *Eur. Phys. J. E*, 41(9):1–17, Sep 2018.

[9] Muhittin Mungan, Srikanth Sastry, Karin Dahmen, and Ido Regev. Networks and hierarchies: How amorphous materials learn to remember. *Physical Review Letters*, 123(17):178002, 2019.

[10] Ido Regev, Turab Lookman, and Charles Reichhardt. Onset of irreversibility and chaos in amorphous solids under periodic shear. *Physical Review E*, 88(6):062401, 2013.

[11] Nathan C Keim and Joseph D Paulsen. Multiperiodic orbits from interacting soft spots in cyclically sheared amorphous solids. *Science Advances*, 7(33):eabg7685, 2021.

[12] John R Royer and Paul M Chaikin. Precisely cyclic sand: Self-organization of periodically sheared frictional grains. *Proceedings of the National Academy of Sciences*, 112(1):49–53, 2015.

[13] Nathan C Keim and Paulo E Arratia. Yielding and microstructure in a 2d jammed material under shear deformation. *Soft Matter*, 9(27):6222–6225, 2013.

[14] Nathan C Keim and Paulo E Arratia. Mechanical and microscopic properties of the reversible plastic regime in a 2d jammed material. *Physical Review Letters*, 112(2):028302, 2014.

[15] K Hima Nagamanasa, Shreyas Gokhale, AK Sood, and Rajesh Ganapathy. Experimental signatures of a nonequilibrium phase transition governing the yielding of a soft glass. *Physical Review E*, 89(6):062308, 2014.

[16] Eric M. Schwen, Meera Ramaswamy, Chieh-Min Cheng, Linda Jan, and Itai Cohen. Embedding orthogonal memories in a colloidal gel through oscillatory shear. *Soft Matter*, 16(15):3746–3752, Apr 2020.

[17] KM Schmoller, P Fernandez, RC Arevalo, DL Blair, and AR Bausch. Cyclic hardening in bundled actin networks. *Nature Communications*, 1(1):1–8, 2010.

[18] Sayantan Majumdar, Louis C. Foucard, Alex J. Levine, and Margaret L. Gardel. Mechanical hysteresis in actin networks. *Soft Matter*, 14(11):2052–2058, Mar 2018.

[19] Joseph D. Paulsen, Nathan C. Keim, and Sidney R. Nagel. Multiple Transient Memories in Experiments on Sheared Non-Brownian Suspensions. *Phys. Rev. Lett.*, 113(6):068301, Aug 2014.

[20] Sebanti Chattopadhyay, Sharadhi Nagaraja, and Sayantan Majumdar. Effect of adhesive interaction on strain stiffening and dissipation in granular gels undergoing yielding. *Commun. Phys.*, 5(126):1–10, May 2022.

[21] Jan Maarten van Doorn, Joanne E. Verweij, Joris Sprakel, and Jasper van der Gucht. Strand Plasticity Governs Fatigue in Colloidal Gels. *Phys. Rev. Lett.*, 120(20):208005, May 2018.

[22] Leonard Mullins. Effect of stretching on the properties of rubber. *Rubber chemistry and technology*, 21(2):281–300, 1948.

CHAPTER

FIVE

Perturbation induced memory shifting in a disordered solid

5.1 Introduction

In the previous chapter (Chapter-4), I have shown that granular gels formed by dispersing Cornstarch (CS) particles in paraffin oil (PO) can retain memories of repeated cyclic perturbation. More importantly, the bulk mechanical properties of this system show clear signatures of such encoded memory. At the end of the chapter, I showed that this system can also encode more than one memory, which can be read out as distinct mechanical signatures. In this chapter, I explore this multiple memory formation in a more systematic manner.

As already mentioned, memory formation has been studied in many soft matter systems. While the encoding of a memory is a result of the system's self organization into a reversible steady state, formation of multiple memories often has a more intricate mechanism at play. For instance, in dilute suspensions, where under training the system can evolve to a collision-less absorbing state [1, 2, 3, 4, 5] (also see Chapter-1 section 1.4.3), multiple memories can be encoded only transiently [3, 4, 5, 6]. At long times, the system retains only the largest applied amplitude, implying an ordering of states in these systems. Interestingly, the presence of a persistent noise in the system can stabilise the multiple memories as shown by both simulations and experiments. On the other hand, disordered solids, with their non-trivial energy landscape and enduring particle contacts, can encode more than one memory even in the absence of external noise [7, 8, 9, 10, 11]. Such distinction in the formation of multiple memories essentially stems from the attributes of the training induced reversible states.

Current research on disordered solids and glassy systems is strongly focusing on reconciling the aspects of multiple memory formation in these systems with return point memory (RPM) of magnetic systems [11, 12, 13, 14, 15]. Such efforts can help in the unification of memory retention across a wide range of systems. However many of these dense systems are often limited by the accessibility of the micro-structures, making it a challenge to understand the effects of encoding more than one memory. In this regard, having bulk signatures of encoded memories can be useful [16, 17].

Protocols to encode multiple memories employ a combination of the two (or more) strain amplitudes applied repeatedly, often with variations such as a protocol bias towards smaller amplitude to ensure its survival (for instance, applying more cycles of the smaller amplitudes for every cycle of the larger amplitude), applying the smaller amplitude last before readout, etc [3, 4, 5, 10, 11, 16]. In case of both dilute suspensions as well as disordered solids, applying a larger amplitude destroys the memory of a smaller amplitude.

Additionally, for dilute suspensions, once the system reaches the absorbing state for a particular amplitude, applying a smaller strain will not have any effect. Interestingly, disordered solids exhibit periodic rearrangements of particles in the reversible state and ordering of states does not hold for these systems [10, 16]. In this case, after the formation of a reversible state at an amplitude, the effects of applying a smaller amplitude is not clear.

Here, I explore multiple memory formation in an adhesive granular gel. I first encode the memory of an amplitude (primary memory) in the system and then subject it to training at a smaller amplitude. I find that the process of encoding the second memory destroys the memory signature at the first amplitude. Interestingly, this is the consequence of a memory shifting phenomena: the position of the primary memory gradually shifts towards the second memory. Additionally, due to the shifted position of the primary memory, the system develops a phantom memory that was not encoded into it. I also find that the memory shifting becomes more dramatic when trained at a higher shear rate. I use energy dissipation analysis to propose a possible mechanism for the observed phenomena.

5.2 Materials and Methods

Dense suspensions are prepared by dispersing Cornstarch (CS) particles (Sigma Aldrich) in Paraffin oil (SDFCL) at a volume fraction $\phi = 0.4$ for all our measurements. Details of the sample preparation technique are same as Chapter-4 (also given in section 2.3.1). Experiments are performed on a stress controlled rheometer (MCR-702, Anton Paar Austria) using a cone and plate geometry in the separate motor-transducer mode. Both the cone and the plate have a diameter of 50 mm and are sandblasted with a cone angle of $\approx 2\,\text{deg}$ (see section 2.2.1 and [18] for more details).

5.3 Results and Discussion

I use a triangular wave shear deformation protocol [16] to train the system. I first apply $N_T = 200$ cycles of the triangular wave with an amplitude of γ_T, thus encoding a memory at γ_T. Next, I apply N cycles of the same deformation but with an amplitude of $\gamma_N < \gamma_T$. In the previous chapter (Chapter-4), I have already shown that applying a strain of $\gamma > \gamma_T$ immediately erases the encoded memory signature of γ_T (see [16] and also the Appendix of this Chapter). In this chapter, I apply only smaller amplitudes to the system in order

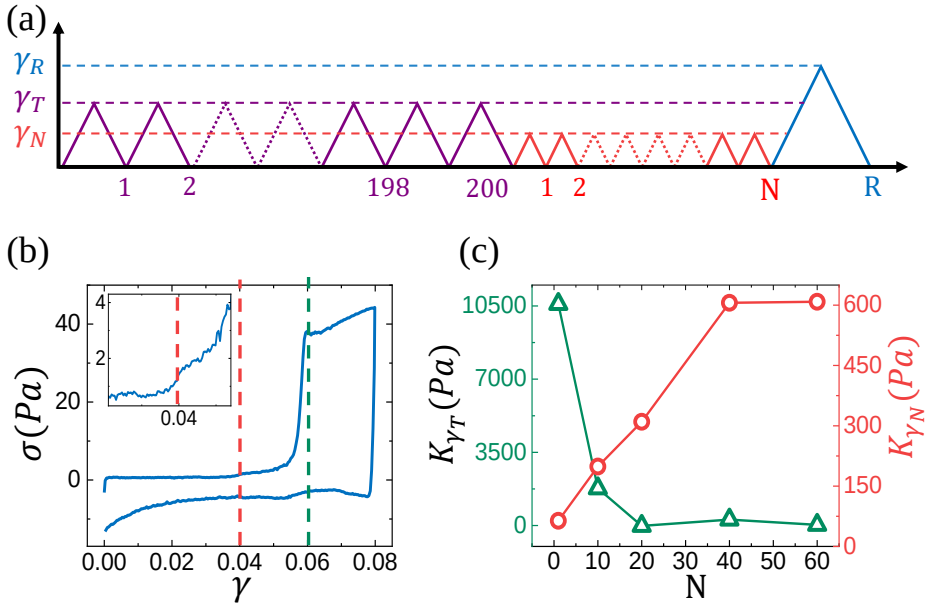

Figure 5.1: (a) Schematic showing the triangular wave shear deformation protocol used to train the system at γ_T (depicted in violet), followed by a second training at $\gamma_N < \gamma_T$ for number of cycles N (depicted in red). Finally a readout is taken at $\gamma_R > \gamma_T$ (depicted in blue). (b) A readout Lissajous curve taken for $\gamma_T = 0.06$ (indicated in the figure by blue dashed line) and $\gamma_N = 0.04$ (indicated in the figure by red dashed line) for the case of $N = 10$. Inset shows a magnified view of the same curve around $\gamma_T = 0.04$ (indicated by the red dashed line). (c) Variation of the readout differential shear modulus (K) at γ_T (in green) and γ_N (in red) as a function of N for $\gamma_T = 0.06$ and $\gamma_N = 0.04$. The points shown here are averaged over three independent experimental runs. Error bars are not shown for the purpose of clarity.

to encode a second memory. After the N cycles of γ_N, I take a readout as shown in Fig. 5.1(a). Our readout consists of a single pulse of the triangular wave but with an amplitude $\gamma_R > \gamma_T$ [16]. Throughout the entire protocol, I maintain the same shear rate of 0.01 s^{-1}. For each set of γ_T and γ_N, I vary N from 1 to 60 in discrete steps. In Fig. 5.1(b), I show a typical readout Lissajous plot for $N = 10$ with $\gamma_T = 0.06$ and $\gamma_N = 0.04$ (indicated in the figure by dashed lines). I observe a sharp change in stress at $\gamma_T = 0.06$ which corresponds to the encoded memory at that amplitude [16]. There is also a mild change at γ_N (inset of Fig. 5.1(b)), indicating a second memory formation at γ_N.

I characterize strength of the encoded memory by the differential shear modulus (K) [16]. As discussed in the previous chapter, K_γ is a good measure of any memory signature present in the system at strain amplitude γ. Thus, for readouts taken at different number of cycles (N), I look at the value of K corresponding to the two amplitudes that were

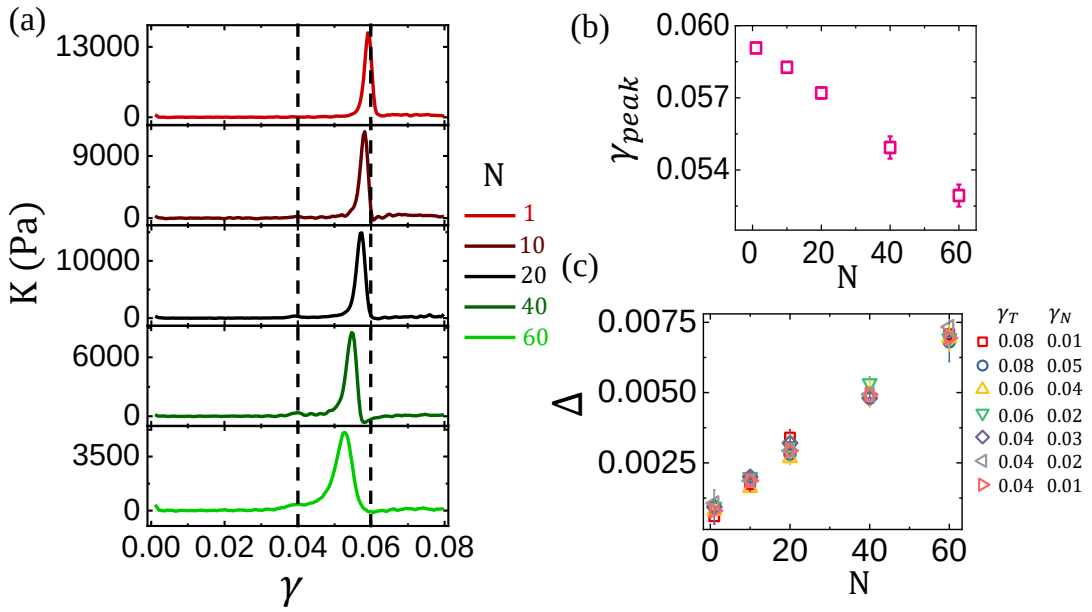

Figure 5.2: (a) Differential shear modulus (K) plotted against strain amplitude γ for readouts taken at different number of cycles (N) as indicated by the color bars. For each N here, I show a single independent run. Dashed vertical lines indicate the two training strain amplitudes $\gamma_T = 0.06$ and $\gamma_N = 0.04$. The shear rate is $0.01s^{-1}$. (b) The peak position (γ_{peak}) (corresponding to the strongest peak in K) of the readout plotted as a function of N. (c) The peak shift parameter (Δ) defined as $\Delta = \gamma_T - \gamma_{peak}$ is plotted as a function of N for different values of the two training strain amplitudes γ_T and γ_N indicated by the color panel.

encoded into the system. In Fig. 5.1(c), I plot K_{γ_T} and K_{γ_N} as a function of N for the case of $\gamma_T = 0.06$ and $\gamma_N = 0.04$. While K_{γ_T} starts from a high value at $N = 1$, with increasing N, it rapidly drops to a negligible value, indicating a progressive weakening and eventual elimination of the memory at γ_T. Simultaneously, the second memory at γ_N gets strengthened (with eventual saturation) as indicated by the increase in K_{γ_N} with N. This is in sharp contrast to what has been observed in numerical studies by Adhikari and Sastry [9]. Under a similar protocol, the memory of the first amplitude, in their case, merely suffers a mild weakening as a result of applying a second amplitude (the mean square displacement (MSD) goes from zero to a non-zero value but both memory signatures survive). While they do not observe any progressive effects of applying a smaller amplitude to the trained system, for our system the effect appears in a systematic manner. Also, they report that a single strain cycle of the smaller amplitude was able to encode a memory [9] but in our case it takes a few cycles to establish a discernible memory corresponding to the smaller strain amplitude γ_N.

The gradual decay and loss of memory at γ_T has an interesting consequence. I note that for our system, γ_T is the largest applied amplitude of deformation until the readout. Now, in systems that show Mullins or Kaiser type memory behavior, studies have reported that largest applied amplitude of deformation gets affected only when the system is driven to an even larger amplitude (a process that I will, henceforth, refer to as over-driving) [6, 16, 19]. This is the first instance where I report that the largest applied deformation is affected without the system being over-driven.

Further, to investigate the loss of memory, I plot the individual readouts taken after different number of cycles (N) in Fig. 5.2(a) with dashed vertical lines indicating $\gamma_T = 0.06$ and $\gamma_N = 0.04$. As explained before, a peak in the differential shear modulus K indicates the memory at the corresponding strain γ [16]. Also, the first encoded memory (at γ_T) is much stronger than that of the second memory (at γ_N) hence the dominant peak is due to the memory at γ_T. I observe a systematic shift in the position of the dominant peak in K towards γ_N. This is further highlighted in Fig. 5.2(b), where the strongest peak position (γ_{peak}) is plotted as a function of N. Clearly, the shifting of the peak position is responsible for the loss of the memory at γ_T that I see in Fig. 5.1(c). Thus, the loss of memory is not absolute, rather, the memory simply appears at a different strain amplitude that is intermediate to both the amplitudes encoded in the system. Thus, the memory signatures at these intermediate amplitudes are phantom memories, as these amplitudes were not encoded into the system through training.

I define a peak shift parameter Δ as $\Delta = \gamma_T - \gamma_{peak}$. For different values of γ_T and γ_N, in the range of 0.01 to 0.08, I plot the corresponding Δ vs number of cycles of perturbation (N) in Fig. 5.2(c). The collapse of Δ vs N for all pairs of γ_T and γ_N indicates that the memory shifting behaviour is, in fact, a general phenomena in this strain range and, more importantly, the underlying mechanism remains the same. In some cases, where $\delta\gamma = \gamma_T$ - γ_N is small (for example for $\delta\gamma = 1$), I observe a merging of the two peaks by $N = 60$ cycles (see Fig. 5.3). For those cases, I have plotted Δ vs N only till the peaks merge.

Next, I study the effect of shear rate on the shifting of the encoded memory. In Fig. 5.4(a) and (b), I show K vs γ (similar to Fig. 5.2(a)) at different N for shear rates of $0.02s^{-1}$ and $0.04s^{-1}$, respectively, for $\gamma_T = 0.06$ and $\gamma_N = 0.04$. Interestingly, I find that the shifting of memory becomes much more dramatic, particularly at the highest shear rate where I observe merging of the two memories (see the last two panels of Fig. 5.4(b)), indicating that the system now remembers only one amplitude and the other memory is entirely lost. In Fig. 5.5, I plot the γ_{peak} (indicating the shifted peak position of the encoded memory at γ_T) as a function of N to highlight the peak position shifting at the

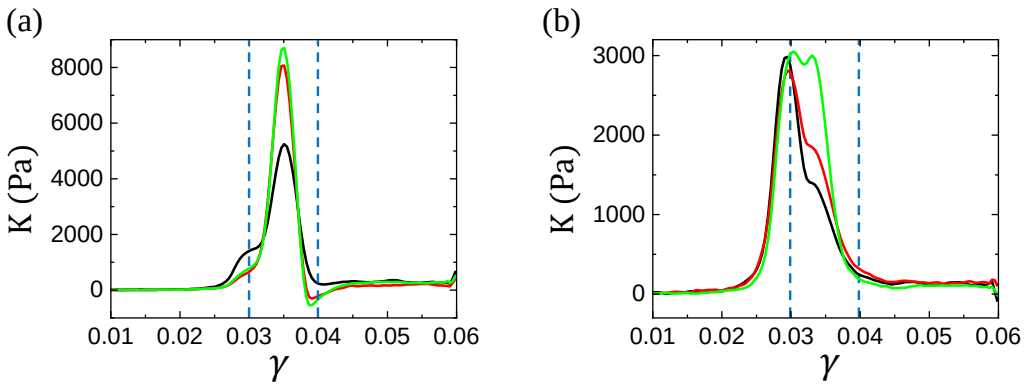

Figure 5.3: Figure shows three independent runs (shown by different colors) for training strain amplitudes $\gamma_T = 0.04$ and $\gamma_N = 0.03$ after (a) $N = 40$ and (b) $N = 60$ cycles of applying the smaller strain amplitude. I observe that while the two peaks in each run are very close for $N = 40$ cycles, they have clearly merged by $N = 60$ cycles.

higher shear rates.

I note here that at higher shear rates, the memory at γ_N is comparatively stronger than that at shear rate of $0.01s^{-1}$, consequently the two peaks (indicative of the two memories in the system) become comparable in some cases. In Fig. 5.6, I show the comparison of Δ vs N at the three shear rates. While the behavior at $0.02s^{-1}$ still remains linear but with a higher slope (indicating the faster shift in the position of the memory formed initially at γ_T), I observe a deviation from linearity at larger N in case of 0.04s^{-1}. This deviation is due to the merging of the peaks and the uncertainty in defining the stronger peak (see Fig. 5.5). I checked the peak values (K_{peak}) at all three rates but did not find a clear trend with increasing N as shown in Fig. 5.7.

The progressive shifting indicates that the number of cycles of perturbation (N) plays a crucial role. So, I characterize the response of the system during the process of encoding of the second memory (at the smaller strain amplitude) by plotting the stress vs. strain (Lissajous plot) for different cycles. In Fig. 5.8, I show Lissajous plots for the lowest and highest shear rates of $0.01s^{-1}$ (in Fig. 5.8(a) to (c)) and $0.04s^{-1}$ (in Fig. 5.8(d) to (f)). For each shear rate, I show the Lissajous plot for $N = 1$ (Fig.5.8(a) and (d)) and $N = 60$ (Fig. 5.8(b) and (e)) (indicated by the shaded cycles in the schematic shown in Fig. 5.8).The response of the system just before applying the smaller strain amplitude is similar in nature, for both the shear rates, showing a strong strain stiffening response near γ_T (as shown in purple Lissajous plots in 5.8). However, the system's evolution during the cycles encoding the second memory depends on the applied shear rate. At both these shear rates, the first cycle of encoding the second amplitude is contained within

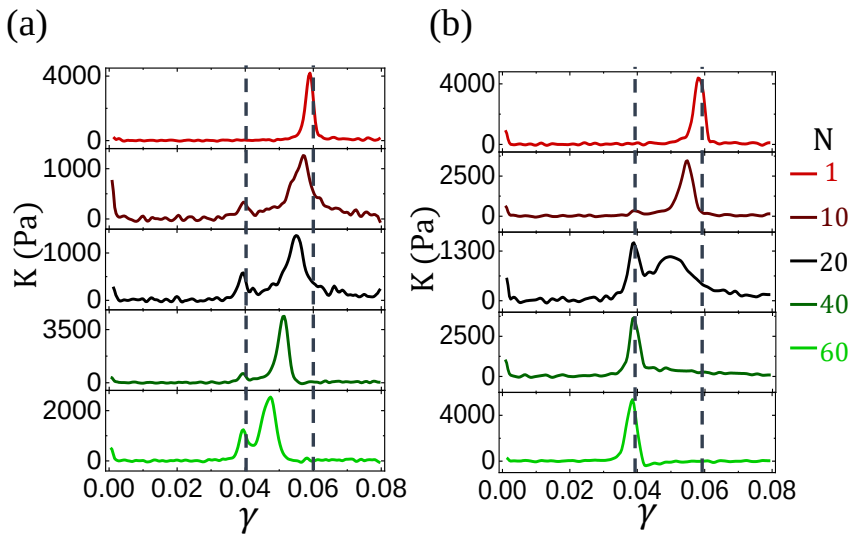

Figure 5.4: Differential shear modulus (K) plotted against γ for readouts taken at different number of cycles N as indicated by the color bars. For each N here, I show a single independent run. The shear rate is $0.02s^{-1}$ in (a) and $0.04s^{-1}$ in (b). For both (a) and (b), dashed vertical lines indicate the training strain amplitudes $\gamma_T = 0.06$ and $\gamma_N = 0.04$.

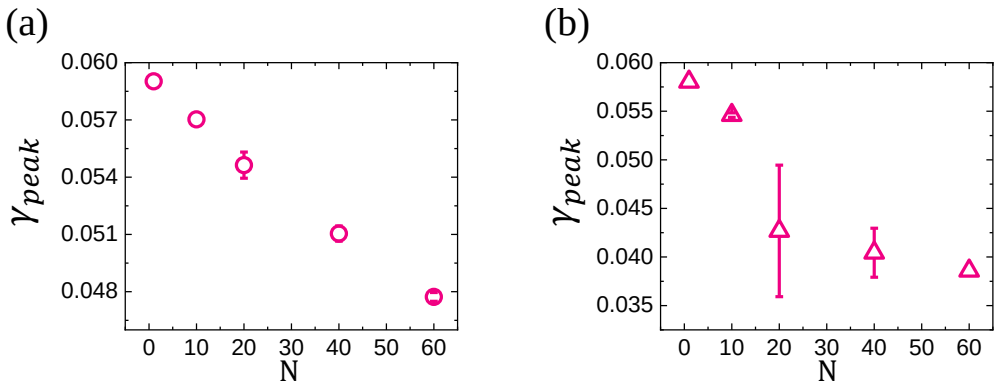

Figure 5.5: Variation of the strongest peak position γ_{peak} as a function of number of cycles N for shear rate 0.02s^{-1} in (a) and 0.04s^{-1} in (b). The data points are averaged over three independent measurements. Data shown here is for $\gamma_T = 0.06$ and $\gamma_N = 0.04$. The large error bar for 0.04s^{-1} at larger N is due to similar strength of the peaks at the two amplitudes that the system remembers, making it difficult to define a clear stronger peak.

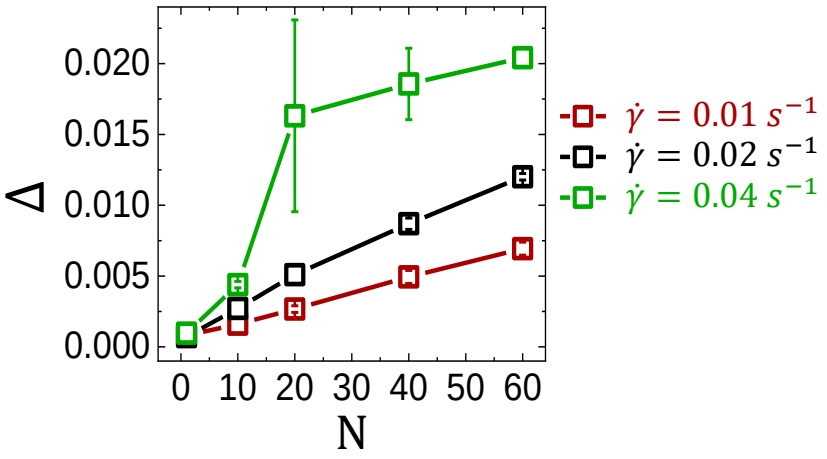

Figure 5.6: Shear rate dependence of the peak shift parameter Δ defined as $\Delta = \gamma_T - \gamma_{peak}$ plotted as a function of N. The slope for the linear range with N increases with increasing shear rate. At the highest shear rate, a deviation from linear behavior is observed as a result of merging of the two memories and uncertainty in determining the stronger peak position.

the Lissajous plots corresponding to the memory at γ_T (Fig. 5.8(a) and (d)), but after 60 cycles, the degree of strain stiffening at the second amplitude (γ_N) is dramatically enhanced for higher shear rates as highlighted in Fig. 5.8(c) and (f). However, I observe that in both cases, the Lissajous figures undergo maximum evolution for the strain values close to γ_N (see Fig. 5.8(c) and (f)).

Based on the reversible contact formation in this system, as explained in the last chapter, I propose a coherent picture to explain our data: during the encoding of the second memory, there is a direction reversal of the input strain at γ_N, which allows structure buildup, resulting in strain stiffening at γ_N. Also, during this process, the system

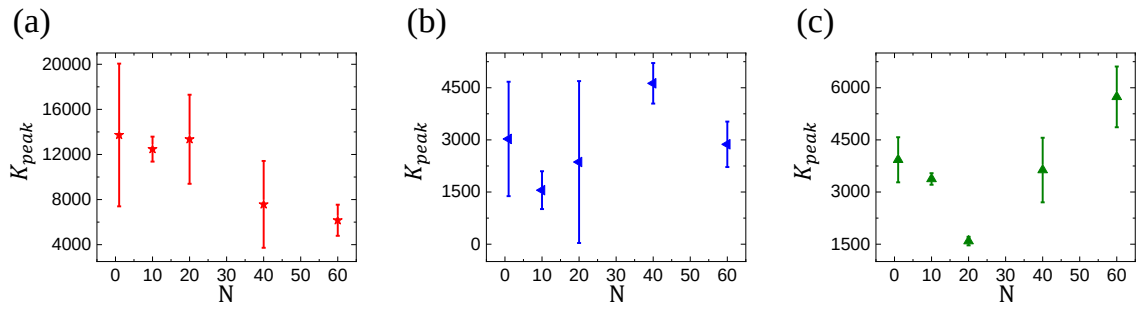

Figure 5.7: Variation of peak strengths (K_{peak}) with number of cycles N averaged over three independent measurements for shear rate 0.01s^{-1} in (a), 0.02s^{-1} in (b) and 0.04s^{-1} in (c)

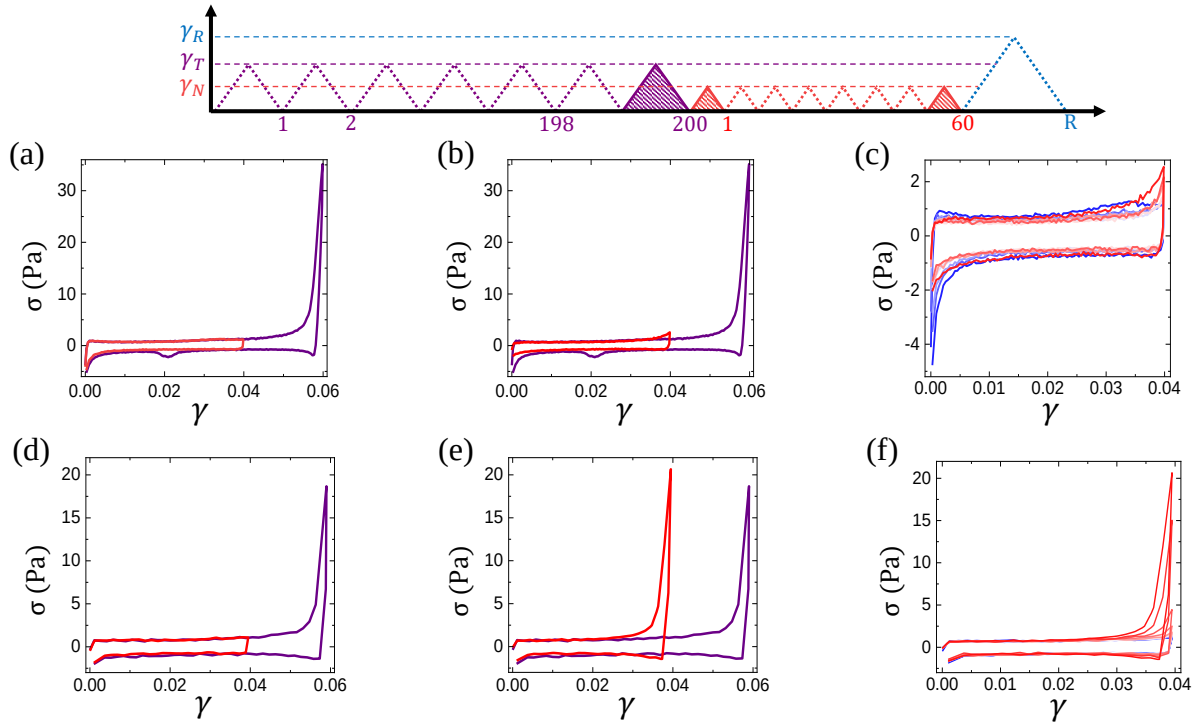

Figure 5.8: Top panel is a schematic of the entire protocol with the shaded cycles indicating those cycles for which I analyse the system's behavior as Lissajous plots in (a)-(f). Here, the first training strain amplitude is $\gamma_T = 0.06$ and the second smaller amplitude is $\gamma_N = 0.04$. Shear rate is 0.01s^{-1} for (a)-(c) and 0.04s^{-1} for (d)-(f). I show the Lissajous plot of the system after $N = 200$ cycles of γ_T alongwith the Lissajous plots after $N = 1$ at γ_N (in (a) and (d)) and after $N = 60$ at γ_N (in (b) and (e)). In (c) and (f), I show the just the evolution during the $N = 60$ cycles at γ_N at the two shear rates for some discrete N values. Color scheme is as indicated in the schematic at the top.

is not over-driven beyond γ_N, allowing the rejoined contacts to survive and get gradually reinforced. This structural reorganization should reflect in the energy dissipation in the system. The area enclosed by the Lissajous plots (shown in Fig. 5.8(c) and (f)) gives the energy dissipated over a cycle of perturbation [18]. I divide each Lissajous plot into 4 quadrants as shown in Fig. 5.9(a). Over $N = 60$ cycles, I plot the variation of normalized dissipation ($\frac{E_N}{E_1}$) in each of the quadrants for the shear rate of $0.04s^{-1}$ in Fig. 5.9(b) (Here, E_N is the dissipation in the N^{th} cycle and E_1 is that for $N = 1$). The normalization takes care of any load to load variation in the absolute values of stress/dissipation. I find that the normalized dissipation monotonically rises in quadrant IV while in the other three, the evolution is minimal with increasing N, as also seen from the Lissajous plots in Fig. 5.8. Such enchanted dissipation in quadrant IV indicates the large restructuring around γ_N. Finally, in Fig. 5.9(c), I compare the normalized dissipation for the three shear rates in quadrant I(left panel) and IV (right panel). The other two quadrants are shown in Fig. 5.10. I observe the dissipation remains higher in quadrant IV for all shear rates and has a systematic dependence on shear rate.

5.4 Conclusion

In this work, I study the effects of encoding a second memory in an adhesive granular gel that is already trained upto a larger amplitude. I find that with increasing number of cycles (N) of the smaller amplitude γ_N, the memory signature at the first training amplitude γ_T drops to zero, indicating a destruction of the memory at γ_T. Interestingly, this memory loss is not absolute but is a result of a memory shift in the system. The memory signature corresponding to γ_T shifts systematically towards the second memory at γ_N. Such memory shift has never been reported or predicted for any system to the best of our knowledge. Additionally, this memory shifting causes the system to have a phantom memory that was not encoded/written into it. I find that this memory shift is much faster for higher shear rates. I use energy dissipation analysis of the system during the encoding of the second memory to explain this phenomena.

The phantom memory, that was not encoded/written into the system, is an interesting result and needs to be explored in more detail. So far, memory formation in physical systems was limited to only those memories that were explicitly encoded into the system. Moreover, the memory shifting phenomena offers us an external handle on what the system remembers. I would also like to highlight that this is the first instance where I find loss of memory from the system without applying a larger strain amplitude. Also, as

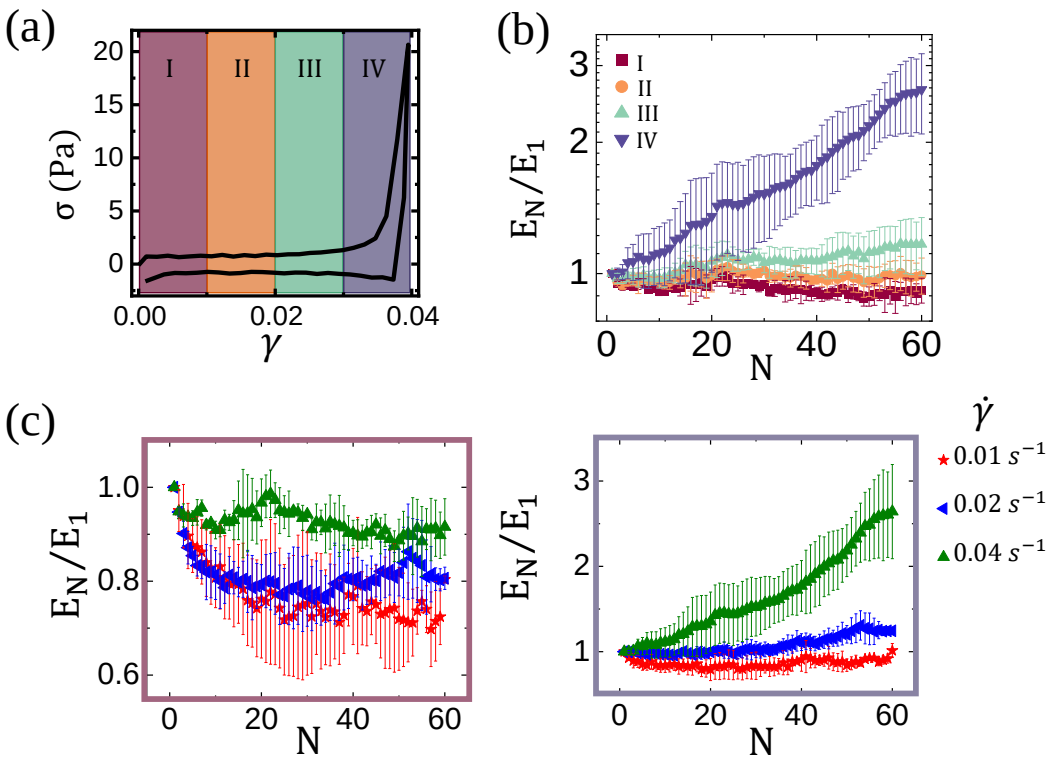

Figure 5.9: (a) A typical Lissajous plot for applied smaller amplitude $\gamma_N = 0.04$ at shear rate of $0.04s^{-1}$. The area enclosed by the Lissajous is divided into four quadrants as indicated in the figure. (b) Quadrant wise evolution of normalized energy dissipation $(\frac{E_N}{E_1})$ with number of cycles N. Here, the system is first trained at $\gamma_T = 0.06$ and then a smaller amplitude $\gamma_N = 0.04$ is applied. The color scheme follows the quadrant wise division shown in (a) (also indicated in the legend). (c) Evolution of normalized energy dissipation as a function of N for quadrant I(top panel) and IV(bottom panel) at the three shear rates indicated in the figure. Box colors are coded according to the color scheme of (a).

a result of the memory shift, the memory at γ_T is not lost but merely stored at a different strain amplitude in the system.

5.5 Appendix: Applying a larger amplitude to an encoded memory

As mentioned in the Results and discussion and also depicted in Chapter-4, applying a larger amplitude destroys the existing memory signatures in the system. In fact this destruction is nearly catastrophic as shown in the Fig. 5.11. I train the system at

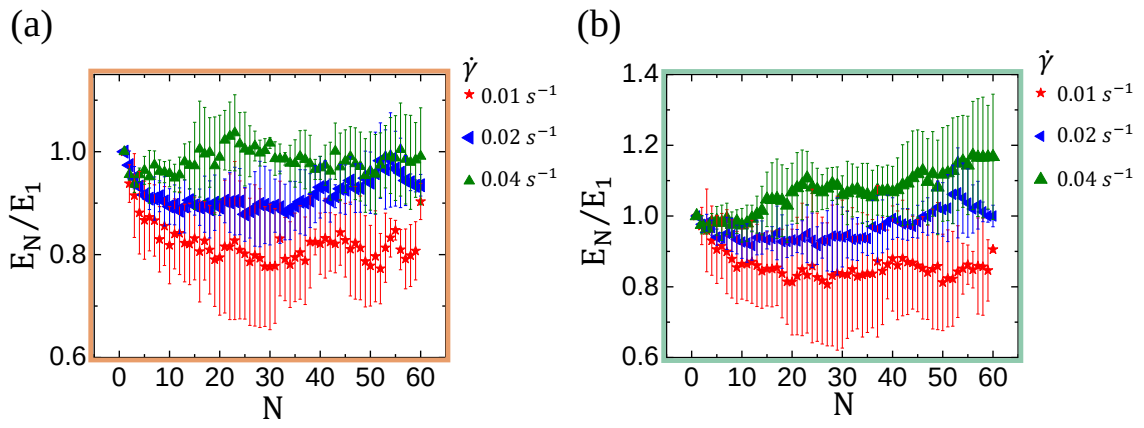

Figure 5.10: Evolution of normalized energy dissipation ($\frac{E_N}{E_1}$) with number of cycles N for quadrant II in (a) and III in (b) at the three shear rates indicated in the figure. The system is trained at $\gamma_T = 0.06$, followed by at $\gamma_N = 0.04$. The box colors follow the quadrant wise color scheme depicted in Fig. 5.9(a).

$\gamma_T = 0.04$ and apply $\gamma_N = 0.08$ for $N = 3$ cycles here, as indicated by the schematic. I note that while the first cycle of 0.08 shows a clear signature at 0.04, the Lissajous plots for the 2nd and 3rd cycle hardly show any variation across 0.04. Clearly the memory of $\gamma_T = 0.04$ is lost within one cycle.

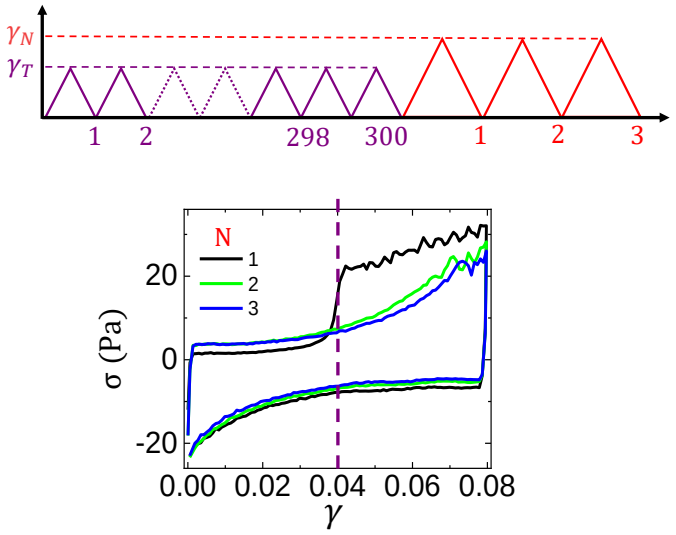

Figure 5.11: Bottom panel shows the system's response when a training at an amplitude $\gamma_T = 0.04$ is followed by a second set of training at a larger amplitude ($\gamma_N = 0.08$). Top panel is a schematic of such a protocol. I show the data here for 3 cycles (N) of the larger amplitude γ_N as indicated by the schematic. Notice that while $N = 1$ has a clear signature of the encoded memory of γ_T at 0.04, $N = 2$ onwards there is essentially no signature. This indicates that the larger amplitude catastrophically erases the memory of the smaller amplitude in the system.

Bibliography

[1] D. J. Pine, J. P. Gollub, J. F. Brady, and A. M. Leshansky. Chaos and threshold for irreversibility in sheared suspensions. *Nature*, 438(7070):997–1000, Dec 2005.

[2] Laurent Corté, P. M. Chaikin, J. P. Gollub, and D. J. Pine. Random organization in periodically driven systems - Nature Physics. *Nat. Phys.*, 4:420–424, May 2008.

[3] Nathan C. Keim and Sidney R. Nagel. Generic Transient Memory Formation in Disordered Systems with Noise. *Phys. Rev. Lett.*, 107(1):010603, Jun 2011.

[4] Nathan C. Keim, Joseph D. Paulsen, and Sidney R. Nagel. Multiple transient memories in sheared suspensions: Robustness, structure, and routes to plasticity. *Phys. Rev. E*, 88(3):032306, Sep 2013.

[5] Joseph D. Paulsen, Nathan C. Keim, and Sidney R. Nagel. Multiple Transient Memories in Experiments on Sheared Non-Brownian Suspensions. *Phys. Rev. Lett.*, 113(6):068301, Aug 2014.

[6] Joseph D. Paulsen and Nathan C. Keim. Minimal descriptions of cyclic memories. *Proc. R. Soc. A.*, 475(2226):20180874, June 2019.

[7] Davide Fiocco, Giuseppe Foffi, and Srikanth Sastry. Oscillatory athermal quasistatic deformation of a model glass. *Phys. Rev. E*, 88(2):020301, Aug 2013.

[8] Davide Fiocco, Giuseppe Foffi, and Srikanth Sastry. Encoding of Memory in Sheared Amorphous Solids. *Phys. Rev. Lett.*, 112(2):025702, Jan 2014.

[9] Monoj Adhikari and Srikanth Sastry. Memory formation in cyclically deformed amorphous solids and sphere assemblies. *Eur. Phys. J. E*, 41(9):105–17, September 2018.

[10] Srimayee Mukherji, Neelima Kandula, A. K. Sood, and Rajesh Ganapathy. Strength of Mechanical Memories is Maximal at the Yield Point of a Soft Glass. *Phys. Rev. Lett.*, 122(15):158001, Apr 2019.

[11] Nathan C Keim, Jacob Hass, Brian Kroger, and Devin Wieker. Global memory from local hysteresis in an amorphous solid. *Physical Review Research*, 2(1):012004, 2020.

[12] Nathan C. Keim and Dani Medina. Mechanical annealing and memories in a disordered solid. *Sci. Adv.*, 8(40):eabo1614, October 2022.

[13] Chloe W. Lindeman and Sidney R. Nagel. Multiple memory formation in glassy landscapes. *Sci. Adv.*, 7(33), August 2021.

[14] Chloe W. Lindeman, Varda F. Hagh, Chi Ian Ip, and Sidney R. Nagel. Competition between Energy and Dynamics in Memory Formation. *Phys. Rev. Lett.*, 130(19):197201, May 2023.

[15] Travis R. Jalowiec, Chloe W. Lindeman, and Nathan C. Keim. Isolating the enhanced memory of a glassy system. *arXiv*, June 2023.

[16] Sebanti Chattopadhyay and Sayantan Majumdar. Inter-particle adhesion induced strong mechanical memory in a dense granular suspension. *J. Chem. Phys.*, 156(24):241102, June 2022.

[17] Dor Shohat and Yoav Lahini. Dissipation Indicates Memory Formation in Driven Disordered Systems. *Phys. Rev. Lett.*, 130(4):048202, January 2023.

[18] Sebanti Chattopadhyay, Sharadhi Nagaraja, and Sayantan Majumdar. Effect of adhesive interaction on strain stiffening and dissipation in granular gels undergoing yielding. *Commun. Phys.*, 5(126):1–10, May 2022.

[19] Nathan C Keim, Joseph D Paulsen, Zorana Zeravcic, Srikanth Sastry, and Sidney R Nagel. Memory formation in matter. *Reviews of Modern Physics*, 91(3):035002, 2019.

CHAPTER

SIX

Probing shear jamming in dense particulate suspensions using steady shear rheology

The results of this chapter are published in [1].

6.1 Introduction

Dense particulate suspensions show a range of non-linear flow behavior under shear, as I explained in section 1.4.4. One of them is the dramatic increase in viscosity during Discontinuous Shear Thickening (DST) and eventual jamming of the system. Hydrodynamic lubrication based models alone are not sufficient to understand strong shear-thickening in dense suspensions [2], as the inter-particle friction also plays a key role [3, 4, 5]. Recent numerical studies [6, 7] demonstrate that DST originates from stress induced rapid build-up of frictional contacts when lubrication layers between the particles break down due to enhanced inter-particle pressure at high stress (σ) values. For a wide range of suspensions, it has been found that the critical applied stress (σ_C) required to overcome the lubrication barrier between the particles and establish frictional contacts exhibits an inverse square dependence on the particle diameter ($\sigma_C \propto d^{-2}$) [8].

In recent years, experiments reveal that at very large values of volume fraction (ϕ), approaching the random close packing fraction (ϕ_{rcp}), many of these systems get into a shear induced solid-like state known as shear jammed (SJ) state having a finite yield stress [9, 10, 11, 12, 13, 14]. The existence of such solid-like SJ state has been predicted earlier by a phenomenological model by Wyart and Cates (WC) [15] based on stress induced enhancement of the number of frictional contacts in the system as a function of increasing applied stress beyond a threshold. WC model predicts that for frictional particles, the viscosity of the system will diverge at a stress dependent jamming packing fraction $\phi_J(\sigma)$ given by,

$$\phi_J(\sigma) = f(\sigma)\,\phi_m + [1 - f(\sigma)]\phi_0 \tag{6.1}$$

where, $f(\sigma)$ is the fraction of particles making frictional contacts with friction coefficient $\mu > 0$, ϕ_0 and ϕ_m represent jamming packing fractions for $f = 0$ (when all the contacts are lubricated) and $f = 1$ (when all the contacts are frictional), respectively. Dense suspensions are extremely complex due to the presence of large number of degrees of freedom and microscopic interactions. WC model provides microscopic insights of shear-thickening and jamming behaviour in these systems, based on a single stress dependent parameter $f(\sigma)$. Remarkably, wide range of dense suspensions of frictional particles agrees with WC model despite having very different microscopic details [16].

While steady state viscosity measurements successfully describe the shear-thickening

behaviour, they cannot capture signatures of SJ state [11]. The main difficulty to probe shear-induced jamming by steady state rheology measurement originates from the fact that in a rigid solid-like SJ state, it is not possible to produce steady-velocity gradients. In this state, the sample can only flow by producing various failures. Such failures give rise to a finite apparent viscosity of a shear jammed state when the real viscosity should tend to infinity. The experimental studies that distinguish the shear-jammed state from a shear-thickened state [11, 13, 14] measure transient stress response of the suspension. However, studies in references [11, 13] also point out that the steady state flow curves do not directly show any signature of the Shear Jamming transition. To our knowledge, there are no studies that experimentally distinguish a SJ state from a shear-thickened state based only on steady state flow curves.

In this chapter, I study the shear-thickening behaviour of suspensions formed by Polystyrene (PS) particles over a wide range of ϕ and σ values. From the steady state flow-curves I obtain systematic deviations of viscosity from the KD relation (an empirical relation that gives the dependence of relative viscosity of a suspension as a function of volume fraction of the suspension, see [17]) for large σ and ϕ values. Using such deviations together with WC model (Eq. 6.1), I predict the onset stress for Shear Jamming (σ_{SJ}) for a given packing fraction. Our conclusion of weakening of the sample at high stress and volume fractions (as concluded from the deviations from KD relation) is consistent with the expected failures caused due to the flow of solid-like SJ state. Furthermore, the agreement of our data with WC model brings out the importance of frictional contacts to observe shear-jamming. Although, both KD relation and WC model have been widely studied in the context of dense suspensions, to our knowledge, they have not been used to determine σ_{SJ}. Thus, our experiments propose a novel method to distinguish a SJ state from a shear-thickened state, entirely from the steady state measurements.

6.2 Materials and methods

Suspensions are formed by dispersing PS particles in polyethylene glycol (PEG-400) [18] at different volume fractions ϕ ranging from 0.4 - 0.6. Details of particle synthesis, SEM imaging and sample preparation, are mentioned in section 2.2.4 and 2.3.2 respectively. Rheology measurements are carried out using a stress controlled Rheometer (see section 2.2.1) with parallel plate (plate diameter of 25 mm and a gap of 300 μm) and cone-plate (cone diameter of 25 mm and cone angle $\approx 2^o$) geometries at a temperature of 25^{o}C.

To obtain steady state flow-curves (shown in Fig. 6.2(e)), I vary the applied shear

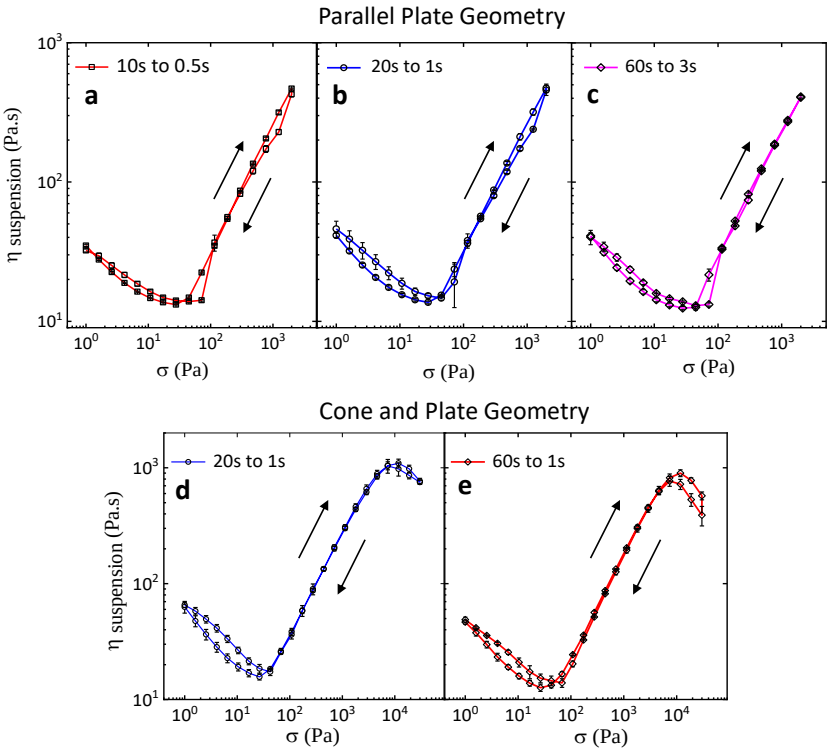

Figure 6.1: Reversibility and waiting-time dependence of shear-thickening of PS in PEG system ($\phi = 0.58$, $d = 1.21$ μm). (a), (b) and (c) indicates suspension viscosity ($\eta_{suspension}$) as a function of applied stress (σ) for both increasing and decreasing stress values for different waiting-time per data point, as indicated. These measurements are done with a parallel-plate (P-P) geometry. (d) and (e) indicate the same measurements with a cone and plate (C-P) geometry. I observe that the shear-thickening behaviour is very similar (in both the geometries) for increasing and decreasing stress values, indicating negligible hysteresis effect for this system. Further, the shear-thickening response does not show any waiting time-dependence, signifying a steady state behaviour of the system. In all cases, the $\eta_{suspension}$ vs σ curves for increasing stress values are averaged over three experimental runs. Similarly, for decreasing stress values the curves are also averaged over the three runs. The error bars are the corresponding standard deviations.

stress on the sample with a waiting time per data point varying logarithmically from 20 s (at the lowest stress) to 1 s (at the highest stress). I choose such protocol, because, for lower applied stress values, the shear rate produced in the sample is very small. To measure the viscosity reliably, I need to wait for a sufficient time for the sample to undergo appreciable strain deformation. On the other hand, higher values of applied stress (deep inside the shear-thickening regime) produce high shear rate. So, the sample already undergoes significant strain deformation within a very short time. Under high shear rate, I find that there is a tendency of the sample to gradually protrude out of the rheometer plates that can result in measurement artefacts. I also vary the waiting time per data point over a range as shown in the Fig. 6.1. I obtain almost the same flow-curves for all the waiting times, signifying that waiting time per data point for our experiment is sufficient for the system to reach a steady state.

While, many recent studies find that shear-thickening in dense particulate suspensions are reversible [18, 19, 20], few others report significant hysteresis effects [9, 21]. For our system (PS particles in PEG), I find that hysteresis effects are negligible for both parallel-plate as well as cone-plate geometries as shown in figure (Fig. 6.1). Such reversibility and instantaneous shear-thickening response is also reported earlier for a similar system [18].

6.3 Results and discussions

Typical Scanning Electron Microscopy (SEM) images of the synthesized particles (Fig. 6.2(a) - (c)) along with the size distributions (Fig. 6.2(d)) are shown. Flow curves, showing the relative viscosity ($\eta_r = \frac{\eta_{suspension}}{\eta_{solvent}}$) as a function of applied shear-stress (σ) at different packing fractions (ϕ) are plotted in Fig. 6.2(e) for almost six orders of magnitude of stress variation for mean particle diameter $d = 1.21$ μm. After an initial Newtonian/shear-thinning region, there is a shear-thickening region at higher values of σ beyond a stress onset σ_0, when η_r increases strongly for $\phi \geq 0.55$. The onset stress (σ_0) is given by the minimum applied stress for which $\frac{d\ log(\eta_r)}{d\ log(\sigma)} > 0$ (indicated in Fig.6.2(e) with a bold arrow). Physically, σ_0 indicates the minimum stress scale for inducing frictional contacts between two particles in the suspension, overcoming the residual inter-particle interactions [2].

I see from Fig. 6.2(f) that η_r increases monotonically with increasing ϕ values at a particular value of σ (= 28 Pa, as indicated by the vertical dashed-line in Fig. 6.2(e)). Such non-linear increase in viscosity as a function of volume fraction can be described by the empirical Krieger-Dougherty (KD) model for spherical particles: $\eta_r = (1 - \frac{\phi}{\phi_J})^{-2}$ [15, 17]. This model predicts that as the particle volume fraction (ϕ) gradually increases,

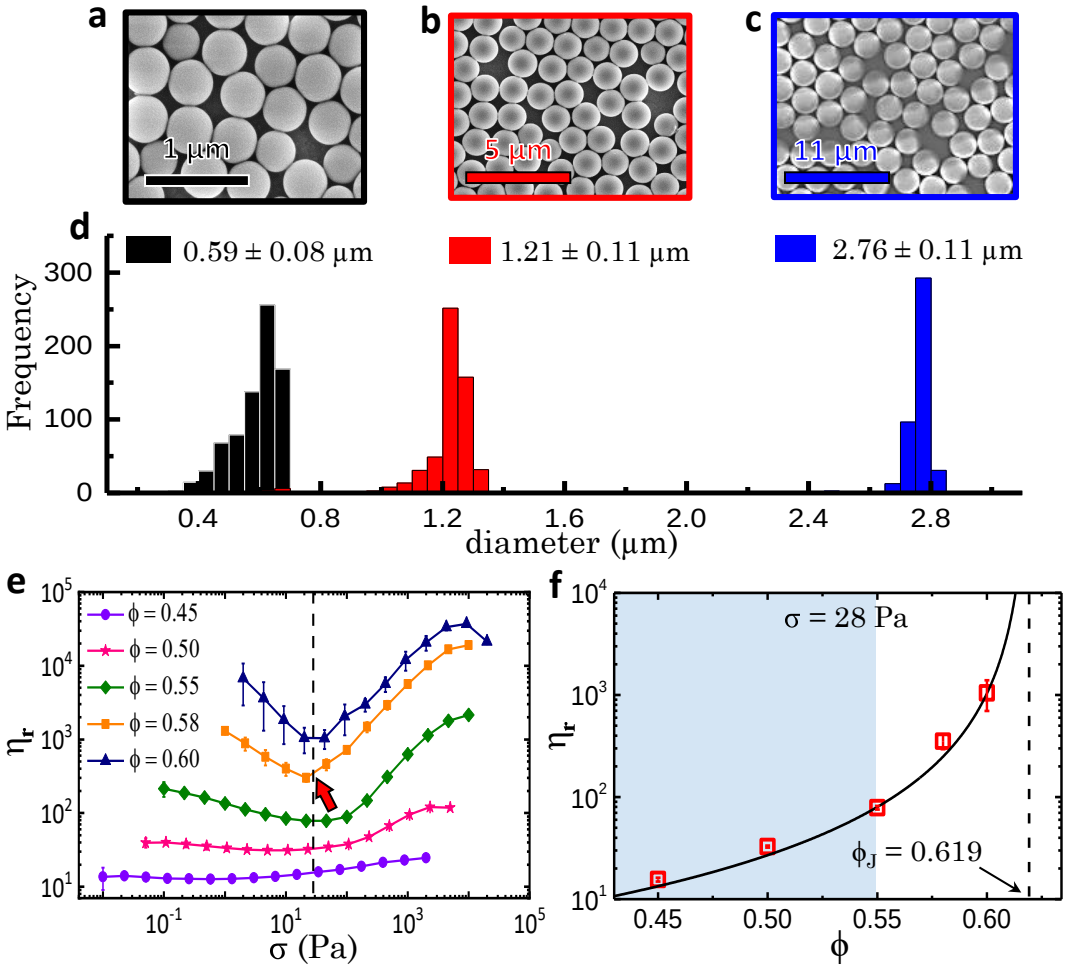

Figure 6.2: (a) - (c), SEM images of synthesized PS microspheres for three different sizes. (d) Histograms indicating the distribution of particle size with mean diameter (d) and standard deviation indicated in the figure. (e) Relative viscosity (η_r) as a function of applied shear stress (σ) for particles with $d = 1.21$ μm for different volume fractions ϕ. The onset stress (σ_0) for $\phi = 0.58$ is marked with a bold arrow. The error bars are the standard deviations of viscosity for two independent measurements. (f) η_r vs ϕ for the value of σ indicated by the dashed line in panel (e). The solid-line in (f) indicates a fit of KD relation to the three data points for $\phi = 0.45$, 0.5 and 0.55 (shaded region). The vertical dashed-line indicates the value of ϕ_J (described in the text).

the viscosity (η_r) also increases and finally diverges when ϕ closely approaches ϕ_J, the jamming packing fraction. To avoid the complications due to material failures (such as those arising from plasticity and sample fractures) originating from the flow of the solid-like SJ state, I restrict our fitting up to the random loose packing ϕ_{rlp} (~ 0.55) of the system, below which shear induced jamming is not expected [22]. So, I fit the data only over the range of packing fractions $0.45 \leq \phi \leq 0.55$ (shaded region) in Fig. 6.2(f). I also compare the ϕ_J values obtained from this fitting range to that obtained from a slightly larger range $0.4 \leq \phi \leq 0.55$ for different σ values (Fig. 6.3). I get identical values of ϕ_J in all cases. Importantly, for smaller values of ϕ, the shear rate produced in the sample becomes very high at higher values of applied stress and the sample tends to come out of the rheometer plates. For this reason, I cannot extend the range down to $\phi = 0.4$ for very high stress values (see Fig. 6.3). For the rest of the chapter, I will stick to the range $0.45 \leq \phi \leq 0.55$ for fitting KD model. η_r vs ϕ shows a very good agreement with KD model as shown by the fitted solid-line in Fig. 6.2(f), with $\phi_J = 0.619$.

Next, using the flow curve data (η_r vs σ) for different ϕ values, I show the variation of η_r as a function of ϕ for different σ values in Fig. 6.4. For simplicity, I have shown such flow curve data only for $d = 1.21$ μm in Fig. 6.2(e). In Fig. 6.5, I explain the detailed procedure to obtain η_r vs ϕ for different σ values from the flow-curves. In Fig. 6.4(a), I show η_r vs ϕ for $d = 0.59$ μm when σ is gradually increased from the left most to the right most panel. For a given value of σ I fit KD model to the data over the shaded region ($0.45 \leq \phi \leq 0.55$). I obtain very good agreement for lower σ values, however, with increasing σ, the fits systematically deviate from the experimentally measured data points for higher values of ϕ. Similar trends are also observed for $d = 1.21$ μm (Fig. 6.4(b)) and $d = 2.76$ μm (Fig. 6.4(c)) particles, albeit, over different stress ranges. This indicates that for large σ and ϕ values, the experimentally measured η_r is much lower compared to the KD predictions. I interpret that these deviations indicate shear-induced solidification of the suspension where steady velocity gradient cannot be maintained without failures in the sample. Here, I use the term 'failure' in a very general sense. In disordered materials, brittle-fracture, shear band plasticity, localized non-affine deformations are the most likely mechanism for yielding/failure [23]. However, with our present imaging set-up (resolution of ~ 50 pixels/mm), I can only observe extreme failures like macroscopic crack formation due to brittle failure at very high applied stress values (see Fig. 6.6(e), (f) and movie https://drive.google.com/drive/folders/13rkUmYfJVYzJgmbzUYP_ojKfMj3F7I2e?usp=sharing (refer to Appendix for movie description)) and not the more subtle ones. Such failures weaken the stress response of the

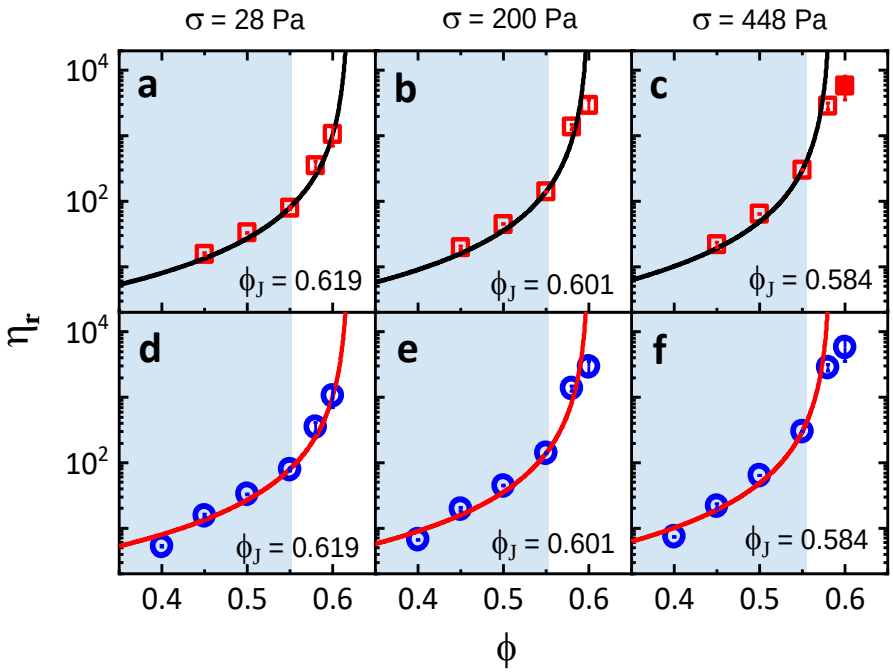

Figure 6.3: Comparison of the value of jamming packing fraction ϕ_J for different range of fitting. (a), (b) and (c) show the fits to KD equation (described in the text) for σ values obtained over the range $0.45 \leq \phi \leq 0.55$. Same fitting is shown over the range $0.4 \leq \phi \leq 0.55$ in (d), (e) and (f). The fitting parameters (ϕ_J) obtained for a given σ value are same (up to at least 3 decimal places) for both the fitting ranges (as indicated in the figure). Importantly, for $\phi = 0.4$, the suspension viscosity being relatively low, very high applied stress ($\sigma > 1000$ Pa) produces high shear rates. Under such high shear rates, the sample tends to protrude out of the rheometer plates. For this reason, I cannot get a reliable viscosity value for $\phi = 0.4$ for $\sigma > 1000$ Pa. So, I can not compare the data for $\sigma = 2000$ Pa (shown in Fig. 6.4(b) for $0.45 \leq \phi \leq 0.55$).

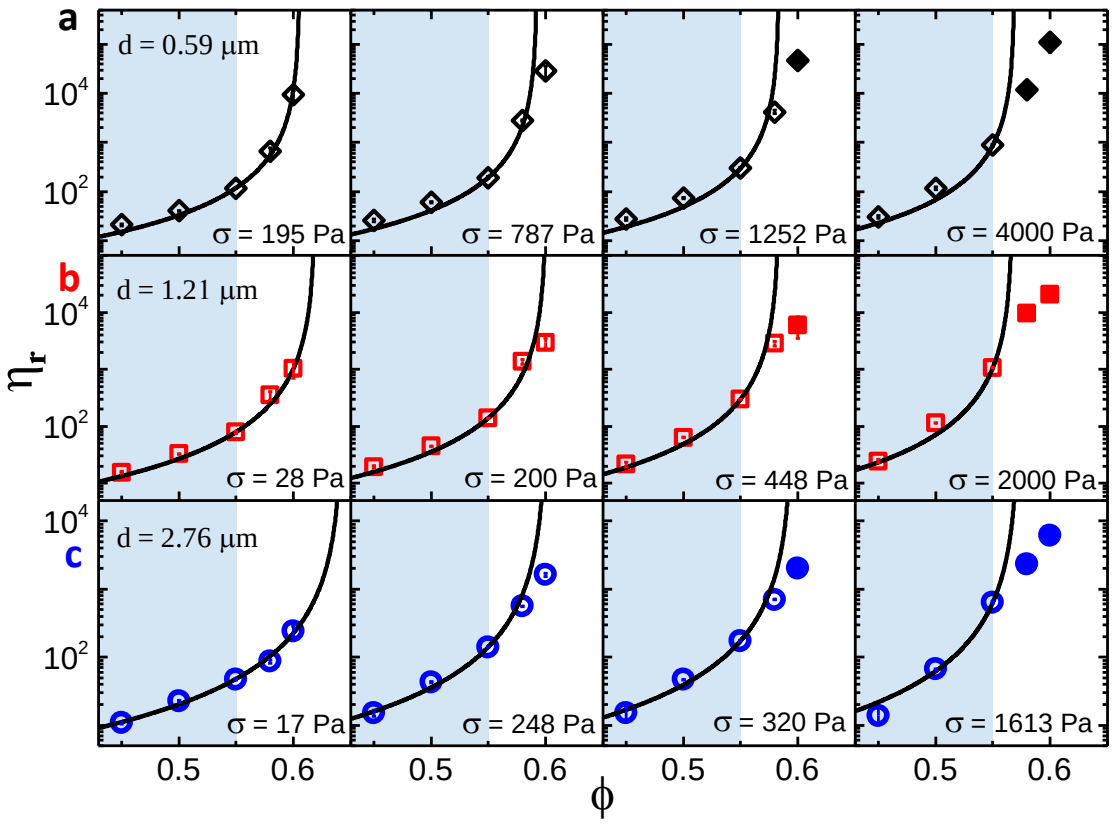

Figure 6.4: Relative viscosity (η_r) as a function of volume fraction (ϕ) for different applied stress (σ) values as indicated. Each row represents a particular mean size of the particles; (a) $d = 0.59$ μm, (b) $d = 1.21$ μm, (c) $d = 2.76$ μm. The solid line is a fit to KD relation based on the values of ϕ in the shaded region. For all three sizes of the particles, I obtain significant deviation (indicated by solid symbols) from KD fits for large σ and ϕ values. The error bars are the standard deviations of viscosity for two independent measurements and are small compared to the size of the symbols in most cases.

sample that translates into a lower value of the measured viscosity.

I now study stress dependence of jamming packing fraction $\phi_J(\sigma)$ obtained from the fitted KD curves shown in Fig. 6.4. I find that, with increasing values of σ, $\phi_J(\sigma)$ decreases as shown in Fig. 6.6(a) ($d = 0.59$ μm), (b) ($d = 1.21$ μm) and (c) ($d = 2.76$ μm). Such stress dependence of ϕ_J can be well described by WC model (Eq. 6.1). The exact form for $f(\sigma)$ can not be determined experimentally. Motivated by earlier studies [24, 25], an exponential form for $f(\sigma)$ is introduced [16]. However, it is found that a stretched exponential form, $f(\sigma) = e^{-(\sigma^*/\sigma)^\beta}$ gives better agreement with the experimental data [16]. The exponent β is a fitting parameter that gives the range of stress values over which shear-thickening is observed. Higher the value of β, lower will be the stress range for shear-thickening. The solid lines in Fig. 6.6(a)-(c) indicate the fits of WC model to the experimental data, where I get an excellent agreement. This observation reconfirms the microscopic picture of stress induced conversion of the lubricated contacts into the frictional ones. For $d = 0.59$ μm, 1.21 μm and 2.76 μm I get the respective β values of 1.19, 0.99 and 0.74. Such trend indicates that the range of stress values for shear-thickening decreases with decreasing particle size. For a typical value of $\beta \sim 1$, an applied stress $\sigma = \sigma^*$ gives $f(\sigma) = 1/e$. Thus, σ^* gives a stress scale when the system develops sufficient number of frictional contacts and is proportional (but not equal) to the average onset stress (σ_0) for shear-thickening [26]. Like the onset stress, σ^* also shows similar dependence on particle size [16]: $\sigma^* \sim 1/d^2$ (see Fig. 6.7).

Physically, WC model predicts the packing fraction of particles $\phi_J(\sigma)$ for a given applied stress σ at which the viscosity of the suspension $\eta_r(\sigma)$ diverges. It implies that, for a given σ value, the suspension having packing fraction ϕ ($> \phi_J(\sigma)$) should behave like a jammed solid with infinite viscosity. Thus, existence of finite viscosity for the parameter range marked by the shaded regions in Fig. 6.6(a)-(c) is not expected. I conjecture that such finite value of viscosity at high σ and ϕ values can be observed (e.g. Fig. 6.2(e) and Fig. 6.4) if the sample develops flow induced failures. For a given ϕ, the onset stress for Shear Jamming (σ_{SJ}) is determined from the stress value σ for which, $\phi = \phi_J(\sigma)$ (shown in Fig. 6.6(b) by dashed vertical lines for $\phi = 0.58$ and 0.6). I show the SJ region (shaded region) for $d = 1.21$ μm in Fig. 6.6(d) with σ_{SJ} values are indicated for $\phi = 0.58$ and 0.6. I find that σ_{SJ} decreases for increasing ϕ. Such trend has also been reported for SJ under transient forcing [11, 14]. I perform in-situ optical imaging of the sample in the flow-gradient ($\mathbf{v}$, $\nabla\mathrm{v}$) plane (see movie https://drive.google.com/drive/folders/13rkUmYfJVYzJgmbzUYP_ojKfMj3F7I2e?usp=sharing and refer to Appendix for movie description) while measuring the flow-curves. Since, the particles are optically opaque,

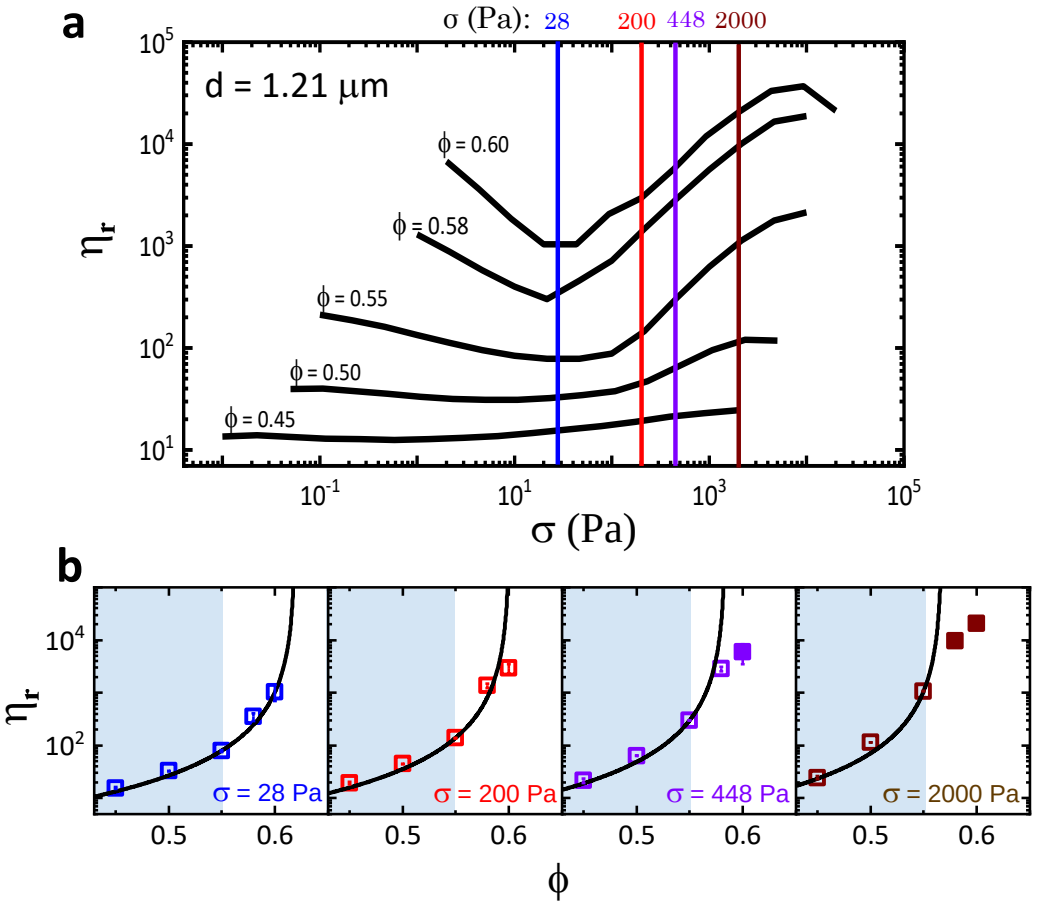

Figure 6.5: Detailed protocol for obtaining relative viscosity η_r vs volume fraction ϕ (indicated in Fig. 6.2) from steady state flow curves. Panel (a) shows steady state flow curves (η_r vs σ) for different ϕ values ranging from 0.45 to 0.6 (also shown in Fig. 6.2(e)). I first draw a vertical line for a particular stress value (say, $\sigma = 28$ Pa), I find the intersection points for the corresponding vertical line (blue) with the flow curves to get η_r vs ϕ, for $\sigma = 28$ Pa as shown in the left-most panel in (b). I repeat this procedure for different stress values in an increasing order (as indicated with different coloured vertical lines in (a)) to obtain the other panels in (b). In (b), η_r vs ϕ are shown for increasing σ values from left to the right most panels. Here, $d = 1.21$ μm (Fig. 6.2(b)).

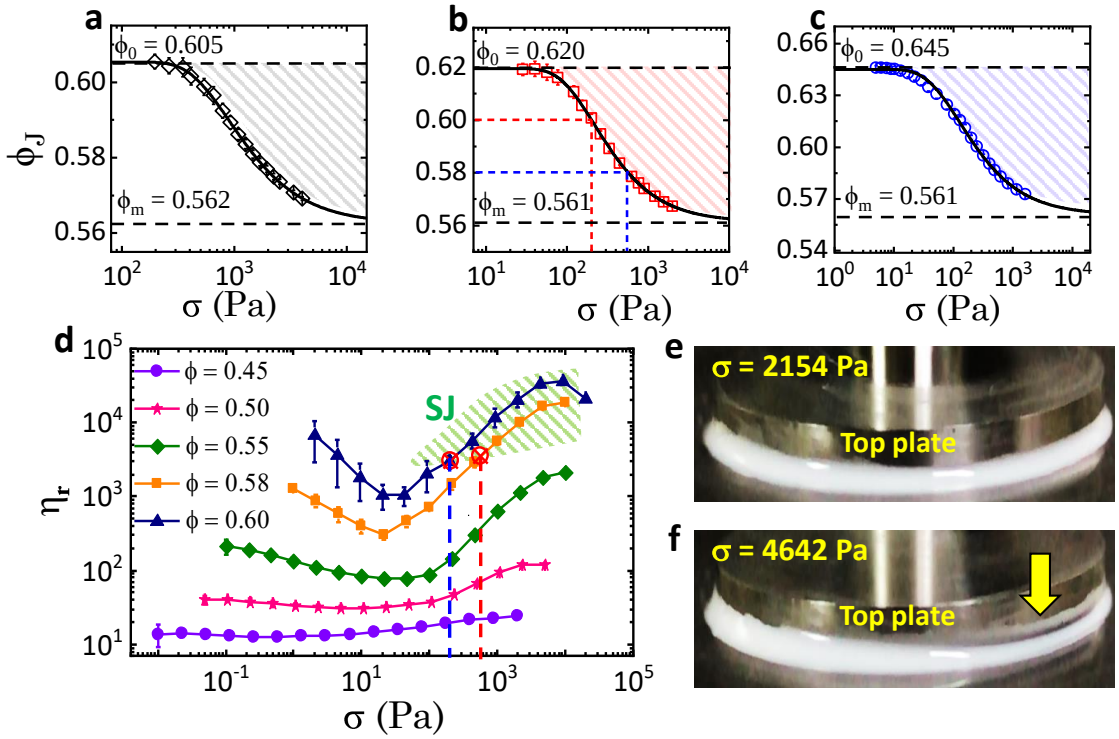

Figure 6.6: Jamming packing fraction (ϕ_J) as a function of applied stress (σ) for different particle sizes: (a) $d = 0.59$ μm, (b) $d = 1.21$ μm, (c) $d = 2.76$ μm. The solid lines are the fit to WC model. Shaded region predicts the parameter range for SJ (mentioned in the text). (d) Steady state flow curves for $d = 1.21$ μm. The shaded region indicates the SJ regime with σ_{SJ} is indicated for $\phi = 0.58$ (blue dashed-line) and $\phi = 0.6$ (red dashed-line), obtained from (b). (e) and (f) show optical images of the sample boundary between the rheometer plates inside SJ regime, for $\phi = 0.58$. For very high stress values, partial detachment of the sample from the plate (due to brittle failure) is observed (as indicated by the bold arrow). The aspect ratio is changed from the original images for clarity.

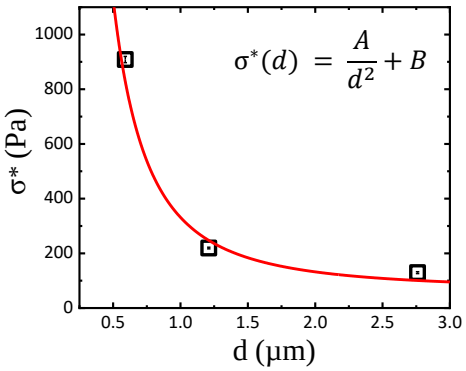

Figure 6.7: Variation of the parameter σ^* (mentioned in the text) with particle size. I get a trend $\sigma^* \sim \frac{1}{d^2}$. The values of the fitting parameters (indicated in the figure) $A = 265.58\ Pa.\mu m^2$ and $B = 65.89\ Pa$.

I can only image the sample boundary. Deep inside the SJ regime, I indeed find detachment and edge fracture of the sample (Fig. 6.6(e), (f) and movie https://drive.google.com/drive/folders/13rkUmYfJVYzJgmbzUYP_ojKfMj3F7I2e?usp=sharing (refer to Appendix for movie description)), reconfirming the formation of solid-like SJ state under shear.

For $d = 2.76\ \mu$m (Fig. 6.6(c)), I find that the value of ϕ_0 (indicated in Eq. 6.1) approaches the random close packing ($\phi_{rcp} \approx 0.64$) for a system of monodisperse hard spheres [15, 22]. I also observe that ϕ_0 systematically drops from ϕ_{rcp} value as the particle size decreases (Fig. 6.6(a) and (b)). This indicates a deviation from ideal hard sphere behaviour due to residual inter-particle interactions [27]. Although, I do not know the exact nature of such interactions, the systematic drop from ϕ_{rcp} value with decreasing particle size indicates that such interactions are predominantly induced by particle-surfaces [28, 19], since, for a given packing fraction, the smaller particles will have a larger surface to volume ratio. This observation is also consistent with the decrease in shear-thickening range for smaller particle sizes (higher values of β) that indicates enhanced inter-particle interactions [29]. The parameter ϕ_m corresponds to the minimum volume fraction required for shear induced jamming. I find that in our study $\phi_m \approx 0.56$ in all cases. This value of ϕ_m is very close to random loose packing ($\phi_{rlp} \sim 0.55$) for monodisperse hard spheres [22]. This observation also agrees with the reported lower-limit for observing jamming in frictional systems [22]. Also, the similar values of ϕ_m for all the particle sizes indicate that despite differences in the residual inter-particle interactions, the stress-induced frictional interactions between the particles are very similar.

6.4 Conclusions

In conclusion, I propose a novel method to predict the onset of Shear Jamming in dense particulate suspensions entirely based on steady state rheological measurements. I generalize our results for a range of particle sizes. In all cases, the predicted onset stress values for Shear Jamming (σ_{SJ}) are found to decrease with increasing ϕ, a trend also obtained from transient measurements [11, 14]. In our case, the optical imaging can not detect any signature of sample failure for stress values just beyond σ_{SJ} (predicted from our analysis) as shown in the movie (see https://drive.google.com/drive/folders/13rkUmYfJVYzJgmbzUYP_ojKfMj3F7I2e?usp=sharing and refer to Appendix for movie description). I believe that our analysis captures the weakening of the sample due to microscopic failures in random locations of the sample. However, these failures are only visible when they merge and grow to macroscopic length-scales under increasing stress. This implies that our analysis is more sensitive in picking up the onset of SJ state as compared to our optical imaging method probing failures in the sample. Since, the resolution of our imaging is not very good, I can only see extreme failures (like brittle fracture, macroscopic crack formation etc.) but not plastic shear bands and other subtler features. Further, due to the opaque nature of the sample, the failures happening inside the bulk of the sample (not on the surface) will not be optically visible. The generality of our analysis for systems with different particle shapes and interactions needs to be verified. Furthermore, comparison of the predicted value of σ_{SJ} from our steady state measurements with that obtained from transient measurements or directly by more sophisticated optical/non-optical imaging techniques probing sample failures, remain an interesting future challenge. I hope that our experiments will motivate further studies on shear induced jamming in dense suspensions.

6.5 Appendix: Movie description

In-situ deformation of the sample boundary in the flow-gradient ($\mathbf{v}$, ∇v) plane is captured during the steady state flow-curve measurement (Fig. 6.6(d)) as shown in movie. The movie is captured by a digital camera (iPhone X) with a resolution of 1920 X 1080 pixels at frame rate of 60 Hz with a spatial resolution of $\sim$ 50 pixels/mm. The optically opaque nature of the sample enables us to track the boundary deformations as a function of increasing applied stress values. At large values of applied stress (indicated in the movie), there is a clear signature of detachment of the sample from the shearing plate. However,

as the applied stress is removed such failure starts to recover when the sample is again transformed back to a liquid like state from a shear jammed state.

Bibliography

[1] Subhransu Dhar, Sebanti Chattopadhyay, and Sayantan Majumdar. Signature of jamming under steady shear in dense particulate suspensions. *J. Phys.: Condens. Matter*, 32(12):124002, December 2019.

[2] Eric Brown and Heinrich M. Jaeger. Shear thickening in concentrated suspensions: phenomenology, mechanisms and relations to jamming. *Rep. Prog. Phys.*, 77(4):046602, April 2014.

[3] Nicolas Fernandez, Roman Mani, David Rinaldi, Dirk Kadau, Martin Mosquet, Hélène Lombois-Burger, Juliette Cayer-Barrioz, Hans J. Herrmann, Nicholas D. Spencer, and Lucio Isa. Microscopic Mechanism for Shear Thickening of Non-Brownian Suspensions. *Phys. Rev. Lett.*, 111(10):108301, September 2013.

[4] Neil Y. C. Lin, Ben M. Guy, Michiel Hermes, Chris Ness, Jin Sun, Wilson C. K. Poon, and Itai Cohen. Hydrodynamic and Contact Contributions to Continuous Shear Thickening in Colloidal Suspensions. *Phys. Rev. Lett.*, 115(22):228304, November 2015.

[5] Cécile Clavaud, Antoine Bérut, Bloen Metzger, and Yoël Forterre. Revealing the frictional transition in shear-thickening suspensions. *Proc. Natl. Acad. Sci. U.S.A.*, 114(20):5147–5152, May 2017.

[6] Ryohei Seto, Romain Mari, Jeffrey F. Morris, and Morton M. Denn. Discontinuous Shear Thickening of Frictional Hard-Sphere Suspensions. *Phys. Rev. Lett.*, 111(21):218301, November 2013.

[7] Romain Mari, Ryohei Seto, Jeffrey F. Morris, and Morton M. Denn. Shear thickening, frictionless and frictional rheologies in non-Brownian suspensions. *J. Rheol.*, 58(6):1693–1724, November 2014.

[8] BM Guy, Michiel Hermes, and Wilson CK Poon. Towards a unified description of the rheology of hard-particle suspensions. *Physical review letters*, 115(8):088304, 2015.

[9] Sayantan Majumdar, Rema Krishnaswamy, and A. K. Sood. Discontinuous shear thickening in confined dilute carbon nanotube suspensions. *Proc. Natl. Acad. Sci. U.S.A.*, 108(22):8996–9001, May 2011.

[10] M. I. Smith, R. Besseling, M. E. Cates, and V. Bertola. Dilatancy in the flow and fracture of stretched colloidal suspensions. *Nat. Commun.*, 1(114):1–5, November 2010.

[11] Ivo R. Peters, Sayantan Majumdar, and Heinrich M. Jaeger. Direct observation of dynamic shear jamming in dense suspensions. *Nature*, 532(7598):214–217, April 2016.

[12] Sayantan Majumdar, Ivo R. Peters, Endao Han, and Heinrich M. Jaeger. Dynamic shear jamming in dense granular suspensions under extension. *Phys. Rev. E*, 95(1):012603, January 2017.

[13] Nicole M. James, Endao Han, Ricardo Arturo Lopez de la Cruz, Justin Jureller, and Heinrich M. Jaeger. Interparticle hydrogen bonding can elicit shear jamming in dense suspensions. *Nat. Mater.*, 17(11):965–970, November 2018.

[14] Endao Han, Nicole M. James, and Heinrich M. Jaeger. Stress Controlled Rheology of Dense Suspensions Using Transient Flows. *Phys. Rev. Lett.*, 123(24):248002, December 2019.

[15] M. Wyart and M. E. Cates. Discontinuous Shear Thickening without Inertia in Dense Non-Brownian Suspensions. *Phys. Rev. Lett.*, 112(9):098302, March 2014.

[16] B. M. Guy, M. Hermes, and W. C. K. Poon. Towards a Unified Description of the Rheology of Hard-Particle Suspensions. *Phys. Rev. Lett.*, 115(8):088304, August 2015.

[17] Irvin M. Krieger and Thomas J. Dougherty. A Mechanism for Non-Newtonian Flow in Suspensions of Rigid Spheres. *Transactions of The Society of Rheology*, 3(1):137–152, March 1959.

[18] Jianbin Qin, Guangcheng Zhang, and Xuetao Shi. Study of a shear thickening fluid: the suspensions of monodisperse polystyrene microspheres in polyethylene glycol. *J. Dispersion Sci. Technol.*, 38(7):935–942, July 2017.

[19] Brent J. Maranzano and Norman J. Wagner. The effects of interparticle interactions and particle size on reversible shear thickening: Hard-sphere colloidal dispersions. *J. Rheol.*, 45(5):1205–1222, September 2001.

[20] Kun Lin, Hongjun Liu, Minghai Wei, Annan Zhou, and Fanrui Bu. Dynamic performance of shear-thickening fluid damper under long-term cyclic loads. *Smart Mater. Struct.*, 28(2):025007, December 2018.

[21] Clarence E. Chu, Joel A. Groman, Hannah L. Sieber, James G. Miller, Ruth J. Okamoto, and Jonathan I. Katz. Hysteresis and Lubrication in Shear Thickening of Cornstarch Suspensions. *arXiv*, May 2014.

[22] Leonardo E. Silbert. Jamming of frictional spheres and random loose packing. *Soft Matter*, 6(13):2918–2924, June 2010.

[23] Alexandre Nicolas, Ezequiel E. Ferrero, Kirsten Martens, and Jean-Louis Barrat. Deformation and flow of amorphous solids: Insights from elastoplastic models. *Rev. Mod. Phys.*, 90(4):045006, December 2018.

[24] Daniel Howell, R. P. Behringer, and Christian Veje. Stress Fluctuations in a 2D Granular Couette Experiment: A Continuous Transition. *Phys. Rev. Lett.*, 82(26):5241–5244, June 1999.

[25] Corey S. O'Hern, Stephen A. Langer, Andrea J. Liu, and Sidney R. Nagel. Force Distributions near Jamming and Glass Transitions. *Phys. Rev. Lett.*, 86(1):111–114, January 2001.

[26] Ben M. Guy, Christopher Ness, Michiel Hermes, Laura J. Sawiak, Jin Sun, and Wilson C. K. Poon. Testing the Wyart-Cates model for non-Brownian shear thickening using bidisperse suspensions. *arXiv*, January 2019.

[27] The influence of particles on suspension rheology | Anton Paar Wiki, July 2023. [Online; accessed 10. Jul. 2023].

[28] Brent J. Maranzano and Norman J. Wagner. The effects of particle size on reversible shear thickening of concentrated colloidal dispersions. *J. Chem. Phys.*, 114(23):10514–10527, June 2001.

[29] Eric Brown, Nicole A. Forman, Carlos S. Orellana, Hanjun Zhang, Benjamin W. Maynor, Douglas E. Betts, Joseph M. DeSimone, and Heinrich M. Jaeger. Generality of shear thickening in dense suspensions. *Nat. Mater.*, 9(3):220–224, March 2010.

CHAPTER

SEVEN

Orthogonal vibration induced control of jamming in dense suspensions

7.1 Introduction

In the previous chapters, I have mentioned that athermal systems (like jammed granular suspensions) are stuck in their out of equilibrium state as the thermal energy at room temperature is insufficient to allow these systems to evolve in any way. To trigger any evolution in such systems requires externally applied perturbations/excitations with much higher energy scales compared to the thermal fluctuations. So far in this thesis, I have been using shear as the only controlled external drive to study how such systems evolve. In this chapter, I will study shear response of the system in presence of controlled external vibrations applied to the system.

Systematic studies have established the physics of dry grains under vibration. Effects such as granular segregation, brazil-nut effect and granular compaction are well established in the literature [1, 2, 3, 4, 5, 6, 7]. More recent interest has been in the physics of vibrated wet granular media like dense suspensions of athermal particles [8, 9, 10, 11]. In these studies typically the particles are heavier than the suspending fluid, thus gravitational settling of the particles ensures frictional contact formation in the system, even under static conditions, that results in the formation of a jammed bed having an yield stress. Such yield stress has been measured using the Taylor-Couette geometry.

Studies on these systems have reported that the frictional yield stress can be tuned by applying orthogonal vibrations to the system [9, 11, 12]. Flow curves (viscosity vs applied shear stress) show that while at low shear stress vibration systematically reduces the viscosity of the suspension, flow behavior at higher applied stress is hardly affected by the vibrations. There is a crossover from a vibration dominated flow regime to a shear dominated flow regime with increasing applied shear stress. Effects of particle size, viscosity of the suspending fluid as well as the stress due to the applied vibration have been studied in the context of frictional yield stress. The vibration stress is defined as:

$$\sigma_V = \frac{1}{2}\rho A^2(2\pi f)^2 \tag{7.1}$$

where ρ is the density of the suspension, A and f are the amplitude and frequency of the applied vibrations respectively. However, it remains unclear whether superimposed vibrations have similar effects for yield stress systems where the yield stress originates from inter-particle adhesive/attractive interactions, as studied in the Chapter-3 of this thesis.

Additionally, with increasing recent interest in shear-thickening and shear-jamming of dense suspensions, there have been efforts to control Discontinuous Shear Thickening

and Shear-Jamming by using orthogonal superimposed vibrations [13, 14, 15, 16, 17, 18]. Despite the promising results, this relatively new area of research still harbours many open questions.

Here, I explore the effects an orthogonal vibration has on dense suspensions that exhibit adhesion induced yield stress. In the latter part, I also explore the effects of vibration on the shear-thickening behavior of dense suspensions formed by particles that are density matched with the suspending fluid.

7.2 Materials and methods

Dense suspensions with adhesive inter-particle interactions were formed by dispersing Cornstarch particles (CS) in Paraffin oil (PO) at a volume fraction of 0.4 and in density matched Organic oil at a volume fraction of 0.46 (see section 2.3.1 for details of the system and sample preparation techniques). For shear thickening suspensions, I use poly-disperse Polystyrene (PS) particles in PEG 400 at a volume fraction of 0.67. Experiments were performed in a Couette geometry with a profiled bob (Anton Paar) with a diameter of 19.6mm and a home made outer cup of diameter 30mm. The cup is mounted on an electromagnetic shaker (LDS V201, Brüel & Kjær, UK). Using this setup, the cup can be made to vibrate orthogonal to the shear direction as shown in the schematic of the setup in Fig. 7.1. I use a high speed camera (Phantom, MIRO C210) to capture in-situ images of the vibrating cup. By tracking some markers on the surface of the cup and using image analysis, I characterize the amplitude and frequency of the vibrations as shown in Fig. 7.2.

7.3 Results and Discussion

First, I study the flow behavior of the adhesive suspensions under steady shear (in the absence of vibration). In Fig. 7.3(a) and (b), I plot the flow curves (stress vs shear rate) for the Cornstarch-Paraffin oil system and Cornstarch-Organic oil system, respectively. I observe non-monotonic flow behavior at low shear rates (particularly for the CS-Paraffin oil system) as observed for other attractive/adhesive systems before [19, 20].

Now, I apply orthogonal vibrations to both these systems of different frequencies at two different values of input current: 0.1A and 0.3A. The flow curves in presence of vibration are plotted in Fig. 7.4 for CS-Paraffin oil and Fig. 7.5 for CS-Organic oil systems.

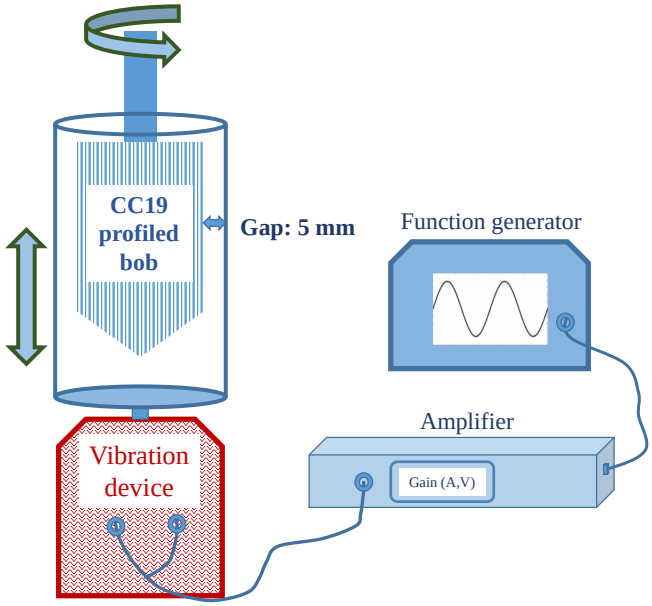

Figure 7.1: Figure shows a schematic of the setup.

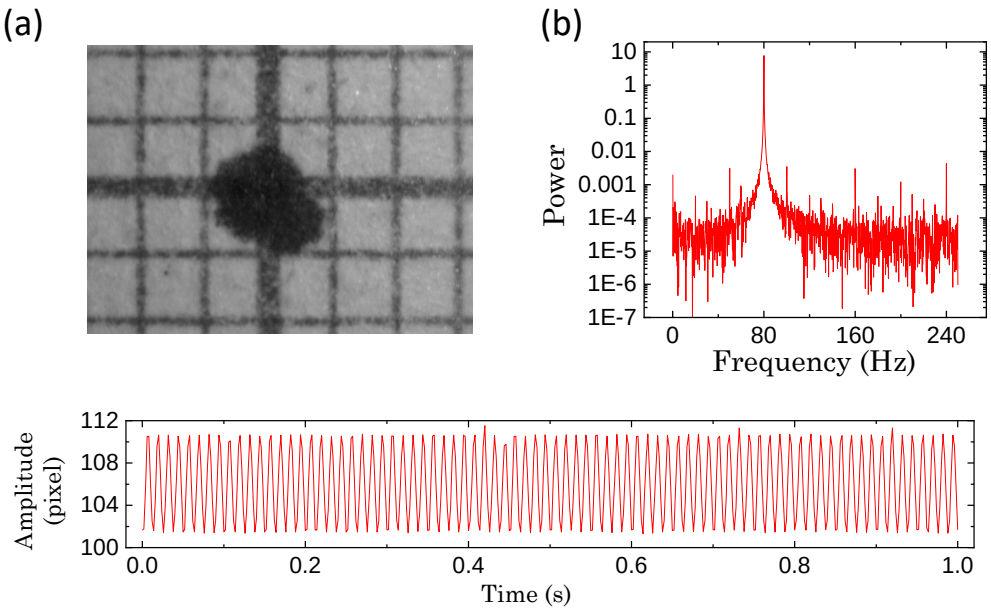

Figure 7.2: (a) An image of the marker attached to the vibrating cup of our setup that is used to calibrate the frequency and amplitude of the vibrations. Bottom panel shows a typical amplitude profile of the shaker. Data shown is for 80 Hz over an interval of 1s. (b) Fast Fourier Transform corresponding to the amplitude profile shown in (a) indicating the frequency of the vibrations.

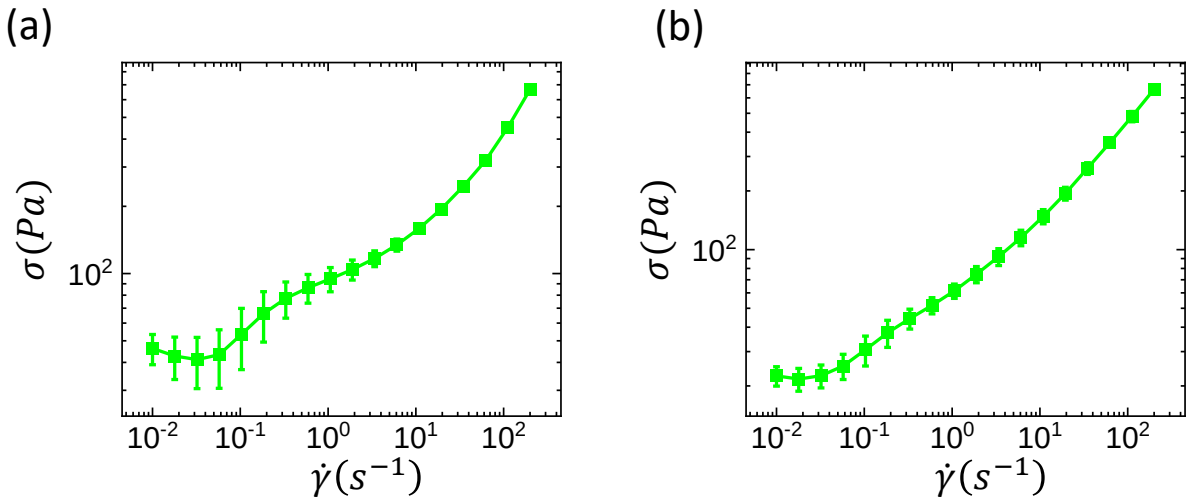

Figure 7.3: Flow curves of the density mismatched (Cornstarch particles dispersed in Paraffin oil) and density matched (Cornstarch particles dispersed in density matched Organic oil) systems without vibration in (a) and (b) respectively. The non-monotonic behavior at low shear rates is similar to that observed in attractive/adhesive systems before, as mentioned in the text. Error bars indicate averages taken over 3 increasing and 3 decreasing shear rate runs.

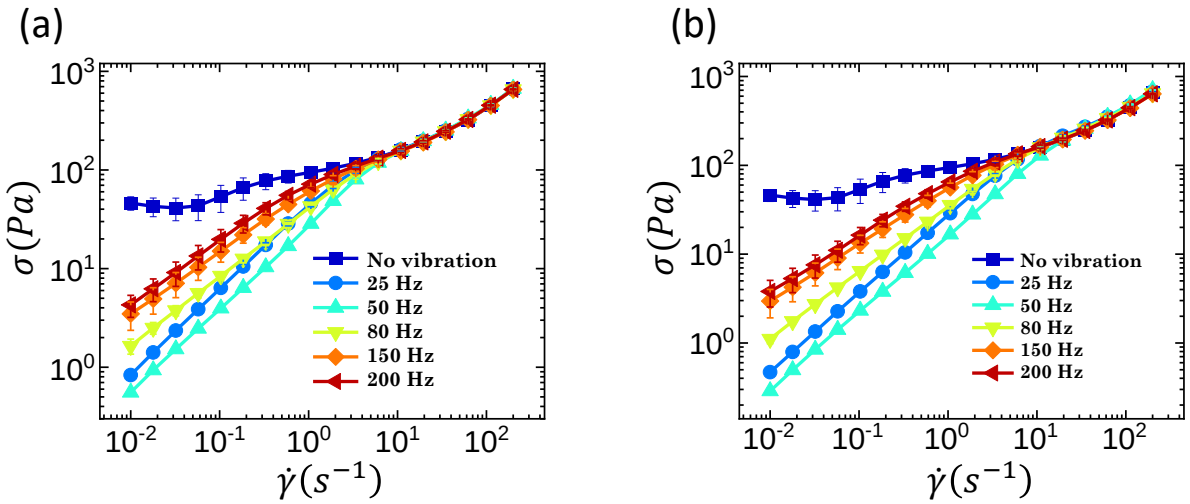

Figure 7.4: Flow curves for Cornstarch particles dispersed in Paraffin oil without and with vibration at different frequencies indicated by the legend in the figures. The input current value is 0.1A in (a) and 0.3A in (b). Error bars indicate averages taken over 2 increasing and 2 decreasing shear rate runs.

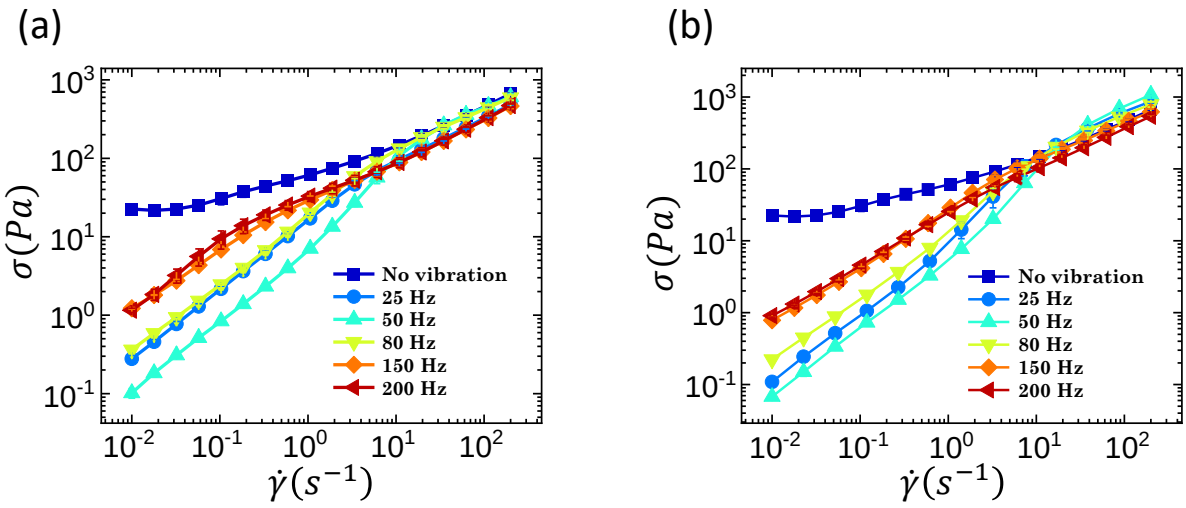

Figure 7.5: Flow curves for Cornstarch particles dispersed in density matched Organic oil without and with vibration at different frequencies as indicated by the legend in the figures. The input current value is 0.1A in (a) and 0.3A in (b). Error bars indicate averages taken over 2 increasing and 2 decreasing shear rate runs.

From Fig. 7.4 and 7.5, I observe that the sample no longer shows a yield stress and the stress value obtained from the lowest shear rate ($0.01s^{-1}$) is significantly reduced in both cases. The flow curve becomes quasi-Newtonian at the low shear rate regime for all frequencies. However, I observe that the lower frequencies $f = 25Hz$ and $f = 50Hz$ show a greater reduction of the adhesive yield stress in both systems. At large shear rates, I see the behavior of both the systems is predominantly shear dominated, as the flow curves under vibration overlap with that of the no-vibration case. This crossover from a vibration dominated to a shear dominated regime is similar to that observed in frictional yield stress systems [9, 11]. I do notice, however, that the overlap in the shear dominated region is near perfect for the CS-Paraffin oil system (particle and solvent density mismatched) but there is a spread in case of the CS-Organic oil system (particle and solvent density matched).

Now, in order to gain more insight about the non-monotonic reduction of stress with applied vibration frequency in Fig. 7.4 and 7.5, I calculate the vibration stress (σ_V) according to equation 7.1 for each of the frequencies. As mentioned earlier, I use the high speed imaging to obtain the corresponding values of amplitudes for each frequency. In Fig. 7.2, I show a typical image of the marker attached on to the vibrating cup that I track for image analysis. I also show a typical amplitude profile during vibration and the corresponding Fast Fourier transform that gives us the frequency of the vibration.

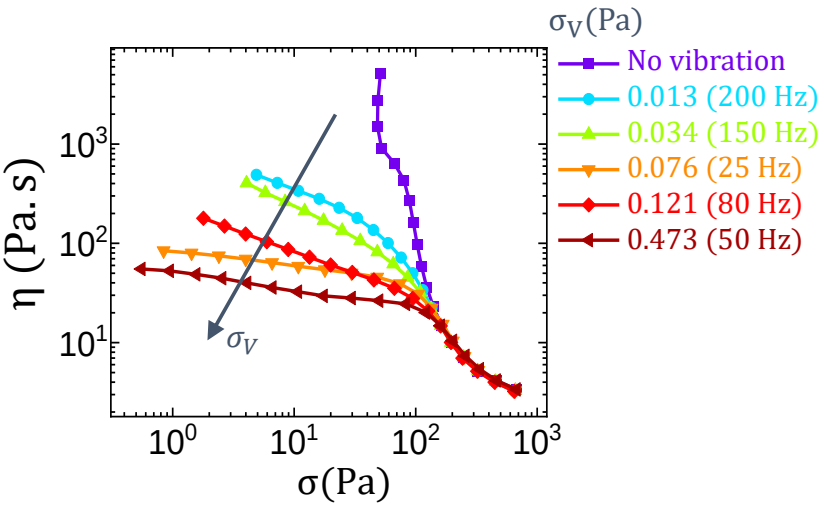

Figure 7.6: Viscosity (η) as a function of stress (σ) for the average data shown in Fig. 7.4(a). The flow curves are plotted at increasing values of vibration stress (σ_V) calibrated in terms of the frequency (indicated in brackets in the legend) and corresponding amplitude of the applied vibrations according to equation 7.1. The input current value is 0.1 A for each frequency.

In Fig. 7.6, I plot the viscosity as a function of shear stress (similar to [9]) for increasing values of σ_V for the CS-Paraffin oil system at input current value of 0.1A. I observe a monotonic drop in viscosity with increasing σ_V. This implies that our adhesive yield stress system also follows the same trend as has been observed for the frictional yield stress systems.

Finally, I explore the effects of vibration on a shear-thickening dense suspension formed by dispersing Polystyrene particles in PEG-400. For this case, I varied the frequency in the range of 1 Hz to 200 Hz and the input current was varied from 0.1A to 1A for each frequency. In Fig. 7.7(a), I plot the viscosity vs shear rate for increasing current values (proportionately increasing the amplitude of the vibration) at a constant frequency of 50 Hz. In Fig. 7.7(b), I plot the same for increasing values of frequency at a constant input current of 0.4A.

I find an increase in the viscosity of the suspensions for low shear rates (quasi- Newtonian regime) in both the cases. This effectively reduces the difference between the viscosity in the shear thickening regime and the quasi-Newtonian regime. Further experiments are ongoing to see the generality of these results.

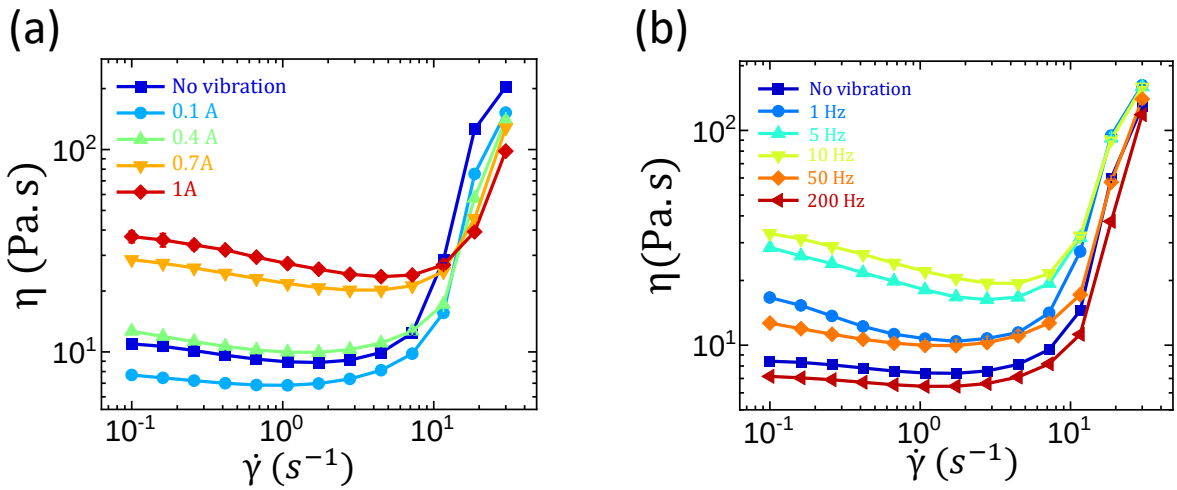

Figure 7.7: Viscosity (η) as a function of applied shear rate ($\dot{\gamma}$) for Polystyrene particles dispersed at PEG under different input conditions. In (a), at a constant frequency of 50 Hz, I increase the input current as indicated in the legend of the figure. In (b), for a constant input current of 0.4A, the frequency is systematically increased from low to high values. Errors bars are averaged over an increasing and a decreasing shear rate run.

7.4 Conclusion

In this chapter, I study the effects of superimposed orthogonal vibration on the rheology of jammed dense suspensions. For adhesive suspensions, I study two cases: i) Particles and the suspending fluid are density mismatched and ii) Particles and the suspending fluid are density matched. Previous works have reported a reduction of frictional yield stress (originating from the settling of particles) under applied vibration. To our knowledge, this is the first report of vibration induced reduction of adhesive yield stress. Similar to earlier studies, I observe that the effects of vibration are predominantly in the regime of low shear rate, while at high shear rates, the presence of vibration does not affect the flow behavior of the system. However, I do observe a slight variation in the density matched suspension where, at high shear rates, some deviation is observed between the cases with and without the applied orthogonal vibration. Further experiments are needed to confirm if density mismatch between the particles and the suspending fluid is a significant factor in tuning the suspension viscosity using orthogonal vibration.

I also study shear-thickened suspensions formed by dispersing Polystyrene particles in PEG. I see that the degree of relative shear thickening does get reduced under vibration. However, this effect is a result of an increase in the hydrodynamic viscosity of the suspension. Such an increase has not been reported previously. An important factor in our

case is that the particles (PS) are density matched with PEG whereas previous works in this regard have used density mismatched suspensions. At this point, I do not understand whether the neutral buoyancy of the particles is responsible for the observed effects but this is an interesting future direction.

Bibliography

[1] H. M. Jaeger and Sidney R. Nagel. Physics of the Granular State. *Science*, 255(5051):1523–1531, March 1992.

[2] James B. Knight, Christopher G. Fandrich, Chun Ning Lau, Heinrich M. Jaeger, and Sidney R. Nagel. Density relaxation in a vibrated granular material. *Phys. Rev. E*, 51(5):3957–3963, May 1995.

[3] J. A. Dijksman and M. van Hecke. The role of tap duration for the steady-state density of vibrated granular media. *Europhys. Lett.*, 88(4):44001, December 2009.

[4] Joshua A. Dijksman, Geert H. Wortel, Louwrens T. H. van Dellen, Olivier Dauchot, and Martin van Hecke. Jamming, Yielding, and Rheology of Weakly Vibrated Granular Media. *Phys. Rev. Lett.*, 107(10):108303, September 2011.

[5] M. Nicolas, P. Duru, and O. Pouliquen. Compaction of a granular material under cyclic shear. *Eur. Phys. J. E*, 3(4):309–314, December 2000.

[6] P. Porion, N. Sommier, and P. Evesque. Dynamics of mixing and segregation processes of grains. *Europhys. Lett.*, 50(3):319, May 2000.

[7] A. Gnoli, L. de Arcangelis, F. Giacco, E. Lippiello, M. Pica Ciamarra, A. Puglisi, and A. Sarracino. Controlled Viscosity in Dense Granular Materials. *Phys. Rev. Lett.*, 120(13):138001, March 2018.

[8] S. Kiesgen de Richter, C. Hanotin, P. Marchal, S. Leclerc, F. Demeurie, and N. Louvet. Vibration-induced compaction of granular suspensions. *Eur. Phys. J. E*, 38(7):1–9, July 2015.

[9] C. Hanotin, S. Kiesgen de Richter, P. Marchal, L. J. Michot, and C. Baravian. Vibration-induced liquefaction of granular suspensions. *Phys. Rev. Lett.*, 108(19):198301., May 2012.

[10] C. Hanotin, S. Kiesgen de Richter, L. J. Michot, and Ph. Marchal. Viscoelasticity of vibrated granular suspensions. *J. Rheol.*, 59(1):253–273, January 2015.

[11] Naïma Gaudel, Sébastien Kiesgen de Richter, Nicolas Louvet, Mathieu Jenny, and Salaheddine Skali-Lami. Bulk and local rheology in a dense and vibrated granular suspension. *Phys. Rev. E*, 96(6):062905, December 2017.

[12] Ashish Garg, Nico Bergemann, Beccy Smith, Matthias Heil, and Anne Juel. Fluidisation of yield stress fluids under vibration. *J. Non-Newtonian Fluid Mech.*, 294:104595, August 2021.

[13] Neil Y. C. Lin, Christopher Ness, Michael E. Cates, Jin Sun, and Itai Cohen. Tunable shear thickening in suspensions. *Proc. Natl. Acad. Sci. U.S.A.*, 113(39):10774–10778, September 2016.

[14] Christopher Ness, Romain Mari, and Michael E. Cates. Shaken and stirred: Random organization reduces viscosity and dissipation in granular suspensions. *Sci. Adv.*, 4(3), March 2018.

[15] Prateek Sehgal, Meera Ramaswamy, Itai Cohen, and Brian J. Kirby. Using Acoustic Perturbations to Dynamically Tune Shear Thickening in Colloidal Suspensions. *Phys. Rev. Lett.*, 123(12):128001, September 2019.

[16] Ran Niu, Meera Ramaswamy, Christopher Ness, Abhishek Shetty, and Itai Cohen. Tunable solidification of cornstarch under impact: How to make someone walking on cornstarch sink. *Sci. Adv.*, 6(19), May 2020.

[17] C. Garat, S. Kiesgen de Richter, P. Lidon, A. Colin, and G. Ovarlez. Using good vibrations: Melting and controlled shear jamming of dense granular suspensions. *J. Rheol.*, 66(2):237–256, March 2022.

[18] Pappu Acharya and Martin Trulsson. Optimum dissipation by cruising in dense suspensions. *arXiv*, February 2023.

[19] Ehsan Irani, Pinaki Chaudhuri, and Claus Heussinger. Impact of Attractive Interactions on the Rheology of Dense Athermal Particles. *Phys. Rev. Lett.*, 112(18):188303, May 2014.

[20] Ehsan Irani, Pinaki Chaudhuri, and Claus Heussinger. Athermal rheology of weakly attractive soft particles. *Phys. Rev. E*, 94(5):052608, Nov 2016.

CHAPTER

EIGHT

Summary and outlook

This chapter summarizes the main results of the thesis and addresses possible future research directions.

In this thesis, I study rheological properties of different athermal dense particulate suspensions. Depending on the inter-particle interactions, the systems studied can be broadly categorized into two classes: (i) Static jammed systems with particles having adhesive inter-particle interactions, and (ii) Systems showing shear-induced jamming.

The static jammed systems that I study, are formed from dense suspensions of granular particles having adhesive inter-particle interactions. I find that this system is highly non-linear even far below the flow point (where the behavior of the system undergoes a crossover from a predominantly elastic to viscous nature). I develop a framework to study the yielding dynamics of these systems in terms of the normalized energy dissipation. I use boundary imaging to map out the microscopic particle level rearrangements, flow behavior and plasticity. This allows us to correlate local particle dynamics to the bulk energy dissipation in the system. Further, I use particle settling experiments to independently determine critical jamming volume fractions of the system. Using these, I explain the flow behavior of the system over a wide parameter space of applied strain and particle volume fraction. Finally, I use surfactants to tune the inter-particle adhesion to explain the observed dissipation and non-linear effects in the system. In future, it will be interesting to explore this energy dissipation based framework of yielding in other soft materials. Further, I also use superimposed orthogonal vibration as an external handle to tune the adhesive yield stress in this system. Although I have shown that both density matched and density mismatched adhesive suspensions show similar yielding and non-linear behavior, further investigation of whether density matching affects particle level dynamics is an interesting future direction.

The data analysis scheme that I develop in this thesis to characterize the non-linear rheological behaviour of the static jammed systems is based on bulk behavior of the system. This framework does not take into account the strain localization and particle-level plasticity observed in our system. From our imaging data, it is fair to assume that the different shear banded regions will follow different constitutive equations. The interaction between such regions remains unknown in our case. Although at this point, I do not understand the origin of shear banding in our system, invoking non-local rheology for this system could be a worthwhile effort. Large Amplitude Oscillatory Shear measurements classify the system's behavior into three different regimes: a quasi linear regime at very low strain values, followed by an intermediate deformation regime where the system shows strain-stiffening and plasticity; finally a fully plastic regime at large strains. Elasto-visco-

plastic models with a non-linear elastic element are likely to be a good description for some of the observed behaviour. However, establishing a suitable model that captures such a rich phase behavior, particularly for the intermediate strain regime, remains an interesting future direction to explore..

Next, I explore the out of equilibrium nature of disordered jammed solids by studying memory formation in the static jammed system mentioned above. I report strong signatures of the encoded memory in the mechanical properties of the bulk system. By tuning the inter-particle interaction, I establish the importance of inter-particle adhesion in the formation of such strong mechanical memory. Using optical boundary imaging and subsequent velocity profile analysis, I propose a strand based mechanism behind the observed memory signature. Further, I explore encoding of multiple memories in this system. Interestingly, I observe a systematic shift in the position of the existing memory by training the system at a different amplitude. This results in a phantom memory that was not encoded in the system. Further, such memory shifting has a systematic dependence on the shear rate associated with the training. Importantly, I are limited by the optical opacity of our suspensions which has made it challenging to image the bulk of the system. In this thesis, I primarily use boundary optical imaging to study the particle level dynamics of the system. It will be interesting, in future, to explore better techniques (both optical and non-optical) to probe the bulk structure of the system. This can help in establishing the underlying physical mechanisms more robustly.

Finally, I study shear-jammed dense particulate suspensions. For this work, I synthesize polystyrene microspheres using the dispersion polymerization technique and use them to make shear-thickening dense suspensions. I combine steady state measurements with established phenomenological models to distinguish between the Discontinuously Shear-Thickened state and the Shear-Jammed state of the suspensions. In future, it is important to establish the validity/applicability of this approach to a broader, more general class of suspensions with non-spherical particle shapes, poly-disperse size distributions, etc. Additionally, the effects of orthogonal vibration on the shear-thickened as well as shear jammed state of the suspensions requires further investigation. Our preliminary results point towards an interesting role played by particle-fluid density matching, which remains a promising future direction to explore.

Both inter-particle interactions as well as frictional interactions have a crucial role in the observed macroscopic phenomena in this thesis. However, to correlate the observed critical strain/stress values with such microscopic interactions, characterization techniques like AFM are required, which will require future efforts and presently remain outside the

scope of this thesis. Normal force data remained consistent with the existing knowledge of shear-thickening granular systems, showing an increasing trend with increasing applied stress in the shear thickening regime. However, for the strain stiffening systems where in some cases we observe a negative normal stress, the trend remains inconclusive due to small magnitude and noisy nature of the normal force data. Future work with more precise measurement techniques should be able to decipher if any conclusive normal force trend exists.